INFLUENCE OF FINE-SCALE NIOBIUM CARBONITRIDE PRECIPITATES ON HYDROGEN-INDUCED CRACKING OF X70 PIPELINE STEEL

BY: CAROLINE THERESA WOJNAS, B.Sc.

A thesis submitted to the Department of Materials Science and Engineering in partial fulfilment of the requirements for the degree of Master of Applied Science in Materials Engineering

Title:	Influence of Fine-scale Niobium Carbonitride Precipitates on Hydrogen-Induced Cracking of X70 Pipeline Steel
Author:	Caroline Theresa Wojnas, B.Sc. (McMaster University)
Supervisors:	Dr. Joey R. Kish and Dr. Joseph R. McDermid
Pages:	xii – 136

ABSTRACT

The microstructure of steel is well known to affect hydrogen-induced cracking (HIC) susceptibility by having certain heterogeneities serving as effective hydrogen trap sites. A consensus on whether or not fine-scale niobium carbide (NbC), nitride (NbN) and carbonitride (Nb(C,N)) precipitates can behave as effective hydrogen traps has yet to be established. The H-trapping capacity of Nb precipitates in a Fe-C-Mn-Nb model steel was investigated with the goal of minimizing embrittlement effects and improving the design of X70 pipeline grade steel for sour service oil and gas applications. First, a heat treatment was applied to the model steel to change the Nb-based precipitate size distribution, which was subsequently characterized via transmission electron microscopy, electron energy loss spectroscopy, and atom probe tomography. The experimental heat treatment increased the number of fine-scale precipitates (<15 nm) that are ideal for APT characterization. NbN and NbC precipitates of various stoichiometries were confirmed within the steel. Further, a custom electrolytic H-charging device was designed, fabricated, and validated using thermal desorption spectroscopy. Additionally, the extent of galvanic corrosion between NbC and NbN and the steel matrix was determined using custom scaled-up particle matrix specimens. Potentiodynamic polarizations conducted using active and passivating electrolytes revealed the relative nobility of the materials. Both NbC and NbN particles were more noble than the steel matrix; thus, possessing driving force for galvanic corrosion, with the particles serving as cathodes. Future studies involving electrolytic charging of the steel in a D-based electrolyte coupled with atom probe tomography will facilitate the direct observation of H-trapping sites relative to various Nb-based precipitates and contribute to an improved understanding of the mechanisms governing HIC.

Keywords: Corrosion resistance, Hydrogen-induced cracking (HIC), High strength low alloy (HSLA), X70 grade pipeline steel, Nb content

ACKNOWLEDGEMENTS

First, thank you to my supervisors Dr. Joe McDermid and Dr. Joey Kish for their support and encouragement throughout my graduate studies. I've developed many skills and expanded my knowledge in a variety of areas while working as a researcher at the Centre for Automotive Materials & Corrosion. Thank you to Dr. Beth McNally for many engaging training sessions, lectures, helpful advice, and in-lab support. Your enthusiasm towards your work continues to inspire and motivate many. From the CAMC, I'd also like to thank Dr. Ghazal Seyed-Mousavi and Dr. Hatem Zurob for their support with the heat treatments, as well as Sara Filice for assisting with TEM sample preparation and for electrochemistry training sessions. I appreciate the funding from Natural Sciences and Engineering Research Council of Canada, EVRAZ North America, and Companhia Brasileira de Metalurgia e Mineração.

From the Canadian Centre for Electron Microscopy, I would like to thank Dr. Brian Langelier for many informative atom probe tomography training sessions, as well as Mr. Jhoynner Martinez, Dr. Xiang Wang, and Dr. Carmen Andrei for electron microscopy support. Also, thank you to Mr. Jim Cleaver and Dr. Moisei Bruhis for their assistance with the hydrogen charging device assembly, and Dr. Nicholas Senior for thermal desorption spectroscopy support. Great to see the device working, and excited to see what's to come on this project. Lastly, thanks to Dr. Mark Biesinger at Surface Science Western for XPS support. Looking forward to what's next.

Contents

LIST OF EQUATIONS

LIST OF FIGURES

LIST OF TABLES

LIST OF ABBREVIATIONS

ACC	**A**ccelerated **C**ooling
APT	**A**tom **P**robe **T**omography
BN	**B**aking-**N**utting
BCC	**B**ody-**C**entered **C**ubic
CI	**C**onfidence **I**nterval
CLR	**C**rack **L**ength **R**atio
COW	**C**ombined **W**elding
CSL	**C**oincidence **S**ite **L**attice
CSR	**C**rack **S**ensitivity **R**atio
CTR	**C**rack **T**hickness **R**atio
DQ	**D**irect **Q**uenching
EDS	**E**nergy-**D**ispersive X-ray **S**pectroscopy
EELS	**E**lectron **E**nergy **L**oss **S**pectroscopy
EW	**E**lectric **W**elded
FCC	**F**ace-**C**entered **C**ubic
FFT	**F**ast **F**ourier **T**ransform
FIB	**F**ocused **I**on **B**eam
FP	**F**errite-**P**earlite
HAGB	**H**igh **A**ngle **G**rain **B**oundaries
HE	**H**ydrogen **E**mbrittlement
HIC	**H**ydrogen-**I**nduced **C**racking
HP	**H**ydrogen **P**ermeation
HSLA	**H**igh **S**trength **L**ow **A**lloy
LAGB	**L**ow **A**ngle **G**rain **B**oundaries

LB	**L**ower **B**ainite
LW	**L**aser **W**elded
MA	**M**artensite-**A**ustenite
PSL	**P**roduct **S**tandard **L**evel
QT	**Q**uenched and **T**empered
RD	**R**olling **D**irection
SANS	**S**mall-**A**ngle **N**eutron **S**cattering
SATP	**S**tandard **A**mbient **T**emperature and **P**ressure
SAW	**S**ubmerged **A**rc **W**elding
SCC	**S**tress **C**orrosion **C**racking
SEM	**S**canning **E**lectron **M**icroscopy
SIMS	**S**econdary **I**on **M**ass **S**pectroscopy
SKPFM	**S**canning **K**elvin **P**robe **F**orce **M**icroscopy
SSRT	**S**low **S**train **R**ate **T**esting
STEM	**S**canning **T**ransmission **E**lectron **M**icroscopy
TD	**T**ransverse **D**irection
TDS	**T**hermal **D**esorption **S**pectroscopy
TEM	**T**ransmission **E**lectron **M**icroscopy
TMCP	**T**hermo**m**echanical **C**ontrolled **P**rocessing
UB	**U**pper **B**ainite
XPS	**X**-ray **P**hotoelectron **S**pectroscopy

1. INTRODUCTION

1.1. MOTIVATION

The global energy industry demands pipeline steel with appropriate mechanical properties for sustainable construction. American Petroleum Institute (API) 5L X70 is a high strength low alloy (HSLA) steel. It is the first generation of thermomechanically processed pipeline steel designed to meet the need for steels with higher strength and toughness, compared to conventional hot-rolled and normalized grades. The advent of combining thermomechanical controlled processing (TMCP) with accelerated cooling (ACC) has honed these characteristics. However, a tradeoff typically exists between strength and corrosion susceptibility of steels [1].

Numerous steel structures undergo catastrophic failure due to hydrogen evolution from their service environments caused by corrosion reactions and cathodic protection (CP). Hydrogen is near-ubiquitous [2] and its accumulation can lead to abrupt and typically unpredictable decrease in toughness, ductility, and material resistance to fatigue-crack propagation via hydrogen embrittlement [3]. The hydrogen commonly originates from moisture and molecular water reduction because of CP [4]. A real-life example is the Gulf of Mexico oil spill in 2010, which was triggered by catastrophic failure of connector bolts due to hydrogen embrittlement [3].

Most of the oil and natural gas today is sour, meaning these products contain hydrogen sulfide (H2S) gas. Cracking risk of a pipeline carrying H2S-rich products is especially high as H2S can poison hydrogen recombination at the pipe inner surface. This creates more hydrogen atoms, which diffuses into the material and leads to a corrosion phenomenon known as hydrogen-induced cracking (HIC) [4]. HIC is a brittle material fracture mode experienced by pipeline steel at stresses below the yield (permanent deformation) stress [5]. In this process, hydrogen atoms at the steel-electrolyte interface diffuse into the steel, recombine into H_2 gas at different microstructural heterogeneities, and build-up internal pressure.

Metallurgical heterogeneities where hydrogen recombination is favorable are referred to as hydrogen trap sites, and span many length scales, from matrix phases to nanoscale strengthening intermetallic particles. When the hydrogen accumulates to reach a critical amount, cracks can initiate without external stresses, potentially leading to abrupt material failure [6]. Additionally, the steel pipelines transporting these products operate in harsh environments, further necessitating pipe material to possess adequate corrosion resistance.

Many strategies have been proposed to enhance the HIC-resistance of X70 steel [7]. These include controlling the inclusion size and amount [8], decreasing the chemical composition segregation [9], grain-boundary engineering [10], introducing hydrogen traps to better distribute hydrogen [11, 12], adding microalloying elements [13], and texture engineering [14].

One of the more promising methods for HIC-mitigation of pipeline steels is the dispersion of fine carbonitride precipitates of Nb, V and Ti [15]. Together, these fine particles increase yield and tensile strength via precipitation strengthening [16]. Additionally, it has been proposed these precipitates can serve as effective hydrogen-trapping sites, driving hydrogen away from relatively HIC-susceptible regions such as elongated MnS inclusions and/or grain boundaries [17]. Whether or not this is beneficial in terms of HIC-effects on steels remains a topic of immense debate. Figure 1-1 schematically shows a variety of potential traps in steel, highlighting the carbonitride trap type in red [18].

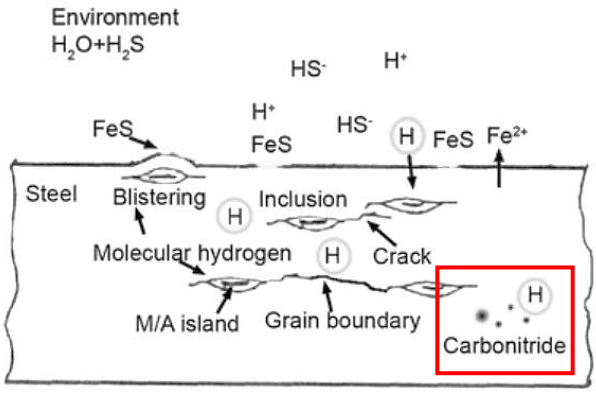

Figure 1-1: H-trap sites in pipeline steel operating in a sour-service environment [18].

1.2. RESEARCH OBJECTIVES

To thoroughly investigate this HIC-mitigation strategy, more research must be carried out on Nb, V and Ti precipitates, specifically to study their associated activation energies, hydrogen-trapping location(s), and how the size, size distribution, stoichiometry, and volume fraction of such particles impacts HIC. In this research work, focus was placed on determining the HIC-effects associated with Nb-based precipitates. The hydrogen-

trapping capacity of V and Ti carbides and their beneficial effects on HIC behavior have been widely reported [19-24].

First, an as-received Nb model steel was heat-treated to alter the size distribution of NbC, NbN, and Nb(C,N) precipitates. The material was characterized using an array of techniques to determine the size distribution, morphologies, and chemistries of Nb precipitates as a function of heat treatment. The Nb model steel sample preparation procedure was optimized for atom probe tomography (APT) after comparing APT ion yields from specimens prepared by electropolishing and electropolishing combined with plasma focused ion beam (PFIB) milling. APT was then employed to visualize the NbC precipitates at the nanoscale and determine their stoichiometry. An electrolytic charging device was designed, fabricated, and tested using thermal desorption spectroscopy to validate its ability to charge the steel with hydrogen. This was conducted in preparation for determining the hydrogen-trapping location(s) relative to NbC precipitates via APT coupled with electrolytic deuterium-charging.

A separate project determined the galvanic corrosion tendency of NbC or NbN inclusions coupled to pure iron. This was completed to test if NbC and/or NbN are effective cathode materials for generating hydrogen, which can diffuse into the steel matrix and contribute to HIC. Custom model iron-inclusion couples were studied in passive and active electrolytes using a series of electrochemical measurements, specifically potentiodynamic polarizations. The model inclusion results were then compared to potentiodynamic polarization results obtained from a commercial X70 steel. Both research works were carried

out with the overall goal of mitigating corrosion, specifically, HIC, to improve the alloy design of X70 pipeline grade steel for sour service oil and gas applications.

1.3. VALUE OF RESULTS

The National Energy Board (NEB) governs close to 45,000 km of pipeline in Canada. In 2006, crude oil, petroleum products, natural gas liquids and natural gas collectively valued at $110 billion were transported by these pipelines. The cost of corrosion, including material failure, operations, and maintenance, in the transmission pipeline industry is estimated to be 0.08% of the gross domestic product in developed nations. This value was 1.53 trillion USD for Canada in 2016 [25]. Furthermore, of 15,609 leaks and 880 rupture cases of provincially regulated pipelines in Alberta from 1990-2012, 509 were reported to be due to HIC, stress-corrosion cracking (SCC), fatigue, and mechanical damage [26]. Clearly, implementation of reliable pipeline infrastructure is crucial to avoid detrimental effects on the global economy, environment, and human health. A thorough understanding of the interaction of hydrogen and steel microstructure, specifically with Nb precipitates, will aid in enhancing the mechanical properties of the current generation of TMP pipeline steels (including X70) operating in hydrogen-rich settings.

1.4. THESIS OUTLINE

This thesis has been divided into six chapters. Chapter 1 provides an introduction. Chapter 2 reviews the following areas: X70 steel composition, processing, structure and its HIC-susceptibility, microstructural hydrogen-mapping in steels, effects of carbonitride precipitates on HIC, and electrochemical activity of NbC and NbN phases. Following the literature review, Chapter 3 describes the materials and methodology employed for each of the two research projects introduced in section 1.2. Chapter 4 presents the results and discussion associated with each project. Finally, Chapter 5 summarizes the key conclusions draw from the research.

2. LITERATURE REVIEW

2.1. X70: CHEMISTRY, STRUCTURE AND PROCESSING

HSLA steels are grades developed for high pressure purposes, notably in the development of pipelines for transporting oil and natural gas. These steels are characterized by a low carbon weight percentage, relatively high manganese weight percentage, and small additions of alloying elements including niobium, titanium, vanadium, and molybdenum. This controlled process of adding small quantities (in mass parts per million) of various alloying elements is referred to as microalloying [27-31].

X70 grade was developed with higher strength for pipeline applications [32]. Material properties are governed by the steel chemistry and microstructural features [30, 33, 34], hence the importance of microalloying is highlighted in addition to the role of each elemental constituent in X70. Further, the significance of the development and use of thermomechanical controlled processing (TMCP) coupled with accelerated cooling (ACC) is emphasized. With these techniques, specific microstructures associated with desired mechanical properties can be fabricated [35], allowing for the creation of steels with higher strength than conventional hot rolled and normalized Fe-C-V steels.

2.1.1. STEEL CHEMISTRY

The main function of alloying with metallic elements is to strengthen ferrite by three unique mechanisms: solid solution strengthening, precipitation hardening and grain refinement [32]. Solid solution strengthening is associated with chemical composition,

whereas the two latter mechanisms rely on the collaboration of elemental constituents and the TMCP process [30, 36]. The alloying elements used are typically deemed to demonstrate low hardenability effects [37]. Solid solution strengthening involves alloying a metal in the single-phase region of a phase diagram. Local strain of certain alloying elements hinders dislocation movement, providing strength. Even stronger HSLA steels can be developed by introducing a second phase. This practice is referred to as dispersoid strengthening and can be facilitated by precipitation. Metal carbide and nitrides precipitate over three distinct stages throughout the processing of microalloyed steels [38, 39]. As a result, metal carbide and nitride precipitates can be classified as types I-III.

Type I precipitates arise in the liquid phase during or after solidification. They are found on the liquid/solid interface and in the delta ferrite phase. Type I precipitates do not influence austenite recrystallization [37]. Type II particles form in austenite after solution treatment and controlled rolling with cooling [40]. Precipitates of this type are strain-induced. In other words, they result from heterogenous precipitation on dislocations and grain boundaries [37]. They can effectively retard austenite recrystallization. Particles of type III are generated throughout or after the austenite-ferrite transformation. They nucleate both on the austenite/ferrite interface and in ferrite [41]. Type III precipitate formation facilitates dispersion strengthening in ferrite.

Alloying elements can refine the grain microstructure by controlling the transformation temperatures. For example, reducing T Ar3, the temperature which marks the start of austenite's phase transformation to ferrite and/or pearlite when cooling, causes

finer grains to form [30, 36]. Reduction of T Ar3 is key source of strength and toughness. Type II precipitates contribute greatly to the grain refinement in martensite-austenite (MA) steels by retarding of austenite recrystallization [42-44].

2.1.1.1. *Carbon*

X70 steel has relatively low carbon content. For this grade of steel, the mass fraction of carbon, based on heat and product analyses, is a maximum of 0.28 wt.% and 0.26 wt.% in seamless pipe and welded pipe, respectively [45]. Carbon aids in matrix strengthening by precipitation [32, 37], and serves as a potent solid solution strengthener. As an interstitial element, carbon distorts the body-centered cubic (BCC) lattice of iron, resulting in a local strain field that inhibits dislocation movement. In addition, reducing carbon content improves weldability, cold forming properties, and decreases heat affected zone (HAZ) hardness [46, 47]. The HAZ microstructure and properties modify due to the weld heat.

2.1.1.2. *Manganese*

X70 features relatively high manganese weight percentage. The mass fraction of manganese based on heat and product analyses is a maximum of 1.40 wt.% in seamless pipe and 1.65 wt.% in welded pipe. Additionally, for each reduction of 0.01 % below the specific maximum concentration for carbon, an increase of 0.05 % above the specified maximum manganese concentration is permitted, up to a maximum of 2.00 % for X70. In HSLA steels, manganese largely influences the microstructural design and properties. Specifically, this alloying element delays austenite decomposition during accelerated cooling, and decreases the ductile to brittle transition temperature [37]. Brittle phase formation by the means of

intercrystallite segregation throughout the solidification process can be avoided [48]. This results in the attainment of a fine-grained lower bainite microstructure, which is discussed further in a later section. Moreover, manganese exhibits a substitutional strengthening effect [32].

2.1.1.3. *Niobium*

Microalloying with niobium has been a large research focus in the development of microalloyed steels over the past 50 years [37]. X70 contains less than 0.15 wt.% niobium. To clarify, unless otherwise agreed upon, the total sum of the mass fractions of niobium, vanadium and titanium is less than or equal to 0.15 wt.% based on heat and product analyses in both seamless and welded pipe [45]. Morrison [49] contributed greatly to elucidating niobium carbide's role in strengthening microalloyed steels [50]. This is done through dispersoid strengthening, hindrance of austenite recrystallization, and grain refining of ferrite due to austenite grain-boundary pinning [51].

Although dependent on rolling conditions, precipitation of niobium carbide is typically incomplete regarding the thermodynamic equilibrium state. Consequently, a small fraction of the niobium stays in solid solution in the austenite phase once rolling is complete [46]. Between rolling passes, strain-induced precipitates reduce the temperature range in which recrystallization may occur [47]. This provides more nuclei for the austenite-ferrite transformation [46]. The recrystallization process is hindered through a solute drag mechanism which prevents austenite grain growth. This results in finer grain size; thus, providing toughness and strength [32]. The influence of niobium addition on mechanical

properties is demonstrated in Figure 2-1. The steel under study has 0.03 wt.% carbon. Even with different processing techniques, yield, and tensile strength for (0.09 wt.% niobium) are consistent to the API 5L X70 standard without reducing the toughness [47].

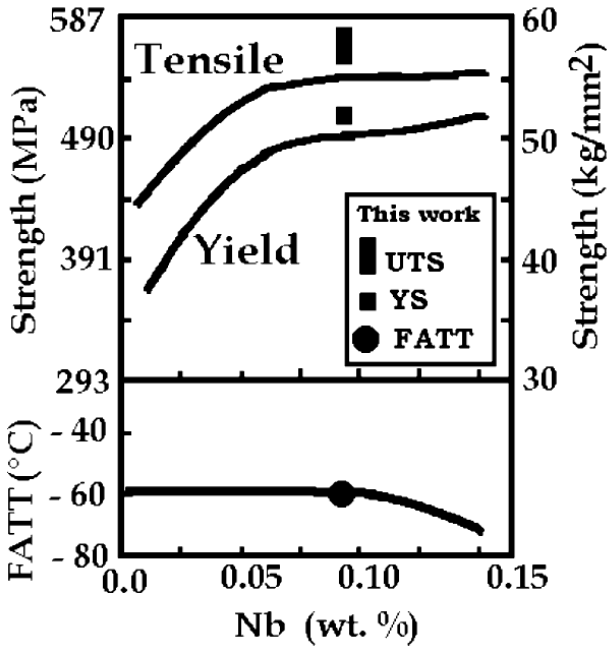

Figure 2-1 Mechanical properties versus niobium content. FATT represents the fracture appearance transition temperature [47].

Decreasing the rolling temperature leads to an austenitic matrix supersaturated with niobium. Niobium carbide particles can nucleate homogeneously in the matrix, but this is more commonly accomplished heterogeneously. Heterogenous nucleation sites include dislocations, grain boundaries, and on other metal nitride precipitates. Deformation strongly influences precipitation kinetics. When deformation occurs in the lower austenite region, niobium in solid solution delays the start of diffusion-controlled recrystallization. Precipitation occurs on dislocations produced by means of material deformation [46].

In the austenitic phase, niobium carbides and nitrides have face-centered cubic (FCC) structure. Niobium carbonitrides may appear in complex form and are incoherent [46]. This means these precipitates have an arbitrary orientation relationship with the surrounding ferrite matrix. During or after the austenite to ferrite transformation, nucleated carbonitride particles exhibit the Baker-Nutting (BN) orientation relationship to its ferritic matrix [52]. This means the [100] or [011] direction of the carbonitride precipitate is parallel to the [100] direction of ferrite, a relationship that was revealed using electron diffraction techniques [52, 53]. The probability of niobium carbide precipitation in ferrite or austenite-ferrite throughout the phase transformation process is associated with the finish rolling and cooling parameters [46]. Studies have demonstrated a high likelihood of precipitation in the ferrite at high cooling rates (such as 50°C/s), whereas the generation of interphase particles is expected with air cooling [54-56].

Niobium carbides and nitrides are excellent ferrite strengtheners [37]. The hardening effect from niobium in solid solution can be quantified using the Ashby-Orowan model [57], provided in Equation 2-1 [58]. Incoherent precipitates, such as niobium carbides and nitrides, cannot be sliced by dislocations. Instead, they are involved in the Orowan mechanism, imaged in Figure 2-2 [59]. The dislocations must bow through particle spacings until the two poles of the dislocations join. This requires more force compared to regular dislocation movement, leaving behind dislocation loops around the particles. The loops have associated strain fields, so the next dislocation to move through will require more force to do so. The extent of the associated strength increase is governed by volume, mass, and distribution of the particles, hence necessitating the exact characterization of the

precipitates present. The density of precipitates determines the interparticle spacing within the slip plane and is controlled in part by nucleation frequency.

$$\Delta\tau \approx \frac{0.81\mu b}{(1-\nu)^{1/2}\left(L_p - 2r_p\right)} \ln\left[\frac{2r_p}{b}\right] \tag{2-1}$$

where $\Delta\tau$ = *shear stress increment*

μ = *material shear modulus*

b = *Burger's vector*

r_p = *particle size*

ν = *material Poisson ratio*

L_p = *particle spacing*

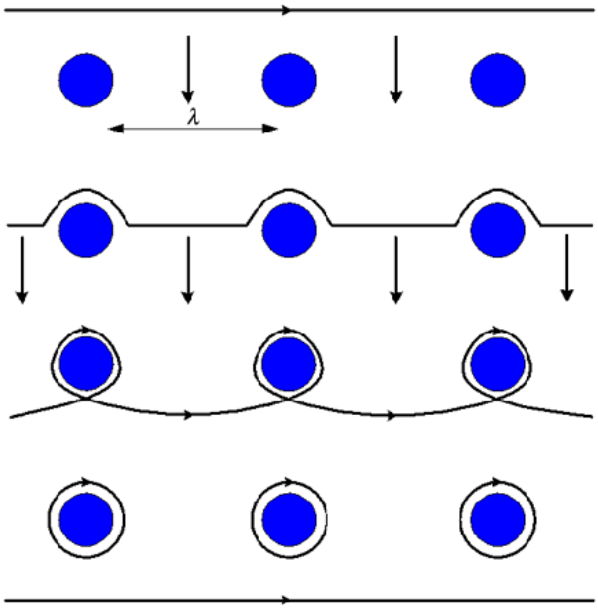

Figure 2-2: Orowan mechanism of precipitation strengthening [59].

2.1.1.4. Vanadium

The greatest use of vanadium today is in the manufacture of HSLA steels such as X70. Innovation of vanadium-microalloyed steels began in the 1950s [60]. Like niobium, this element is a strong ferrite strengthener due to the formation of vanadium carbides and nitrides [37]. Coherent strain fields from metal carbides and nitrides have seldom been reported in studies of precipitation in microalloyed steels. However, vanadium carbides and nitrides are a notable exception [38]. This is in part due to the very small size at which they lose coherence [37]. Vanadium carbonitrides have a fibrous morphology [61].

Vanadium is much more soluble in the austenitic phase relative to other microalloying elements. As a result, it stays in solution throughout more of the austenite range processing, contributing greatly to dispersoid strengthening in ferrite. The vanadium carbonitrides generated strengthen the microalloyed steel through engaging in the Orowan mechanism previously described. Larger stability or lower free energy is associated with vanadium nitrides when compared to vanadium carbides. This results in a greater driving force and denser precipitation in steels containing a higher mass fraction of nitrogen [60]. The thermomechanical processing needed to accommodate these differences and optimize API 5L X70 is explained later.

2.1.1.5. Titanium

The carbides and nitrides of titanium exhibit FCC structure; however, their carbonitrides are observed in complex form [46]. In the austenite phase, its carbonitrides are incoherent, and titanium nitride particles control the grain size. Grain refinement takes

place through suppression of the austenite grain coarsening. Past research has demonstrated nucleation of titanium carbides in austenite or ferrite occurs on grain boundaries, dislocations, or other precipitates [62, 63]. Therefore, titanium also aids in ferrite strengthening [32]. The low carbon content of HSLA steels, in combination with nitrogen binding to titanium, limits niobium carbonitride nucleation, assuring a sufficient level of niobium dissolves prior to rolling [64, 65]. As mentioned previously, niobium is proficient in precipitation strengthening. Furthermore, titanium fixes free nickel atoms, avoiding adverse effects of nickel on the steel's hardenability [32].

2.1.1.6. *Nickel, Molybdenum, Chromium and Copper*

Nickel is known to enhance low-carbon steel properties, while preserving useful weldability and low temperature toughness. This alloying element frequently improves fracture toughness. When compared to Mg and Mo, Ni tends to form less hardened microstructural features detrimental to low temperature toughness [32]. A weight percentage of 0.50 wt.% or less is typically used to develop 5L API X70 steels [45]. Addition of molybdenum to microalloyed steels boosts hardenability, promoting the development of advantageous lower bainite microstructure, which is discussed in the subsequent section. In addition to aiding in the formation of bainite, molybdenum is a ferrite strengthener [37]. A mass fraction of less than or equal to 0.15 wt.% is used in the manufacture of both seamless and welded X70 pipeline steel [45]. Both chromium and copper are added to improve corrosion resistance. Copper also serves as a ferrite strengthener [37]. A weight

percentage of less than or equal to 0.50 wt.% is used for each of these alloying elements in X70 steel [45].

2.1.1.7. *Sulfur, Phosphorus, Nitrogen and Boron*

Sulfur content must be less than or equal to 0.030 wt.%. The same mass fraction limit is used with respect to phosphorus addition [45]. Lowering sulfur levels boost hydrogen induced cracking (HIC) resistance [37]. Sulfide shape control with calcium is recommended to enhance notch toughness [66]. This treatment reduces the likelihood of atomic hydrogen reacting to produce molecular hydrogen, which can produce high pressure within the material's micropores [48]. However, controlled additions of sulfur have demonstrated ability to improve the machinability of the steel [37]. Low phosphorous contents minimize the hardening tendency of segregated areas in microalloyed steel [47]. Nitrogen plays a large role in the strengthening of steels through the formation of nitrides and carbonitrides [37]. Due to the difference in vanadium carbide and vanadium nitride solubilities, the presence of nitrogen influences the density of vanadium carbonitride precipitation. Hence, nitrogen content affects the extent of precipitation strengthening [60]. Although no deliberate addition of boron is permitted, the weight percentage of residual boron in X70 is typically less than or equal to 0.001 wt.% [37]. The remaining mass fraction is iron.

2.1.2. MICROSTRUCTURAL DESIGN

In the 1980s, both the pipeline and the automotive industries required strengths exceeding 420 MPa, the maximum yield strength ferrite-pearlite (FP) steels could achieve at the time. This necessitated the incorporation of higher strength microstructures. Researchers were interested in investigating lower temperature transformation products such as matrices containing non-polygonal ferrite, acicular ferrite, bainite and martensite. Bainite became one of the key structural components in pipeline steels of grade X70. Although incorporation of the martensitic phase results in even stronger material, stress-corrosion cracking susceptibility is heightened; thus, deeming this phase less suitable for pipeline steels [67]. The finer grains of bainite improve strength and toughness, and high dislocation mobility leads to further increase in steel strength [67].

The bainitic microstructure structure is further categorized as either upper or lower bainite. Figure 2-3 schematically differentiates lower bainite (LB) formation from that of upper bainite (UB). The major difference in upper and lower bainite morphologies is there is no cementite precipitation in the ferrite of UB. LB is characterized by fine cementite and carbide formation inside ferrite plates and is consequently superior in strength and toughness compared to UB. Bainite is a microstructure resulting from diffusive, incomplete transformation. As plates of bainite grow, excess carbon is partitioned into the residual austenite. The next plate grows from carbon-enriched austenite, and the process carries on until the transformation is impossible. The bainite start temperature is dropped through the addition of a vast array of alloying elements; however, carbon has the greatest influence

on bainitic microstructural development. Reducing the carbon content helps form the lower bainite structure [29].

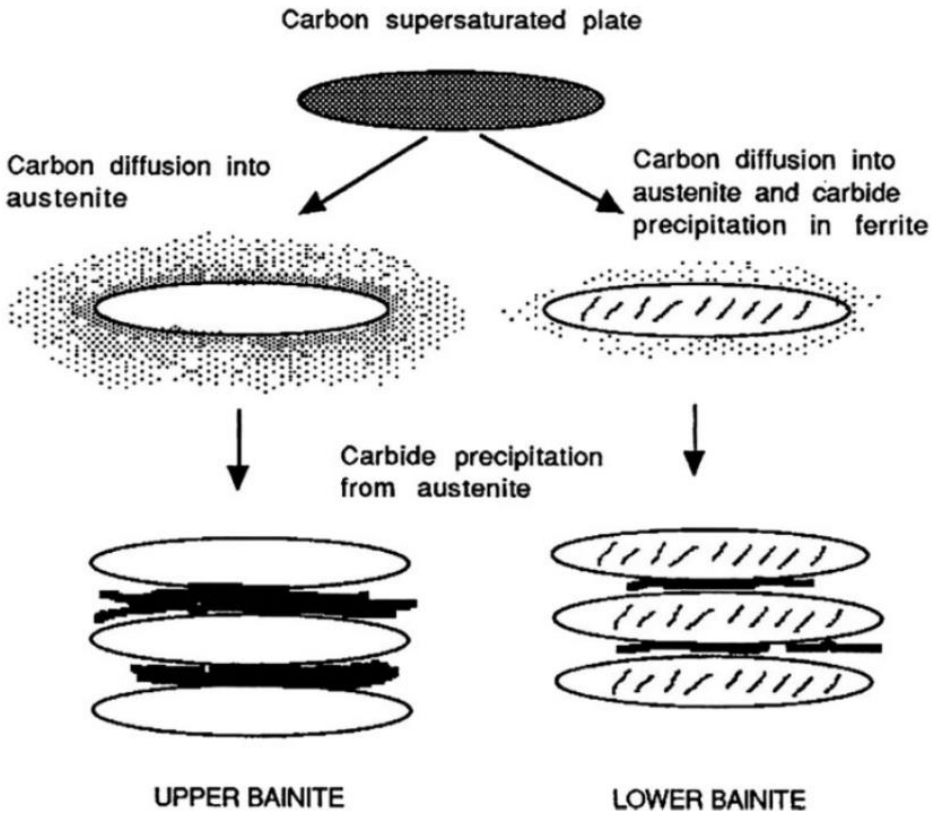

Figure 2-3: Representation of formation of upper versus lower bainite microstructures [37].

There are two methods that can be utilized to obtain bainitic microstructure. The first of these is executed by increasing the quantity of alloying elements. The better option is to increase the cooling rate of the plates. Although more equipment is needed, the second approach does not ruin the steel's weldability [48]. Mendoza *et al.* [47] conducted a study applying an accelerated cooling procedure on API grade 5L X70 steel plates, the chemical

composition of which is highlighted in Table 2-1. A bainitic and ferritic structure was obtained and displayed in Figure 2-4(a). The final rolling procedure began at approximately 1020 °C and finished at about 890 °C. Next, the resulting plates were quenched at 6 °C/s until 670 °C prior to cooling in air to room temperature. More images of the processed steel were collected, revealing ferrite and patches of pearlite. This is shown in Figure 2-4(b).

Table 2-1: Nominal composition of API 5L X-70 heats under study (in wt.%) [47].

C	Mn	Si	S	P	Al	Nb	Cu	Cr	Ni	Ti	Ca	N_2
0.037	1.50	0.14	< 0.003	< 0.015	0.03	0.09	0.27	0.26	0.16	0.010	0.0025	0.0040

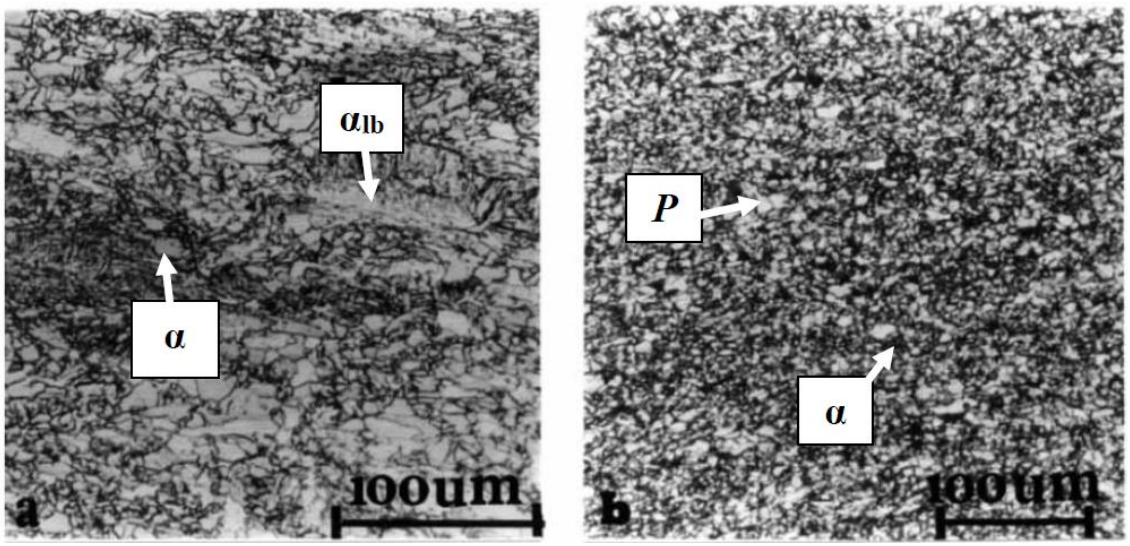

Figure 2-4: (a) SEM image of ferrite and bainite microstructure, (b) ferrite with patches of pearlite [47].

Another common and useful microstructural feature in HSLA pipeline steels is acicular (Widmanstatten) ferrite, seen in thick-walled pipes of X70 grade [68]. In three-dimension, acicular ferrite is characterized by a thin lenticular plate morphology and forms

when the austenite grain size is relatively large. When this criterion is satisfied, ferritic plates can nucleate in an intragranular manner on non-metal inclusions. The ferrite plates are not arranged parallel to one another, and the complex ordering can heighten X70's toughness. Hence, austenite grain size is an important parameter, as it determines the dominant microstructure. This argument is conveyed in Figure 2-5, which shows the influence of austenite grain size in controlling whether the bainitic or acicular ferritic microstructure prevails. Like the bainitic microstructure, acicular ferrite can also be obtained through higher rates of controlled cooling, as explained further in the next section. This leads to continuous yielding in HSLA steels rather than yield point elongation.

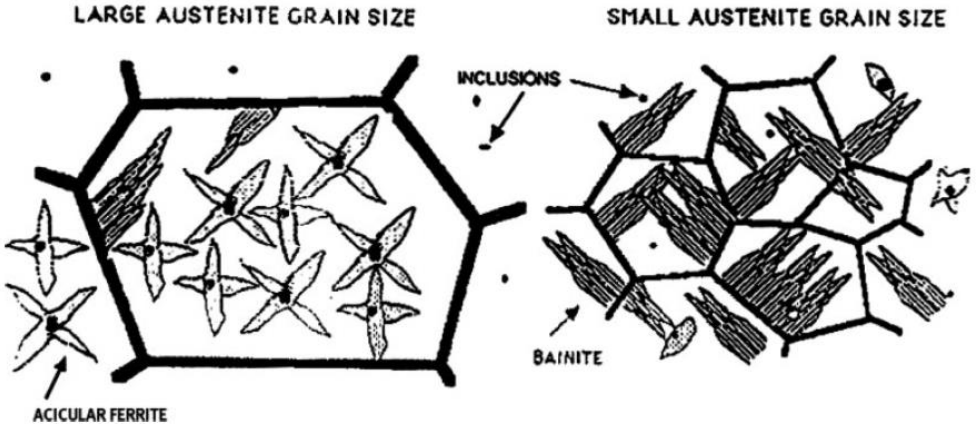

Figure 2-5: Illustration depicting the influence of austenite grain on microstructural evolution. Larger austenite grain size promotes acicular ferrite formation [69].

2.1.3. PROCESSING: TMCP AND ACC

Development of pipeline steels has been an active area of research over the last 50 years. The refinement of grains is the most effective means of increasing strength and toughness in HSLA steels, and this was first evident from the work of Hall [70] and Petch

[71]. In the 1960s, a cost-effective process called TMCP was explored and developed. This technique facilitates precise microstructural evolution, which ultimately enhances the hardening capacity and ductility of the steel [27, 30, 72]. TMCP considers the interactions of many mechanisms. This includes glide and climb of dislocations, recrystallization, grain growth, phase transformations, precipitation of microalloying elements, as well as particle coarsening and pinning. Whether each of these changes occurs dynamically or statically is of considerable significance.

In 1963, the first controlled rolling experiments were conducted [37]. Studies by Morrison [49] demonstrated it is essential to use low finishing rolling temperatures to refine the grains and improve properties. Controlled rolling with intentionally lowered rolling temperatures relative to conventional hot rolling is now widely used in microalloyed steel manufacturing [73, 74]. The initial objective of implementing this process was to obtain steel with refined polygonal ferrite grains; however, today the aim is to also incorporate acicular and bainitic microstructures [75].

Conventional hot-rolling and controlled-rolling techniques differ in the location at which ferrite nucleation takes place. In the former, ferrite nucleation only occurred at austenite grain boundaries, whereas in controlled-rolling, the nucleation of ferrite also occurs within the grains, fostering further grain refinement [76]. The conventional controlled-rolling process is a thermomechanical controlled process because both the temperature and deformation during hot rolling are carefully managed. Adequate control of the austenitic microstructure at the beginning of its phase transformation is provided,

avoiding its recrystallization. Ferrite grain refinement is achieved through two mechanisms when using this method. One mechanism involves forming fine recrystallized austenite grains when hot rolling at intermediate temperatures, and the other is the enhancement of ferrite nucleation by deformation of austenite below recrystallization temperature [73].

The first step in processing is controlling austenite grain size during soaking. This is achieved by managing the soaking temperature, assuring microalloying elements are taken into solution, since precipitates form after solidification during casting followed by cooling. This austenite grain size has an exponential relationship with this temperature [37]. The degree to which precipitates dissolves, resulting austenitic grain size, and cost of processing are aspects that must be carefully considered when selecting this temperature [73, 77].

The controlled rolling process itself has three stages, each step precisely modifying the austenite and ferrite grain morphologies [73]. Firstly, deformation takes place in the austenite recrystallization temperature range. Exceeding 1000 °C, deformation of austenite typically results in coarse recrystallized grain formation, which then undergoes transformation to coarse ferrite and upper bainite. Increasing strain decreases the austenite grain size produced via recrystallization. Higher strain is initiated by reducing rolling until a limit is obtained [78].

In the second stage of the controlled rolling process, deformation occurs in the unrecrystallized temperature range. The non-recrystallization temperature, T_{nr}, is an important measure here. T_{nr} denotes the start of static recrystallization inhibition when cooling between rolling passes [37]. A common way of determining the non-

recrystallization temperature is by simulation of successive rolling passes. The mean flow stress (MFS) can be plotted as a function of the inverse of the absolute temperature for every simulated pass [77]. The value of T_{nr} is the second derivative of the MFS curve. More specifically, deformation results when the material is subjected to temperatures of 1000 – 900 °C, refining the austenite grain size through dynamic recrystallization. These grains are elongated, forming pancake-like structures [79]. Enough strain can be established to create twins or deformation bands, increasing the number of nucleation sites for the transformation of austenite to ferrite or bainite. This leads to the formation of finer ferrite and is by and large one of the most essential features of TMCP [76, 80].

The final stage has the greatest impact on mechanical properties. In this step, deformation takes place in the two-phase region. Below the recrystallization temperature, deformation provides "warm-worked" austenite, also contributing to the development of fine ferrite. Rolling at a temperature slightly higher than Ar3 creates equiaxed ferrite grains, as well as a substructure. This substructure's morphology is caused by the deformation of newly formed grains. As previously discussed, precipitation of niobium carbide in lower temperatures of the austenite range plays a vital role in TMCP. In addition to delaying recrystallization, these carbides stabilize the deformed substructure [47].

As formerly mentioned, austenite's condition prior to transformation is a substantial factor in the final ferrite grain size, chiefly the grain size of austenite and number of potential ferrite nucleation sites. To account for the pancake-like, elongated grains, Priestner and de los Rios [81] proposed S_v, a term that represents the grain boundary surface

area per unit volume of austenite. The term incorporates both grain boundary and intragranular nucleation zones [74]. S_v is also known as the effective grain size. Austenite has a relatively high S_v value, meaning its capacity for ferrite nucleation is large. Final deformation takes place in the low temperature range of austenite, and recrystallization between rolling passes stops while maintaining work-hardening. Today, computers aid in numerous areas of steelmaking, and results from computational modelling facilitate the achievement of a small, homogenous ferrite grains (< 10 μm) [35, 82, 83].

Traditional API 5L X70 steel was manufactured using thermomechanical rolling with subsequent cooling in air [48]. Current processing techniques used on X70 employ relatively fast cooling rates and low coiling temperatures to achieve the useful microstructures previously mentioned in this review. Using appropriate ACC, strain-based design requirements can be satisfied, particularly the strain hardenability, toughness, and strength of X70 [27]. Coupling TMCP with ACC is beneficial as it changes the plate microstructure from FP to fine-grained bainite and ferrite [84, 85], increasing strength without diminishing the low temperature toughness. Moreover, incorporation of the ACC technique improves precipitation strengthening by niobium and vanadium carbides and nitrides [60].

A summary of the main TMCP and ACC stages, highlighting typical temperatures used and resulting features, is organized in Table 2-2 [32]. This is followed by Table 2-3 [32], which presents specific microstructures formed after applying different processing conditions.

Table 2-2: Overview of TMCP stages, typical temperatures, and features [32].

Processing Parameters		Range	Features
Rolling	Reheat Temp. (°C)	1140 – 1180	Dissolution of precipitates; Produce a fine, polygonal austenitic grain; Maintain within the range of T*nr*
	Reduction ratio (%)	40 – 75	
	Finishing Temp. (°C)	760 – 800	
ACC	Start Temp. (°C)	730 – 760	Enhances grain refinement of ferrite; Prevents formation of pearlite during cooling
	Cooling rate (°C/s)	20 – 50	
	Stop Temp. (°C)	150 – 400	
Tempering	Heat Temp. (°C)	600	Reduce excess hardness and residual stresses

Table 2-3: Microstructures obtained using different processing conditions [32].

API 5L	Processing	Microstructure
X70	TMCP	Polygonal Ferrite (PF) + Pearlite Band (P)
		Bainite (B)
	TMCP + QT*	Bainite (B) + Martensite (M) + Ferrite (F)
	TMCP + ACC + QT*	Fine-grained Bainite

* QT is the acronym for the quenching and tempering processing route.

2.1.4. MICROSTRUCTURE-PROPERTY RELATIONSHIPS

The properties of API 5L X70 pipeline steel result from the chemical composition and processing conditions, which govern the microstructural evolution [47]. For instance, the product's strength is dependent on the quantities of microalloying elements used and the rolling procedure. This includes the finishing temperature, which determines the amount of dissolved microalloying elements such as niobium. Of equal importance is the cooling rate applied after rolling [48]. There are specific standards that must be met when preparing the bodies of seamless and welded pipes. These measurements include yield strength, tensile strength, and elongation. The requirements for the tensile test results of X70 pipe grade are summarized in Table 2-4. PSL, EW, LW, SAW, and COW represent product

standard level, electric welded, laser welded, submerged arc welded, and combined welding, respectively.

Table 2-4: Requirements for the results of tensile tests for PSL 1 pipe [45].

Pipe grade	Pipe body of seamless and welded pipes			Weld seam of EW, LW, SAW and COW pipes
	Yield strength[a] $R_{t0.5}$ MPa (psi) minimum	**Tensile strength**[a] R_m MPa (psi) minimum	**Elongation** (on 50 mm or 2 in) A_f % minimum	**Tensile strength**[b] R_m MPa (psi) minimum
L485 or X70	485 (70 300)	570 (82 700)	c	570 (82 700)

[a] For intermediate grades, the difference between the specified minimum tensile strength and the specified minimum yield strength for the pipe body shall be as given in the table for the next higher grade

[b] For intermediate grades, the specified minimum tensile strength for the weld seam shall be the same value as was determined for the pipe body using footnote a).

[c] The specified minimum elongation, A , expressed in percent and rounded to the nearest percent, shall be determined using the following equation:

$$A_f = C\frac{A_{xc}^{0,2}}{U^{0,9}}$$

where

C is 1940 for calculations using SI units and 625 000 for calculations using USC units;

A is the applicable tensile test piece cross-sectional area, expressed in square mm, as follows:

- For circular cross-section test pieces, 130 mm² for 12.7 mm and 8.9 mm diameter test pieces; and 65 mm² for 6.4 mm diameter test pieces;
- For full-section test pieces, the lesser of a) 485 mm² and b) the cross-sectional area of the test piece, derived using the specified outside diameter and the specified wall thickness of the pipe, rounded to the nearest 10 mm²;
- For strip test pieces, the lesser of a) 485 mm² and b) the cross-sectional area of the test piece, derived using the specified width of the test piece and the specified wall thickness of the pipe, rounded to the nearest 10 mm²;

U is the specified minimum tensile strength, expressed in megapascals (pounds per square inch).

Figure 2-6 captures the evolution of HSLA steel studies, displaying the changes in processing conditions that have taken place over time and ultimately led to microstructures exhibiting useful properties, specifically the yield strength and toughness. It is clear from this figure that implementation of the accelerated cooling conditions is responsible for the

significant increases in strength of HSLA steels without detrimentally affecting the weldability. This result is virtually independent of composition [37, 77].

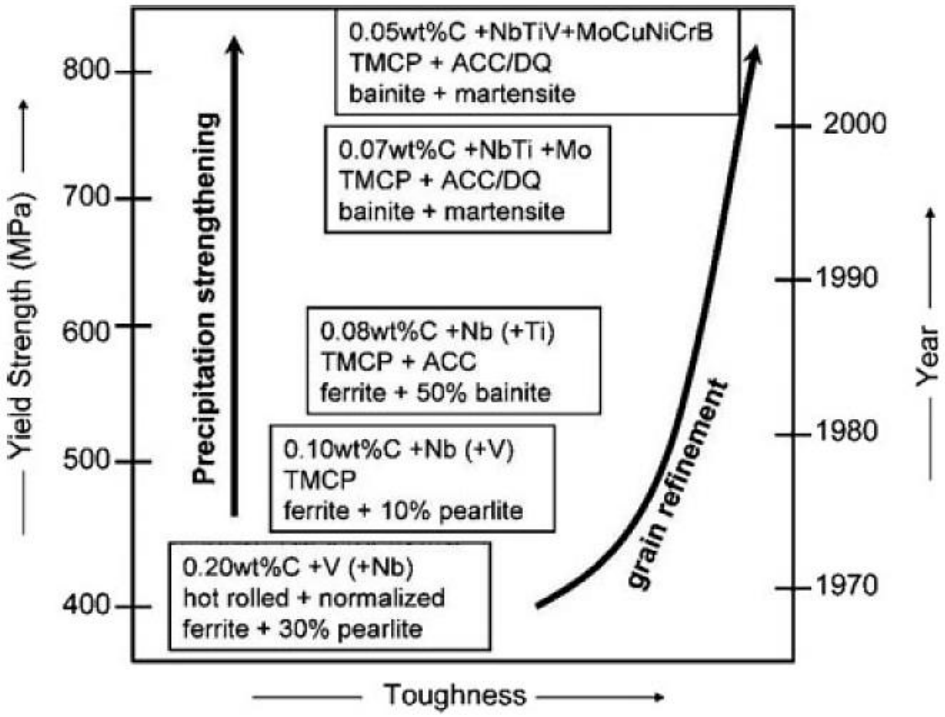

Figure 2-6: The development of pipeline steels. DQ represents direct quenching [37, 83].

2.2. X70 HIC-SUSCEPTIBILITY

The number following "X" in the API classification system is indicative of the steel's minimum yield strength requirement. For X70 grade, this value is 70,300 psi or 485 MPa. However, a tradeoff exists between steel strength and HIC-susceptibility. It has long been reported that as steel tensile strength increases, HIC-resistance decreases [1]. This section first presents the general concept of pipeline corrosion in sour-service environments, supported by presentation of the dominant electrochemical reaction scheme. Following this, the established means by which hydrogen migrates into steel structures in the HIC process is elucidated, as well as how HIC-susceptibility is identified and quantified in line pipe steels today via standard tests. Finally, the question of why X70 grade is HIC-susceptible is answered, highlighting the major metallurgical and environmental factors involved.

2.2.1. PIPELINE CORROSION FUNDAMENTALS

When steel pipelines undergo hydrogen embrittlement due to sour service exposure, electrochemical reactions have taken place. The inner pipe surface often contains both the anodic and cathodic areas, and the electrolyte completing the circuit is typically sourced from the oil and gas mixture transported. These fluids contain corrosive agents such as dissolved H_2S, CO_2, microbes, and/or other organic compounds [4]. Electrons are released via metallic dissolution at the anodic sites and transferred to cathodic sites where water is reduced to hydroxyl (OH^-) ions and hydrogen ions (H^+) can combine to form molecular gaseous hydrogen (H_2) [86]. When chloride (Cl^-) and oxygen (O_2) quantities are limited, the sulphide corrosion product (FeS) passivates the pipeline steel at relatively low temperatures

[87]. The common chemical reactions associated with HE of sour-service pipelines are shown in Figure 2-7 [4]. Atomic hydrogen produced by these reactions can recombine to form molecular hydrogen on the pipeline surface and diffuse off. Alternatively, these ions can travel into the steel and recombine at crystallographic defects [88, 89].

Anodic reaction:

$$Fe\ (s) \rightarrow Fe^{2+}(g)\ + 2e^{-} \qquad \text{(I)}$$

Cathodic reactions:

$$2H^{+}(aq) + 2e^{-} \rightarrow H_2\ (g) \qquad \text{(II)}$$

$$O_2\ (g) + 2H_2O\ (l) + 4e^{-} \rightarrow 4OH^{-}\ (aq) \qquad \text{(III)}$$

$$O_2\ (g) + 4H^{+}(aq) + 4e^{-} \rightarrow 2H_2O\ (l) \qquad \text{(IV)}$$

Overall corrosion reaction:

$$Fe(s) + 2H^{+}(aq)\ \rightarrow Fe^{2+}(aq)\ +\ H_2(g) \qquad \text{(V)}$$

Passive film formation:

$$Fe(s) + H_2S\ (g)\ \rightarrow FeS\ (s)\ +\ H_2(g) \qquad \text{(VI)}$$

Figure 2-7: Main electrochemical reactions occurring during hydrogen embrittlement of pipeline steel operating in sour-service conditions. (I) iron dissolution, (II) hydrogen reduction, (III) oxygen reduction in neutral and alkaline solution, (IV) oxygen reduction in acidic media, (V) net reaction, (VI) formation of a passive FeS film in the absence of Cl^- and O_2 [4].

2.2.2. EVALUATING HIC-SUSCEPTIBILITY OF PIPELINE STEELS

Recall HIC is a brittle material fracture mode occurring at stresses below yield [90]. The major steps specifically involved in the HIC-process are (i) H_2 gas evolution as a cathodic

reaction product during corrosion, (ii) hydrogen ion adsorption on the steel surface, (iii) subsequent diffusion of the ions into the steel, (iv) hydrogen ion accumulation at various metallurgical heterogeneities, which serve as internal hydrogen trapping sites, (v) H_2 gas production via ion recombination, facilitating (vi) crack initiation due to high internal gas pressure and (vii) crack propagation.

To identify and quantify material susceptibility to HIC, AMPP developed the standard TM0284 test for pipeline steels [91]. The methodology is applicable to line pipe with wall thickness ranging from 5 to 30 mm. The test involves immersion of unstressed coupons in synthetic seawater with H_2S at standard ambient temperature and pressure (SATP) and pH 4.8 – 5.4 for 96 hours. Next, the specimens are sectioned, polished, and etched such that cracks can be differentiated from laminations, scratches, inclusions, and discontinuities. Parameters known as the crack length ratio (CLR), crack thickness ratio (CTR), and crack sensitivity ratio (CSR) are calculated for each of the sections using Equations 1 – 3, and the averages are reported for each coupon [92]. In these equations, a (mm) is crack length, b (mm) is crack thickness, W (mm) represents section width, and T (mm) is the test sample's thickness. The CLR, CTR and CSR values must be < 15%, < 5% and < 2%, respectively, for acceptable steel HIC-resistance [93].

$$Crack\ length\ ratio: CLR = \frac{\Sigma a}{W} \times 100\% \tag{2.2}$$

$$Crack\ thickness\ ratio: CTR = \frac{\Sigma b}{T} \times 100\% \tag{2.3}$$

$$Crack\ sensitivity\ ratio: CSR = \frac{\Sigma (a \times b)}{W \times T} \times 100\% \tag{2.4}$$

2.2.3. X70 HIC-SUSCEPTIBILITY

X70 grade's HIC-susceptibility is attributed to various metallurgical and environmental factors. The metallurgical factors include the phases present, grain size, crystallographic texture, alloying elements, strength, segregation, strengthening precipitates, and shape of non-metallic inclusions [92]. The steel's susceptibility will also depend on environmental factors such as the partial pressures of H_2S and CO_2, temperature, electrolyte pH, and concentration of reactive ions such as chloride.

Recall X70 is typically comprised of a ferrite-bainite microstructure; however, can contain acicular ferrite, pearlite, martensite and retained austenite based on the microalloying and processing route employed [94, 95]. Some X70 microstructures are known to be more HIC-susceptible than others. Constituents with higher hardness undergo greater stress concentration at the hard phase-matrix interface, more readily causing hydrogen-trapping and potential crack initiation depending on the quantity accumulated [96, 97]. Phase hardness is reported to increase as follows: ferrite < pearlite < bainite < martensite, with hydrogen trapping efficiency increasing in the same order [96]. When comparing the primary phases of X70, Nanninga *et al*. found bainite and tempered martensite exhibit the highest HIC-susceptibility, whereas acicular ferrite demonstrates the best HIC-resistance [98]. Park *et al.* also reported the acicular ferrite microstructure is most effective at minimizing HIC [99], owing to its improved crack propagation inhibition in comparison to bainite, martensite, and dual phase [100]. The reduced crack propagation observed is attributed to hydrogen-trapping of finely dispersed carbonitride precipitates

and a high density of tangled dislocations. It is believed these traps distribute the hydrogen more uniformly, preventing hydrogen accumulation to critical concentrations necessary for the onset of HIC [97].

Furthermore, grain size in the ferrite matrix is known to impact HIC-susceptibility. Grain refinement of ferrite demonstrates enhanced HIC-resistance, believed to be a result of increased grain boundary area leading to higher hydrogen mobility [95]. In addition, since there is a tendency for hydrogen atoms to transport along grain boundaries, the grain boundary distribution should be one that minimizes HIC [4]. TMCP is often conducted to raise the number of low angle grain boundaries (LAGB) and special coincidence site lattice (CSL) boundaries because of their low energy and lower HIC-susceptibility when compared to high angle grain boundaries (HAGB) [101]. Both LAGB and CSLs are reversible trap sites, meaning at these sites it is less probable for hydrogen to reach the critical levels required for crack initiation [102]. However, raising the number of CSL boundaries is challenging to achieve in HSLA grades due to reduced stacking fault. This type of boundary is often associated with twinning [103].

It should be clarified that hydrogen traps are classified as either reversible or irreversible depending on if the hydrogen is easily released or tightly bound. This is distinguished using activation energy, or energy required for hydrogen atoms to escape the trapping site. These values are obtained through thermal desorption spectroscopy (TDS) analysis. Lower activation energy values are characteristic of reversible traps, which include grain boundaries, dislocations, and micro-voids. Conversely, traps with higher activation

energies such as various inclusions are considered irreversible at ambient temperature [95]. It is reported that irreversible traps are involved in crack initiation, whereas reversible traps accelerate crack propagation [6, 95].

The main secondary phases in X70 include complex (Fe, Mn) sulphide inclusions, complex Al-Ca-Si-Mg oxides and oxysulfides, and fine scale Nb, Ti and V carbonitride precipitates [104]. Of these phases, the most detrimental are reported to be Al_2O_3, Al-Ca-Si oxides, and Mn sulphides, as they are common crack initiation sites in X70 [96]. This is in part due to inclusion-matrix incoherency, which facilitates hydrogen accumulation at this interface. HIC-susceptibility is also known to increase with a higher number of relatively large inclusions and clusters [93, 96]. Additionally, specific inclusion morphologies can promote HIC, particularly the elongated MnS stringer type known to decrease pipe body fracture toughness. Moore and Warga demonstrated that deoxidation increases the solubility of sulphur, leading to increased formation of the stringer morphology [105]. When comparing the HIC behavior of X60 and X70 pipeline steels, Mohtadi-Bonab *et al.* found X70 was more HIC-susceptible due to the presence of stringer-shaped MnS inclusions [6]. An additional factor driving this was the central segregation zone, reported to contain a high concentration of Mn, Si, and S, which led to increased hydrogen accumulation and crack initiation. Elemental segregation can also facilitate the formation of hard phases like bainite and martensite at this centerline region, further contributing to HIC-risk. This region generally features larger grains as a result of exposure to higher temperatures for longer periods of time [106].

2.2.4. SUMMARY

The main factors driving HIC-susceptibility of X70 are the presence of elongated manganese sulfide stringer type inclusions in addition to the chemical composition, hard phase segregation, and coarser grains in the central segregation zone. The existence of a higher proportion of relatively HIC-susceptible microstructures including bainite and martensite decrease the material's HIC-resistance further. Also, it is necessary to consider how the grain boundary character and distribution present impacts HIC-risk. It is well documented that grain boundaries are the preferential diffusion path for hydrogen, and the beneficial LAGB and CSL boundaries are challenging to obtain when manufacturing HSLA steels.

2.3. MICROSTRUCTURAL HYDROGEN-MAPPING IN STEELS

Hydrogen is challenging to map in materials. Its low mass along with high diffusivity in the vicinity of thermal, mechanical, and compositional gradients makes accurate tracking difficult [107]. This is further hindered by embrittlement effects existing even at low concentrations. Specifically, in steels, the direct observation of hydrogen is challenging due to its low solubility and positive heat of solution [108]. HE processes involve hydrogen-defect interactions occurring at many different length-scales, necessitating multi-length scale mapping of materials of interest.

Three-dimensional mapping of the hydrogen distribution is especially important as hydrogen segregation is dependent on various factors, including the presence of potentially hidden microstructural features, stress triaxiality, and the material's cross-sectional area [107]. To date, it remains difficult to measure the precise location of hydrogen atoms [109], causing HE to be a research area of immense debate. Lack of a mechanistic understanding of HE delays the development of more corrosion-resistant steels for numerous applications.

Many methodologies have been used for microstructure-sensitive hydrogen tracking. These techniques include thermal desorption spectroscopy (TDS), hydrogen permeation (HP) measurements, secondary ion mass spectroscopy (SIMS), neutron radiography, and atom probe tomography (APT) [107]. Herein each of these methods are discussed, highlighting their associated spatial resolution, main advantages, and limitations. Focus is placed on advancements in hydrogen-tracking enabled by coupling electrochemical pre-charging with atom probe tomography.

2.3.1. THERMAL DESORPTION SPECTROSCOPY

TDS can be used to assess the global hydrogen content within steel. More specifically, the hydrogen quantity and de-trapping activation energy associated with various microstructural features in steels are determined by applying different heating rates [107]. A TDS profile contains desorption peaks that have temperatures and shapes influenced by trapping energy as well as diffusion [1]. While this technique provides hydrogen desorption rate profiles that are microstructure-sensitive, a major limitation of TDS is that it fails to deliver spatially resolved mapping [107]. TDS generates macroscale data related to hydrogen desorption as the origin of the hydrogen is from all potential trapping sites within the specimen under study.

A schematic representation of a hydrogen desorption profile obtained using TDS is shown in Figure 2-8. The relative trapping contributions from various specific microstructural constituents often cannot be easily realized with TDS [109]. For example, it is challenging to utilize TDS to distinguish trapped hydrogen within precipitates versus at matrix-particle interfaces. Thus, using this hydrogen-mapping method can complicate the achievement of a clear understanding of the roles of various trap types such as inclusions, grain boundaries and dislocations. In addition, this method assumes that increased hydrogen bonding energy consistently causes higher hydrogen adsorption capacity. This does not always occur, as studies have demonstrated strong hydrogen traps, such as TiC particles in iron, adsorb limited hydrogen quantities when cathodically charged [23, 110].

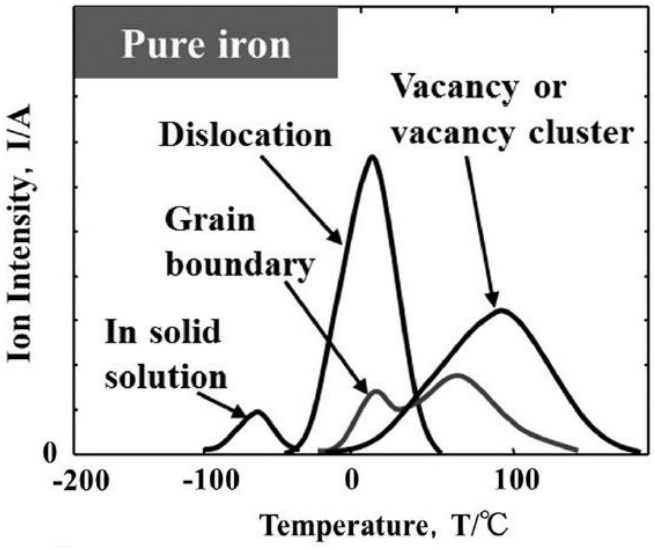

Figure 2-8: Schematic of a hydrogen desorption profile achieved via TDS [107].

2.3.2. ELECTROCHEMICAL HYDROGEN PERMEATION

HP measurements quantify the diffusible hydrogen concentration in metals, and are commonly employed as a non-intrusive, indirect assessment of internal corrosion in the oil and gas industry [111]. The amount of atomic hydrogen permeating through a metal surface is measured by recording the steady state permeation current needed to oxidize hydrogen atoms in a sealed electrochemical cell [112]. The most common cell utilized for these tests is the Devanathan-Stachurski cell, which features a metal membrane sandwiched between two individual electrochemical cells. This is schematically represented in Figure 2-9. In one cell, a cathodic potential or current is applied, causing hydrogen adsorption on the metal surface. The adsorbed hydrogen is absorbed into the metal bulk and diffuses to the opposite surface. In the adjacent cell, an anodic potential is used to oxidize the hydrogen [113]. Major drawbacks of using hydrogen permeation measurements to quantify hydrogen in steels are

that, like TDS, this method fails to provide spatial information and falsely assumes greater hydrogen bonding energy will always lead to more hydrogen adsorption capacity [114].

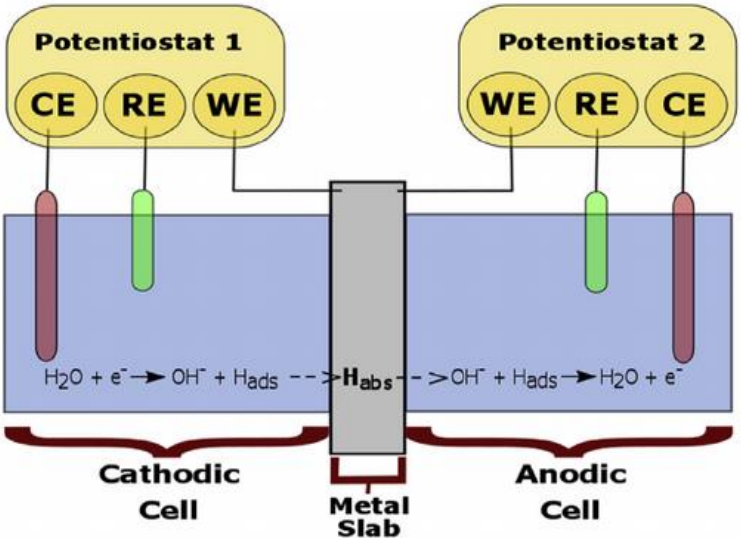

Figure 2-9: Schematic of Devanathan-Stachurski cell for hydrogen permeation measurements [113].

2.3.3. SECONDARY ION MASS SPECTROMETRY

SIMS is today's most sensitive surface analysis technique and is capable of directly imaging hydrogen in steels [115]. This destructive method works by holding the steel under ultra-high vacuum and bombarding the surface with a high energy ion beam of an element not present in the specimen. The material is sputtered away and subsequently analyzed by a mass spectrometer, which provides the chemical composition [107]. SIMS has been applied as a quantitative three-dimensional mapping method for trapped hydrogen; however, the method cannot deliver the accurate location of hydrogen atoms [116]. The x-y plane spatial resolution is a few micrometers, and for the depth or z direction the

resolution is several tens of nanometers. In addition, it can be challenging to map hydrogen in ferritic steel due to high diffusivity, even with cryogenic SIMS combined with silicon sputtering and cold-trapping methods involving $N_{2\ (l)}$ [107].

2.3.4. NEUTRON RADIOGRAPHY

Neutrons interact strongly with light elements such as hydrogen and pass easily through heavier constituents. In other words, hydrogen exhibits a relatively high neutron attenuation coefficient, making neutron radiography another useful hydrogen mapping technique [117]. This method is fast and non-destructive. It works by firing a neutron beam at an alloy of interest. A portion of this beam interacts with the sample, strikes a neutron imaging contrast agent, and generates an attenuation pattern or neutron radiograph. The technique has been employed for in-situ studies of hydrogen absorption and diffusion in zirconium alloys [118] and hydrogen effusion in austenitic stainless steels [119]. The main limitations associated with neutron radiography are its spatial and temporal resolutions. The spatial resolution is limited to approximately 20 – 30 μm while the time resolution is about 28 seconds and 14 seconds for two- and three-dimensional analyses, respectively [107].

2.3.5. ATOM PROBE TOMOGRAPHY

The most site-specific hydrogen analyses can be conducted by coupling hydrogen pre-charging with APT. This nanoscale analytical characterization technique involves three major steps. The first is sample preparation, where a small, needle-shaped specimen is

obtained through electropolishing or a combination of electropolishing and focused ion beam milling. This is done to maximize the electric field strength for field evaporation of the specimen. Specifically, the tip radius is inversely proportional to the electric field strength achieved. The next step is data acquisition through field evaporation, a process controlled by high-voltage or laser pulses, gradually destroying the sample. Adsorbed ions are counted by a detector that records impact position and time of flight of each hit. Finally, the data is reconstructed and analyzed to generate an atom-by-atom three-dimensional model of the evaporated volume, providing structure and composition information with sub-nanoscale spatial resolution and near ppm elemental sensitivity [120].

To date, APT offers the maximum attainable spatial and chemical resolutions in the field of hydrogen mapping. The highest possible spatial resolution is at the lattice size level, but is dependent on the measurement direction, specimen chemistry, and temperature [1]. Many studies have demonstrated APT's ability to resolve the positions of single hydrogen atoms, making it the top candidate for accurately determining hydrogen trapping locations of various microstructural features [1, 107, 108, 116]. Due to the residual hydrogen in the atom probe chamber, deuterium is commonly used for charging prior to subsequent characterization with APT. This is advantageous due to deuterium's relatively low isotopic abundance, facilitating the differentiation of deliberately introduced and residual hydrogen in the instrument chamber [108]. One major challenge experienced by researchers using this method is undesired hydrogen recombination or mobility, leading to inaccurate positioning of the hydrogen [107]. However, recent advances incorporate cryogenic and/or

vacuum transfer systems, enabling higher hydrogen yields and more accurate mapping [121]. Another limitation associated with APT when working with multiphase materials is the variability in evaporation fields, which leads to an apparent expansion or compression of atomic positions known as the local magnification effect [122].

2.3.6. SUMMARY

Today, many hydrogen mapping strategies are available to better understand HE mechanisms in steels. The technique selected by the researcher primarily depends on the desired length scale for the characterization (i.e., sample dimensions). For instance, a more global or relatively large-scale quantification of hydrogen can be achieved through TDS and/or HP, whereas more localized mapping is possible through SIMS, neutron radiography, or APT. It is also critical to consider the resolutions necessary to meet specific research objectives. APT offers the best spatial and chemical resolution to date, making this method the best available tool for determining specific trapping locations associated with a variety of microstructural features. Combining several of these strategies would enable quantitative, three-dimensional, multiscale, kinetic hydrogen-mapping in steels with high spatial resolution [107].

2.4. EFFECTS OF CARBONITRIDE PRECIPITATES ON HIC

The most beneficial of the main secondary phases in X70 are argued to be nitrides and carbides of Nb, V, and Ti, which are reported to play a dual role in pipeline steels. In addition to enhancing mechanical properties through precipitation strengthening, they tend to lower the diffusion of hydrogen in the steel lattice through irreversible hydrogen trapping [4]. Recall a hydrogen trap is categorized as irreversible when the activation energy is relatively high, and elevated temperatures are required to release the hydrogen. 850 °C and 450 °C are typical hydrogen release temperatures used to distinguish irreversible and reversible hydrogen-traps, respectively. Table 2-5 summarizes the activation energies of different hydrogen trap sites in steel, where values corresponding to various inclusions are higher than those associated with reversible sites.

Table 2-5: Hydrogen Trap Sites and Activation Energies

Hydrogen Trap Site	Activation Energy, E_a (kJ/mol)	Character	Reference
Grain Boundary	18 – 59	mixed	[123-125]
Dislocation	19.2 – 29.9	reversible	[124, 126]
Microvoid	27.6	reversible	[124]
MnS Interfaces	72.3	irreversible	[127, 128]
Al_2O_3 Interfaces	78.96	irreversible	[128]
TiC Interfaces	87 – 95	irreversible	[128, 129]
Incoherent Ti Precipitates	86 – 116	irreversible	[129]
Coherent Ti Precipitates	46 – 59	irreversible	[129]
VC Precipitates	34	irreversible	[129]
Precipitate Interfaces	23 – 48	mixed	[129]
Incoherent NbC Precipitates	63 – 68	irreversible	[129]
Incoherent NbN Precipitates	100 – 143	irreversible	[129]

It is challenging to understand the specific roles of Nb, V and Ti inclusions in crack initiation and propagation due to the nature of hydrogen and the limited number of

techniques that are suitable for investigating HIC initiation. Consequently, the role of these traps in hydrogen damage remains controversial within the scientific community today. This section explores documented effects of Ti and Nb (C,N) on HIC.

2.4.1. Ti-BASED PRECIPITATES

Carbides of titanium are frequently mentioned to enhance the HIC-resistance of steels [130, 131]. For instance, microalloying with Ti has been observed to aid in conversion of MnS into less damaging TiS and $Ti_4C_2S_2$ precipitates [4]. Also, precipitate-matrix coherency has been shown to influence the hydrogen-trapping capacity of titanium carbides. Pressouyre and Bernstein [126] revealed incoherent TiC precipitates demonstrate higher hydrogen-trapping capacity compared to coherent carbides. This is believed to be attributed to a relatively high concentration of octahedral carbon vacancies within incoherent TiC particles when compared with less coherent particles [23]. The activation energy for hydrogen from coherent TiC precipitates was 46 – 59 kJ/mol, and this value ranged from 82.7 – 116 kJ/mol for incoherent precipitates [132].

Inclusion size also plays an important role in HIC-mitigation. Small titanium-based particles are reported to improve HIC-resistance of steels [133]. Beidokhti *et al*. found that the dispersion of fine titanium carbonitrides in the steel matrix redistributed absorbed hydrogen away from relatively detrimental trapping sites, permitting accumulation of a higher bulk hydrogen concentration before cracking initiation occurred [134]. Moon *et al.* conducted HIC testing on X70 hot-rolled steel and demonstrated preferential HIC-propagation along larger (Nb, Ti, V)(C,N) particles (> 7.5 μm) generated at the centerline

after Ti was added to the steel [100]. These coarse Ti precipitates were highly concentrated at the centerline, as this region is the final solidification zone during continuous casting.

To build on the mechanistic understanding of HIC, identification of the hydrogen-trapping location(s) relative to Ti-based particles is critical. Because of its superior spatial resolution, APT is commonly used to determine hydrogen-trapping locations associated with a variety of microstructural heterogeneities. Use of this technique is often coupled to a charging pretreatment. In 2010, Takahashi *et al*. published their work showcasing the first atomic-scale direct observation of hydrogen trapping sites at nano-sized (2 – 6 nm diameter) TiC platelets in steels using APT [108]. A deuterium (D_2) gas charging pretreatment was carried out prior to subsequent APT characterization of the steel needles. Proposed trapping sites included the matrix-particle interface, particle core, and/or the surrounding strain field. After IVAS reconstruction and analysis of the obtained data, the D atoms were observed on the broad interface between the steel matrix and TiC platelets. However, no D atoms could be observed in precipitates < 3 nm, supporting that trapping location and activation energy vary with precipitate size. Given these results, they discussed two possible deep trapping locations: the carbon vacancy on the precipitate surface, and the misfit dislocation core at the interface. Drawing conclusions from their results is challenging due to limited deuterium yields.

In recent years, many advances have been made by integration of cryogenic and vacuum transfer systems from various instruments used for APT sample preparation and/or the pre-charging setup. Incorporation of such systems have been found to increase the deuterium yield in charged specimens. Additionally, the stoichiometry of the TiC

particles is difficult to determine due to overlap of the carbon and titanium ions at 24 atomic mass units [135].

2.4.2. Nb-BASED PRECIPITATES

NbC and NbN are argued to have a higher hydrogen trapping capacity than any Ti- or V-based precipitates, as determined by TDS activation energy measurements [129]. Zhang *et al*. used cathodic hydrogen pre-charging, slow strain rate testing (SSRT), and NanoSIMS to investigate the role of NbC precipitates in hydrogen embrittlement of a nickel-based superalloy. Large cracks were discovered in fractured coarse carbides and regions of agglomerated carbonitrides. Their findings suggested that ensuring the inclusion sizes are relatively small and do not agglomerate could prevent crack initiation at such sites, and therefore aid in HIC-mitigation [114]. The role of NbC size on HIC of HSLA steels was studied further by Shiqi *et al*. Their HIC test and hydrogen permeation results support that Nb microalloying (0.055 wt.%) significantly improved the material's HIC-resistance, and the steel featuring nanoscale Nb precipitates exhibited higher HIC-resistance than the steel with larger (100 – 200 nm diameter) precipitates. The NbC particles did not initiate cracks and were found to reduce intergranular cracking by increasing the hydrogen-trap density and hindering hydrogen aggregation [136].

A more recent study elucidates the dual role of nanosized NbC precipitates in HE susceptibility of steels [7]. In this work, the influence of nanoscale (approximately 10 nm diameter) spherical NbC particles on HE was studied via SSRTs, HP testing, APT, and microstructural examination. Consistent with previous research work [136], HE-susceptibility declined as the number of NbC particles increased. The beneficial functions

highlighted include the alleviation of hydrogen accumulation to other areas via hydrogen-trapping by both NbC and additional prior austenite/martensite grain boundaries resulting from NbC precipitation. Secondly, NbCs reduced the proportion of Σ3 boundaries and pinned movable hydrogen-dislocation Cottrell atmospheres. One harmful role discussed was the reduction of the {111}//ND texture, which promoted hydrogen-assisted fracture by reducing crack propagation resistance; however, the beneficial effects were reported to outweigh this single effect. The effects of NbC precipitates on the HE of the martensitic steel under study are summarized in Figure 2-10 [7].

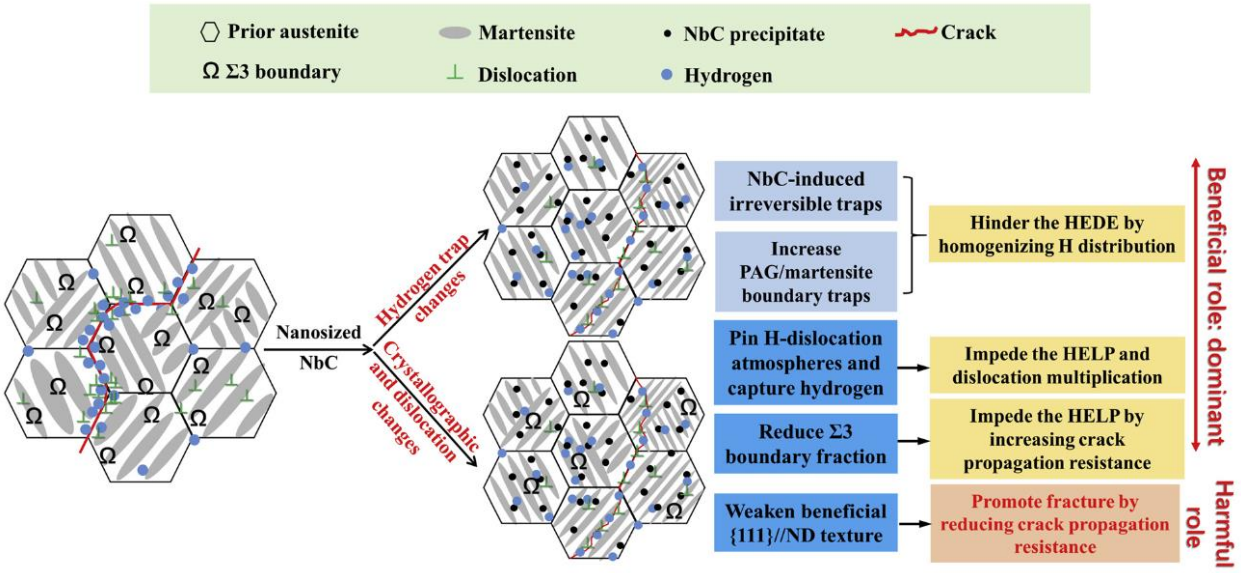

Figure 2-10: Schematic illustrating the effects of NbC precipitates on HE in a martensitic steel [7].

The relatively high hydrogen trapping capacity associated with NbC may be attributed to the existence of numerous trapping sites with different activation energies, such as the precipitate-ferrite interface, coherency strain region surrounding the precipitate, and crystallographic defects within the precipitate [137]. The hydrogen trapping

sites relative to Nb-based particles are a subject on ongoing debate in the scientific community. A small-angle neutron scattering (SANS) study on NbC precipitates by Ohnuma *et al*. [138] found hydrogen-trapped both inside the semi-coherent nanoscale NbCs and at their particle-matrix interfaces after electrolytically charging a 97.62Fe-0.23C-0.25Nb-1.90Ni (at.%) steel. Their SANS instrument is reported to detect trapped hydrogen content as low as a few ppm by weight. Wei *et al*. TDS studies claim that hydrogen trapped by incoherent carbonitrides during cathodic charging is likely in the precipitates rather than at the particle-matrix interfaces [23]. However, more recent APT studies showed deuterium trapping at carbide-ferrite interfaces in larger (approximately 20 nm diameter), incoherent NbC precipitates after electrolytic charging of a ferritic Nb-bearing low-carbon steel [109]. Using IVAS, they analyzed regions of interest through the precipitate centers, and confirmed peaks in the deuterium concentration aligned with the edges of the NbC profile. More APT studies should be carried out to confirm these findings, as this information is vital for enhancing the design of hydrogen embrittlement resistant HSLA steels.

2.4.3. SUMMARY

Generally, inclusions are harder than the pipeline matrix. This often creates incoherent particle-matrix interfaces, which tend to increase hydrogen trapping [139]. A greater degree of coherency has been found to lower the activation energy associated with the site [140, 141]. Typically, the more coherent the particle-matrix interface, the more likely the material will resist crack initiation and propagation. The shape, quantity, size, distribution, and stoichiometry of the inclusions will also affect HIC-susceptibility of the

steel. When inclusions are elongated, HIC-resistance is reduced. Mechanistically, it is widely accepted that the hydrogen preferentially gathers at the elongated inclusion's edges, where the stress concentration is higher. Hydrogen migrates into the interfacial voids, elevating the pressure under high strain, resulting in crack formation [142]. Also, a high number of relatively large precipitates or clusters are reported to pose higher HIC-risk [93, 96]. Precipitate stoichiometry may also influence hydrogen-trapping location(s) [143].

It is generally assumed inhibiting hydrogen diffusion using nanoscale carbides as H-traps is an effective means of reducing steel HIC-susceptibility. While the beneficial effects of Ti-based precipitates have been thoroughly documented [20, 21, 23, 144, 145], there remains a lack of adequate research on Nb carbonitrides and their influence of HIC. To manufacture X70 with improved HIC-resistance, steel manufacturers need to know what quantity of Nb is optimal in creating effective irreversible hydrogen traps. More specifically, it is critical to determine the best NbC, NbN, Nb(C,N) size distribution for mitigating HIC. Engineering X70 with a wide distribution of nanoscale Nb carbonitrides has potential to achieve this via establishment of a more uniform hydrogen profile in the steel, lessening diffusion and aggregation of hydrogen at more susceptible areas such as elongated MnS inclusions.

Also, the specific hydrogen trapping locations relative to NbC, NbN and Nb(C,N)s are a subject of ongoing debate. Specifically, whether the hydrogen is trapped within the precipitate and/or at the steel-precipitate interface remains to be resolved. This information is vital for improving the HIC-resistance of X70 steel for sour-service oil and gas applications. The exact site can be realized by incorporating recently developed

cryogenic and vacuum sample preparation transfer technologies into the APT methodology, which have been shown to increase deuterium yields [121].

2.5. ELECTROCHEMICAL ACTIVITY OF NbC and NbN PHASES

Many studies support the galvanic couple effect as the main cause for corrosion initiation for a variety of inclusion types in carbon steel, including: MnS [146-148], Al_2O_3 [149], MnS- Al_2O_3 [150], (Mn,Ca)S-(Al,Ca)O [151], (Ti,Nb)N [152], and $MnCr_2O_4$ [153]. Understanding the mechanism of localized corrosion initiation induced by Nb-based precipitates may aid in improving the corrosion resistance of HSLA steels such as X70 [154].

Clarification of the electrochemical difference between NbC or NbN and the surrounding steel matrix has previously been demonstrated by potentiodynamic polarization measurements of Nb-coated steels. For example, Oruela *et al*. studied the corrosion resistance of NbC coatings formed on AISI 1045 steel via thermo-reactive diffusion deposition [155]. The percentage of ferroalloy (with chemical composition of 30.82Fe-0.04C-63Nb-1.5Si-0.8Mn-3.8Al-0.04P (wt.%)) in the reaction medium was varied and the corrosion resistance of each generated coating was compared to the steel substrate. After conducting potentiodynamic polarization measurements in 3.0 wt.% NaCl at room temperature, it was found that the corrosion potential associated with the NbC coated steels was higher than that of the uncoated steel. The researchers attribute these findings to Nb oxide layers on the coated surface, the presence of which was confirmed by XPS.

The corrosion potentials and potentiodynamic polarization curves are summarized in Table 2-6 and Figure 2-11, respectively. The names of the samples are based on the percentage of the ferroalloy used in the thermo-reactive diffusion deposition process. For example, 1045-Nb-8 refers to 8 wt.% of the ferroalloy used for the NbC coating deposition

on the 1045 steel surface. Note that the reference electrode used for their polarization experiments was the saturated calomel electrode. The corrosion potentials of all NbC-coated systems were higher than that of the uncoated steel, implying the coating improves corrosion resistance. In addition, the corrosion current density was found to decrease slightly as the percentage of ferroniobium increased.

Table 2-6: Corrosion potentials of NbC coatings deposited on AISI 1045 steel [155]

Sample	Corrosion potential (mV)	Current density (mA/cm^2)
1045	− 832 ± 36	5.97E−05 ± 2.59E−06
1045-Nb-8	− 669 ± 39	4.32E−05 ± 1.63E−06
1045-Nb-12	− 665 ± 42	3.61E−05 ± 3.66E−06
1045-Nb-16	− 673 ± 36	3.58E−05 ± 3.13E−06
1045-Nb-20	− 671 ± 31	3.56E−05 ± 2.82E−06

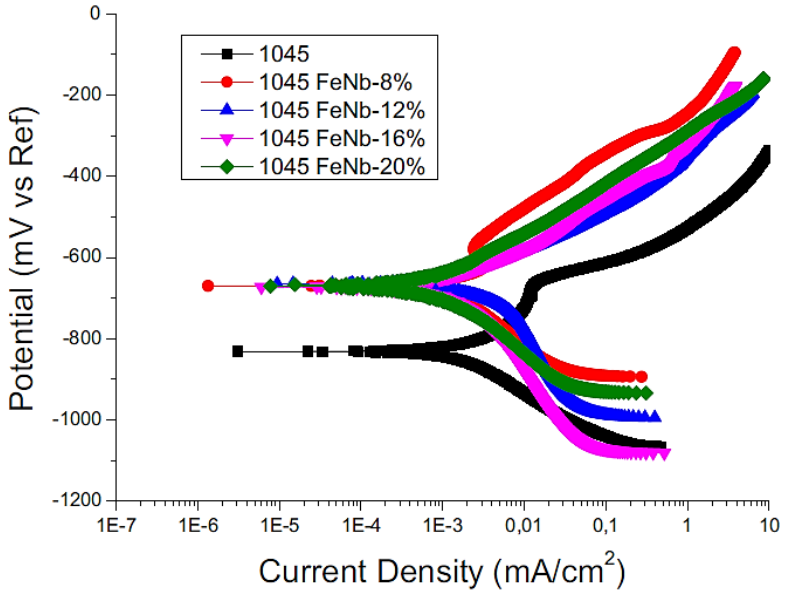

Figure 2-11: Potentiodynamic polarization curves of NbC coatings deposited on AISI 1045 [155]

These findings were later confirmed by the work of Fernandes *et al.* [156]. Their work involved potentiodynamic polarization tests in 3.5 wt.% NaCl at room temperature. A summary of the electrochemical parameters and potentiodynamic polarization data are

presented as Table 2-7 and Figure 2-12, respectively. At negative (cathodic) potentials, the curves are similar. The NbC-coated system yielded a more positive corrosion potential value as well as a lower corrosion rate for applied potentials less than 250 mV. The curves are also similar at elevated anodic potentials > 250 mV, featuring a nearly equal (approximately 60 mA/cm^2) current density. Beyond this potential, both the substrate and NbC coating experienced increased corrosion rate.

Table 2-7: Electrochemical parameters of NbC coated and uncoated AISI 52100 steels [156]

Sample	Corrosion potential (mV)	Current density (A/cm^2)	βc, (V/dec.)	βa, (V/dec.)	Corrosion rate (mm/year)
AISI 52100	− 725	8.1×10^{-6}	0.339	0.073	0.070
AISI 52100 + NbC	− 423	4.3×10^{-6}	0.372	0.089	0.037

* **βc** and **βa** are representative of the cathodic and anodic Tafel constants, in Volts/decade, respectively.

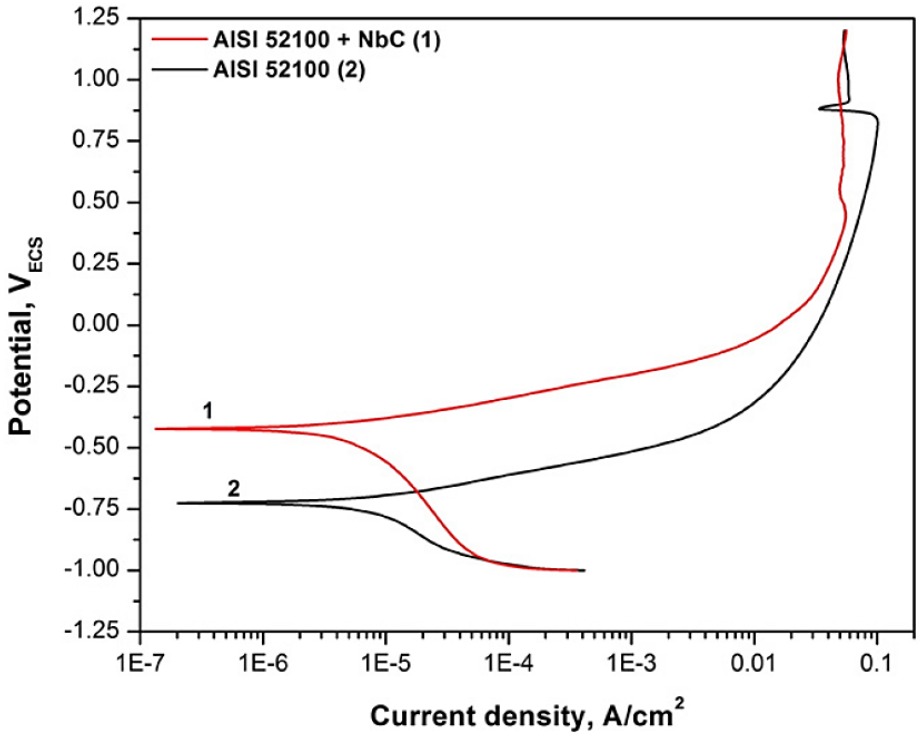

Figure 2-12: Potentiodynamic polarization curves in 3.5 wt.% NaCl for NbC-coated and uncoated AISI 52100 steels [156]

Similarly, NbN coatings have been added to various grades of steel and subsequently tested via potentiodynamic polarization measurements to reveal differences in the corrosion potentials. Wang *et al*. applied a NbN coating via plasma surface diffusion alloying on the surface of AISI 304 stainless steel [157]. The NbN surface layer was 8 – 9 μm thick. The electrochemical parameters obtained and potentiodynamic polarization curves of the uncoated and NbN-coated 304 stainless steels in 0.05 M H_2SO_4 and 2 ppm F^- solution at 70 °C purged in different atmospheres are presented in Table 2-8 and Figure 2-13. The Nb-based coated steel features a more positive corrosion potential and lower current density than that of the uncoated material in both environment types.

Table 2-8: Electrochemical parameters of NbN-coated and uncoated 304 stainless steels [157]

Sample	Purged with H_2		Purged with air	
	Corrosion potential (mV)	Current density (μA/cm²)	Corrosion potential (mV)	Current density (μA /cm²)
Uncoated 304	− 347	21.204	− 319	13.453
NbN-coated 304	100	0.127	143	0.071

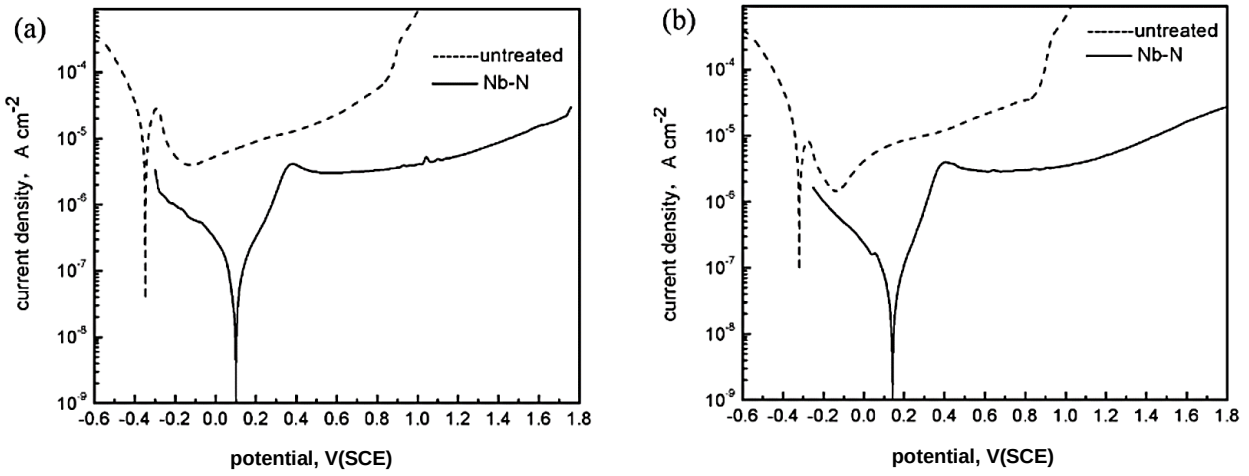

Figure 2-13: Potentiodynamic polarization curves of untreated and NbN 304 stainless steel in 0.05 M H_2SO_4 + 2 ppm F^- solution at 70 °C purged with (a) air and (b) H_2 [157].

A similar phenomenon was observed more recently by Fonseca *et al.* [158]. Their research work involved magnetron sputtering of Nb and Al targets in an Ar/N_2 atmosphere onto 316L stainless steel substrates, and subsequent electrochemical characterization. Specifically, potentiodynamic polarization measurements were carried out in 3.5 % (m/v) NaCl to assess the corrosion performance of the NbN coatings. Various electrochemical parameters from the NbN-coated and bare steels are summarized in Table 2-9 and followed by polarization curves displayed in Figure 2-14. Likewise, the NbN coated steel featured a higher corrosion potential than the bare 316L substrate. Additionally, the passivation current density reported for the NbN coated steel was two orders of magnitude lower than for the bare AISI 316L stainless steel.

Table 2-9: Electrochemical parameters of NbN-coated and uncoated AISI 316L stainless steel [158]

Sample	Corrosion potential (mV)	Transpassivation potential (mV)	Passivation current density (A/cm^2)
AISI 316L	-408 ± 13	710 ± 20	$(1.05 \pm 0.37) \times 10^{-5}$
AISI 316L + NbN	-231 ± 15	348 ± 8	$(4.95 \pm 0.71) \times 10^{-7}$

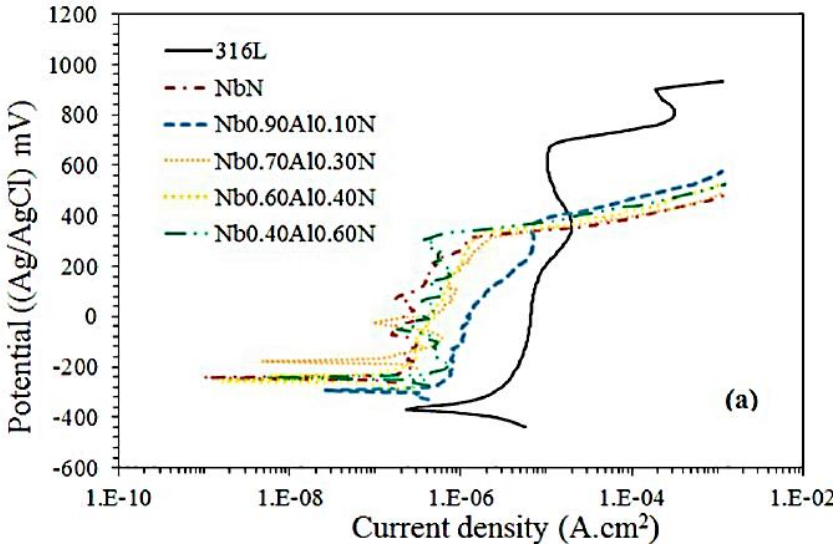

Figure 2-14: Potentiodynamic polarization curves for as-deposited NbN films and bare AISI 316L stainless steel [158]

To validate the galvanic couple effect in Fe-NbC and Fe-NbN coupled-systems, it is necessary that more research be carried out. Further studies should be conducted in electrolytes that better simulate the environments sour-service X70 pipeline steel operate in. If NbC and NbN precipitates serve as cathode materials when galvanically coupled to the X70 matrix, they can generate hydrogen gas, which can ultimately diffuse into the steel matrix and contribute to HIC. Understanding their galvanic corrosion susceptibility, specifically the ability to serve as cathodes in the Fe-NbC and Fe-NbN galvanic couples, will aid in the development of more corrosion-resistant X70 grade steel.

However, caution should be taken in the interpretation of scanning Kelvin probe force microscopy (SKPFM) measurements, as it has been demonstrated by several research groups that the measured Volta potential difference acquired by this technique cannot always be correlated to the corrosion potentials of the coupled materials [154, 159, 160]. For instance, the work of Rohwerder clearly demonstrates that the Volta potential difference of Fe and Nb measured in air cannot predict the corrosion behavior or anodic/cathodic roles in the Fe-Nb galvanic couple [159]. After galvanic coupling Fe and Nb at different pH values, their Volta potential measurements supported that Nb was the net anode of the pair; however, the opposite was valid. Thus, when compared to SKPFM, potentiodynamic polarization is the more reliable technique for determination of corrosion potential values and anodic/cathodic roles of various inclusions.

3. EXPERIMENTAL PROCEDURES

3.1. HYDROGEN-TRAPPING CAPACITY OF FINE-SCALE NIOBIUM CARBONITRIDE PRECIPITATES

3.1.1. MATERIALS

The material selected for this project was a Nb model steel provided by CanmetMATERIALS. Cambridge Materials Testing Limited provided a report on the steel chemical composition, for which the following standards were employed: ASTM E1019-18: Standard Test Methods for Determination of Carbon, Sulfur, Nitrogen, and Oxygen in Steel, Iron, Nickel, and Cobalt Alloys by Various Combustion and Inert Gas Fusion Techniques [161], ASTM E1097-12: Standard Guide for Determination of Various Elements by Direct Current Plasma Atomic Emission Spectrometry [162], and ASTM E1479-16: Standard Practice for Describing and Specifying Inductively Coupled Plasma Atomic Emission Spectrometers [163]. The steel chemistry is summarized in Table 3-1.

Table 3-1: Nb Model Steel Chemistry (wt. %)

Element	C	Si	Mn	Al	Nb	V	Ti	P	S	O	N
wt. %	0.045	0.03	1.26	0.01	0.046	<0.01	<0.01	<0.010	<0.005	0.0015	0.0036

Heat treatments were applied to the as-received Nb model steel to vary the Nb precipitate size distribution. To remove the mill scale prior to heat treatment, 1 cm x 1 cm x 10 cm steel bars were flash pickled. The composition of the pickling solution was 477 mL of concentrated HCl (Fisher Chemical™, 36.5-38 % w/w, specific gravity: 1.19), 645 mL of

deionized water, and 2 g of hexamethylene tetramine (Sigma-Aldrich®, F.W.: 140.19 g/mol). The steel was immersed in this solution for 5 minutes at 50 °C, rinsed for 1 minute in deionized water at 23 °C, and rinsed with ethanol (Fisher Chemical™, F.W.: 46.069 g/mol).

The precipitation time temperature (PTT) diagram in Figure 3-1 was consulted to guide temperature and time selection for the steel heat treatment procedure [164]. On this diagram, a red dashed line has been superimposed at 900 °C. P_s and P_f represent the precipitation start and finish times, respectively. The red circle superimposed on the dashed line indicates the target holding time at 900 °C. A 500 second holding time was selected with the objective of increasing the number of fine precipitates ideal for APT.

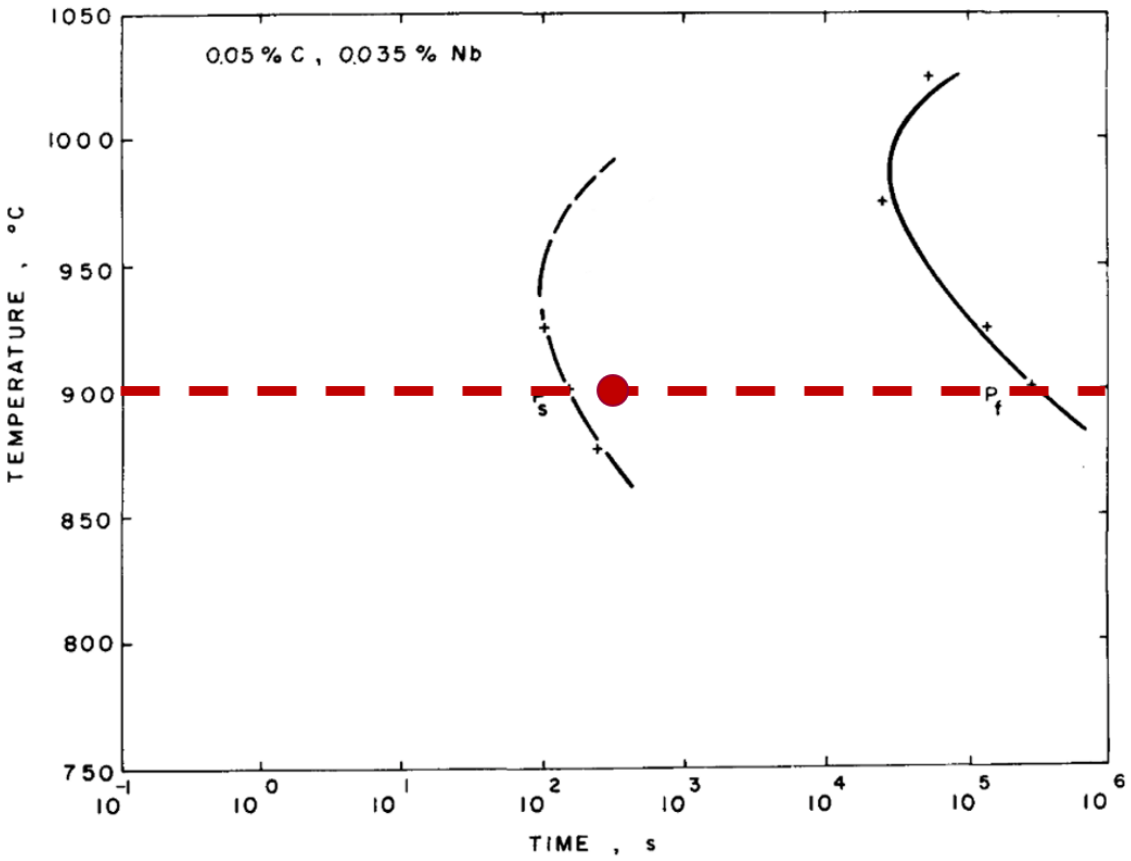

Figure 3-1: Precipitation Time Temperature Diagram for Nb-bearing Steel [164].

The flash pickled blocks of Nb model steel were held at 1100 °C for 1 hour in a Carbolite™ CTF Wire-Wound tube furnace under an Ar, 4.94 % H_2 (Air Liquide) atmosphere. The objective was to entirely solutionize the precipitates. This was followed by quenching the steel in water at room temperature. Next, the steel was placed back into the furnace and held at 900 °C for 500 s under the same atmosphere. This was followed by another quench in water at room temperature. Following heat treatment, all steel bars were flash pickled once more using the same procedure previously described. Additionally, to remove the decarburization layer off each bar, a reciprocating surface grinder was employed to grind approximately 100 µm off from each side of the specimens.

3.1.2. MICROSTRUCTURE CHARACTERIZATION

The as-received Nb model steel was cut using a Struers Secotom-50 precision cutter. Samples were cold mounted in MetLab Corporation epoxy resin and hardener. Grinding and polishing were carried out using the Struers Tegramin-25, polishing up to 1 µm using water-based lubricants. Once polished, all samples were etched using a 2 % nital solution to expose the steel microstructure. This is 2 % v/v nitric acid (Fisher Chemical™, F.W.: 63.01 g/mol, specific gravity: 1.42) in 2-propanol Optima® (Fisher Chemical™, F.W.: 60.1 g/mol). The process was repeated for the heat treated steel. Light optical microscopy (LOM) images were taken using a KEYENCE™ VHX Digital Multiscan Microscopy (VH-ZST) with the objective of comparing the average grain size in the as-received steel versus the heat treated steel. The grain size measurements were completed using ImageJ™, following ASTM E112-13: Standard Methods for Determining Average Grain Size, specifically, the Abrams Three-

Circle procedure [165]. Two planes were selected: rolling direction-normal direction (RD-ND) and rolling direction-transverse direction (RD-TD).

3.1.3. TRANSMISSION ELECTRON MICROSCOPY OF CARBON EXTRACTION REPLICAS

Carbon extraction replicas of one as-received sample, and four of the heat treated samples were prepared for TEM (transmission electron microscopy) investigation of the Nb-based precipitates. The specimens were polished up to 1 μm using water-based lubricants, and lightly etched in 2 % nital solution to expose the second phase or particles. Next, the freshly etched surface was coated with approximately 20 nm of carbon. Following this, the carbon replica film and extracted particles were removed from the steel surface. A sharp needle was used to draw a 2 mm x 2 mm square grid on the replicated surface film, and the carbon replica was stripped by etching in 4 % nital solution. Next, a glass straw was used to transfer the replica into deionized water, using several drops of methanol to flatten the replica film. Individual replica squares were lifted out onto a copper grid held by tweezers. The copper grid containing the replicas were examined using the Talos™ L120C TEM to characterize the precipitate size distributions and morphologies.

Images were taken at several magnifications to examine fine and coarse precipitates in each of the five carbon extraction replica samples. Magnifications of 92,000X or 120,000X were used to observe fine particles (< 15 nm diameter), and 28,000X was used to observe medium/coarse particles (> 15 nm diameter) in the heat treated sample. For the as-received specimen, magnifications of 45,000X and 8,500X were applied for fine and coarse particles, respectively. The acquired TEM images were opened into ImageJ™ software, which was

used to measure the particle diameters. Due to the difference in length and width for elongated precipitate morphologies, the shortest scale of precipitate projection was used as the width of the precipitate for simplification. This is clarified in the TEM micrograph shown as Figure 3-2. The precipitate size distributions in the as-received and heat treated samples were compared.

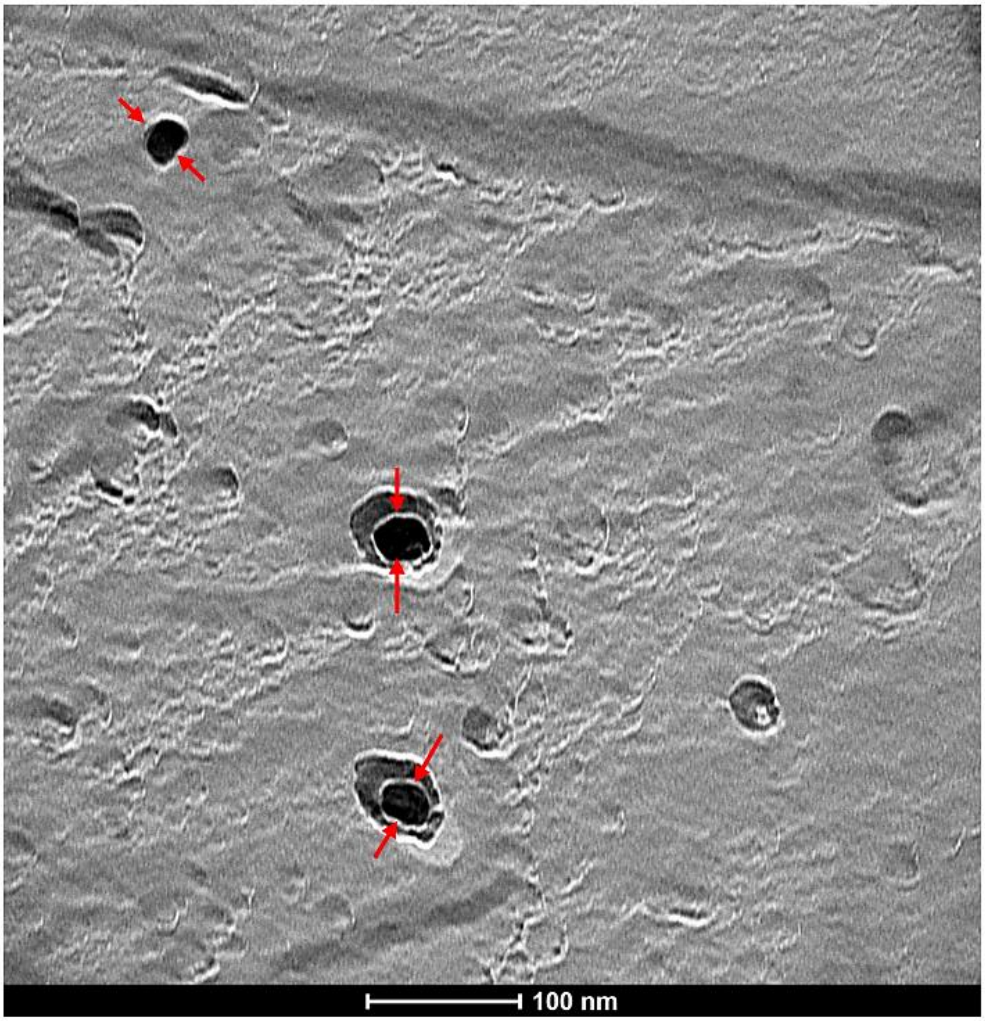

Figure 3-2: Defining precipitate width in ImageJ™.

To determine the precipitate chemistries present, spot-checking of the particles was conducted using electron energy loss spectroscopy (EELS). Fast Fourier Transforms (FFTs)

of TEM images were also completed. ImageJ™ and the FIJI image processing package were used to measure the d-spacings associated with the FFT-generated patterns to identify particle chemistry. This method is demonstrated in Figure 3-3. First, the TEM image of a precipitate was opened in ImageJ™. Next, a region of interest, capturing an entire precipitate, was selected and a FFT was performed. Using the FFT-generated image, the "calculate d-spacing" function was selected for each diffraction ring. The d-spacings measured by the software were compared to literature values. The two techniques were carried out to provide complementary compositional information.

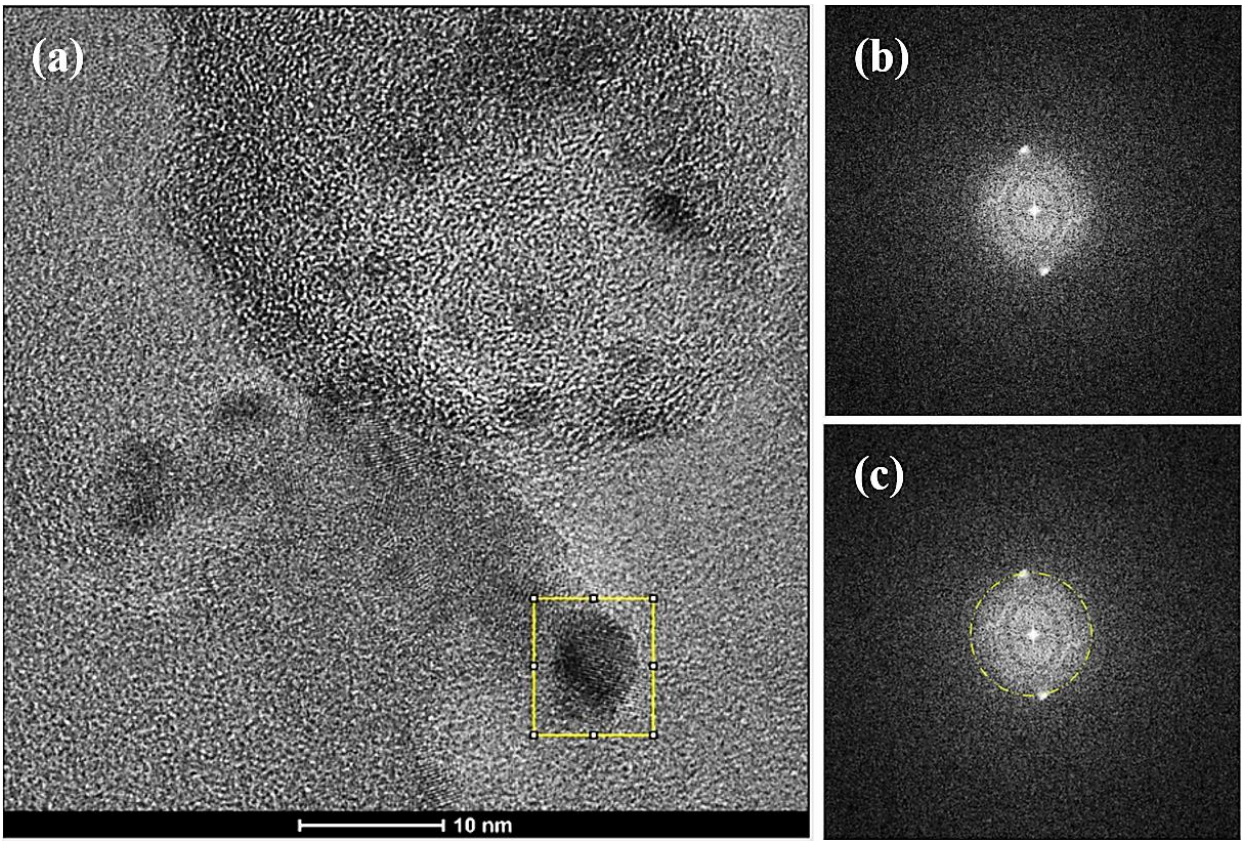

Figure 3-3: FIJI-ImageJ™ d-spacing measurement. (a) Bright-field TEM image of a precipitate cluster in the heat treated Nb model steel. A region of interest is highlighted by the yellow box. (b) FFT-generated image. (c) Selected ring for d-spacing calculation.

3.1.4. ATOM PROBE TOMOGRAPHY

Preparing samples for APT can be done by electropolishing, or through the combination of electropolishing and milling with a plasma focused ion beam (PFIB). Four matchsticks were cut from the as-received material using a Struers Secotom-50 precision cutter. The dimensions achieved were 0.5 x 0.5 x 20.0 mm^3. Following this, matchsticks were selected for two-stage electropolishing. Relatively long matchsticks were preferred so that samples can be repolished and used for multiple APT experiments. The first electropolishing stage, also known as the rough stage, involved repeatedly submerging a matchstick into 25% v/v perchloric acid (Fisher Chemical™, F.W.: 100.454 g/mol) in glacial acetic acid (Fisher Chemical™, F.W.: 60.052 g/mol). In the second stage, or fine stage, the tapered sample was contained in a Cu tube and electropolished under an optical microscope using a single droplet of 2 % perchloric acid in 2-butoxyethanol. A DC voltage range of 15-20 V was applied using a Xantrex LXQ 60-1 DC power supply during both stages of electropolishing. All electropolishing was conducted at room temperature. This sample preparation process is schematically represented in Figure 3-4.

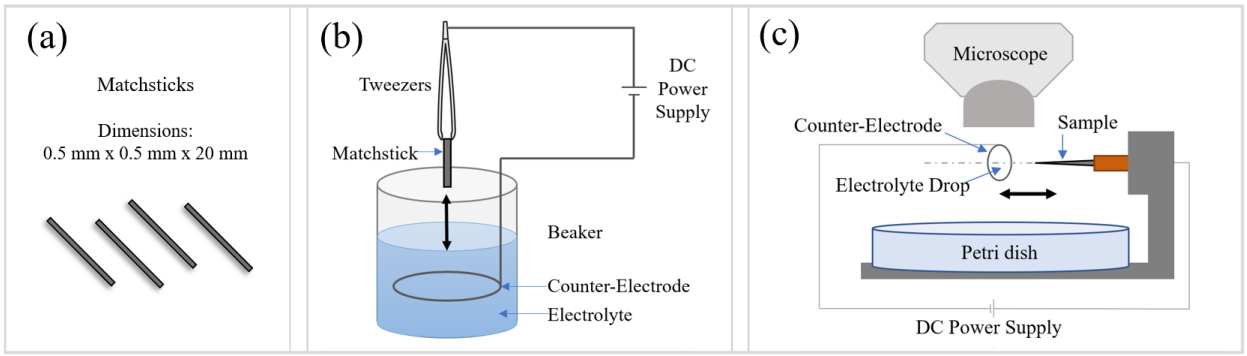

Figure 3-4: APT sample preparation process. (a) Cutting matchsticks, (b) rough-stage electropolish, and (c) fine-stage electropolish.

Additionally, three of the four electropolishing samples were milled further using a Thermo Scientific™ Helios G4 UXe DualBeam Plasma-FIB with the goal of maximizing the APT evaporated ion yield for this material. All APT results were obtained using the CAMECA LEAP 4000X HR operating in voltage mode with pulse rate of 200 kHz and detection rate of 0.5 %. All data reconstruction and analysis was conducted using Integrated Visualization and Analysis Software (IVAS®) version 3.8.0. This process was repeated on the matchsticks sectioned from the heat treated steel. The ion yields achieved via the two sample preparation strategies were compared for the as-received and heat treated Nb model steels, and summarized in Table 3-2. It is clear the two-stage electropolishing led to substantially higher ion yields when compared to yields retrieved from specimens that were electropolished and milled further with the PFIB.

Table 3-2: APT ion yields from sample preparation procedures

Sample	*Ion yield* (10^6)			
	Electropolishing	*Electropolishing + PFIB*		
	Trial 1	Trial 1	Trial 2	Trial 3
As-received	39.2	16.0	12.4	6.7
Heat treated	21.6	5.0	3.6	7.1

The effect of ion yield on the quality of the APT reconstruction is elucidated in Figure 3-5(a-b). Figure 3-5(a) displays the reconstruction from the electropolished matchstick prepared from the as-received Nb model steel. The carbon, iron, and niobium maps are shown. The sample volume is approximately 90 nm x 80 nm x 200 nm, with a total ion count of 39.2 million. Figure 3-5(b) shows a reconstruction from an electropolished and PFIB-milled matchstick, also prepared from the as-received Nb model steel. The sample

volume is approximately 80 nm x 70 nm x 160 nm, and the total ion yield is 16.0 million, the highest ion yield of the three electropolishing and PFIB-milling trials conducted.

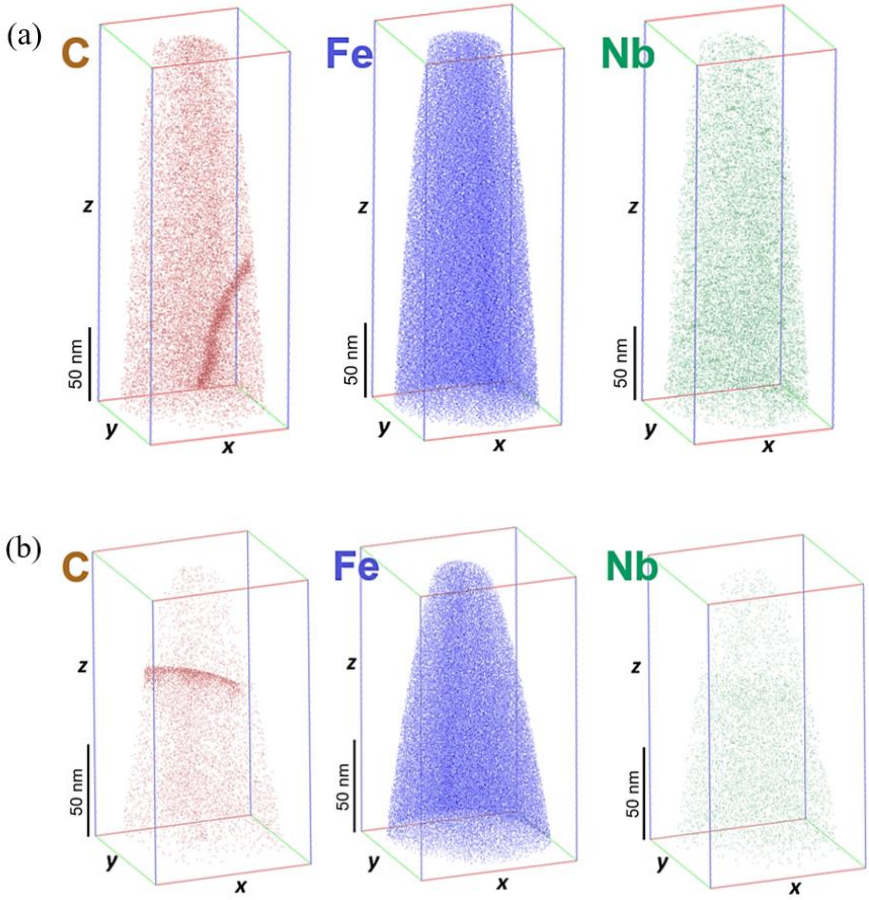

Figure 3-5: APT-reconstructed elemental maps from the (a) electropolished APT Nb model steel matchstick and (b) electropolished and PFIB-milled Nb model steel matchstick.

Additionally, the chemical composition of each of these reconstructions is tabulated in Table 3-3. Comparing Figure 3-5(a) and (b) it can be easily noticed that the lower yield obtained from electropolishing and PFIB-milling led to a less accurate representation of the analyzed specimen. When working with the heat treated steel, the objective is the visualize nanoscale niobium carbide precipitates, and eventually their associated

hydrogen-trapping locations. It is critical to optimize the sample preparation such that the highest possible ion yields are achieved moving forward. Thus, the two-stage electropolishing sample preparation route was used for all subsequent APT work.

Table 3-3: APT ion yields from select trials

	Ion count	
Element	*Electropolishing*	*Electropolish + PFIB*
Fe	31,250,697	12,317,637
Mn	440,849	149,556
Cr	128,363	34,456
Si	39,506	9,595
C	23,552	8,552
Nb	10,784	4,908
Al	9,247	3,460
N	4,031	3,108
P	1,821	493
Cu	1,059	1,045
B	85	0

3.1.5. H-CHARGING DEVICE FABRICATION AND CHARGING PARAMETER SELECTION

In preparation for hydrogen charging and subsequent APT characterization of the Nb-containing precipitates, an electrolytic charging device was designed and fabricated. The cell features a 1200 mL GAMRY Standard Multiport Corrosion Cell bottom with a custom lid composed of 304 stainless steel, which sits on top a polytetrafluoroethylene (PTFE) encapsulated silicone O-ring. A GAMRY Multiport™/Flexcell™ CPT Clamp, 4” Shot Flange was used to clamp the lid in place. The cell is to be deaerated the cell with nitrogen gas. A power supply is to be utilized to provide a constant current density for the hydrogen evolution reaction (HER) to occur, platinum wire is the counter electrode, and the working

electrode is the Nb model steel prepared by two-stage electropolishing of matchsticks. The steel tips are to be secured to a copper sample holder designed for the CAMECA LEAP 4000X HR system, which can be connected to a transfer rod post-charging and loaded to the atom probe for characterization of the charged samples.

A schematic representation of the charging device is shown as Figure 3-6. The electrolyte used in the cell will depend on the type of APT experiment. For the null-charge or hydrogen-charge experiment, the electrolyte will be 0.1 M NaOH in deionized H_2O, whereas for the deuterium-charge experiment, the electrolyte will be 0.1 M NaOD in D_2O. Recall charging with deuterium is advantageous for this research work due to its very low isotopic abundance compared to protium.

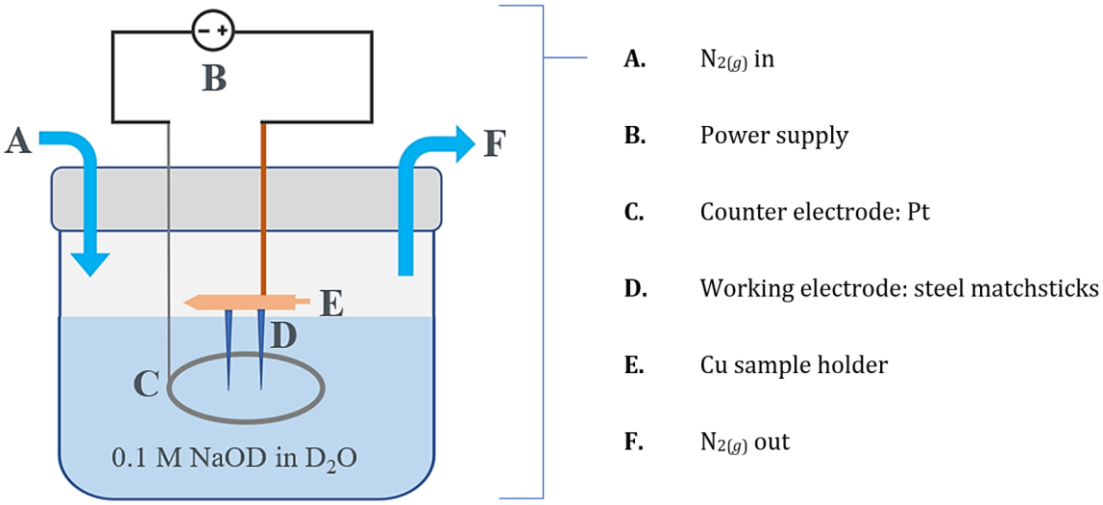

Figure 3-6: Schematic of electrolytic H-charging cell.

To determine the appropriate H-charging parameters, specifically, a suitable current density for hydrogen evolution, a 1-hour galvanostatic polarization in 0.1 M NaOH (Fisher Chemical™, F.W.: 39.997 g/mol) in deionized H_2O was conducted on the heat treated Nb

model steel. A current density of – 10 mA/cm^2 was applied using a GAMRY Instruments Reference 600+™ potentiostat/galvanostat/ZRA system. A 1 x 1 x 12 mm^3 steel matchstick served as the working electrode, two graphite rods were used as the counter electrode, a saturated calomel electrode was used as a reference, and the solution was deoxygenated using nitrogen gas (Air Liquide, purity: 99.999 %) for 1 hour prior to measurement. Deaeration with nitrogen gas continued throughout the polarization. The pH of the solution was measured before and after the polarization using a Cole-Parmer Accumet AB15 Basic pH benchtop meter. The stable potential of − 1.330 V_{SHE} (− 1.574 V_{SCE}) measured via galvanostatic polarization as well as measured electrolyte pH value of 12.66 were plotted on the Pourbaix diagram for iron [166] to confirm hydrogen evolution at a current density of – 10 mA/cm^2.

3.1.6. THERMAL DESORPTION SPECTROSCOPY: CHARGING DEVICE VALIDATION

TDS was carried out on the heat treated Nb model steel to measure hydrogen content in the material and validate the hydrogen charging ability of the electrolytic cell. The assembled cell is displayed in Figure 3-7. Prior to TDS measurement of the samples charged by the electrolytic device, 0.1 M NaOH (Fisher Chemical™, F.W.: 39.997 g/mol) in deionized water was prepared. The electrolytic cell was filled with solution such that the electrolyte only contacted the working electrode (three heat treated steel matchsticks of dimensions 0.5 mm x 0.5 mm x 20.0 mm), platinum wire counter electrode, nitrogen inlet, and nitrogen outlet. With the electrodes retracted, the solution was deoxygenated for 15 hours using nitrogen gas (Air Liquide, purity: 99.999 %) flowing at a rate of 100 mL/min.

This was done to minimize the oxygen gas current consumption during the hydrogen charging process. Next, the electrodes were lowered into the electrolyte. The potentiostat (Pharmacia Biotech Electrophoresis Power Supply 600) was connected and the matchsticks were charged for 1 hour using a constant current of – 5 mA, equivalent to constant current density of – 10 mA/cm^2 for the three samples. The charging process was conducted at room temperature.

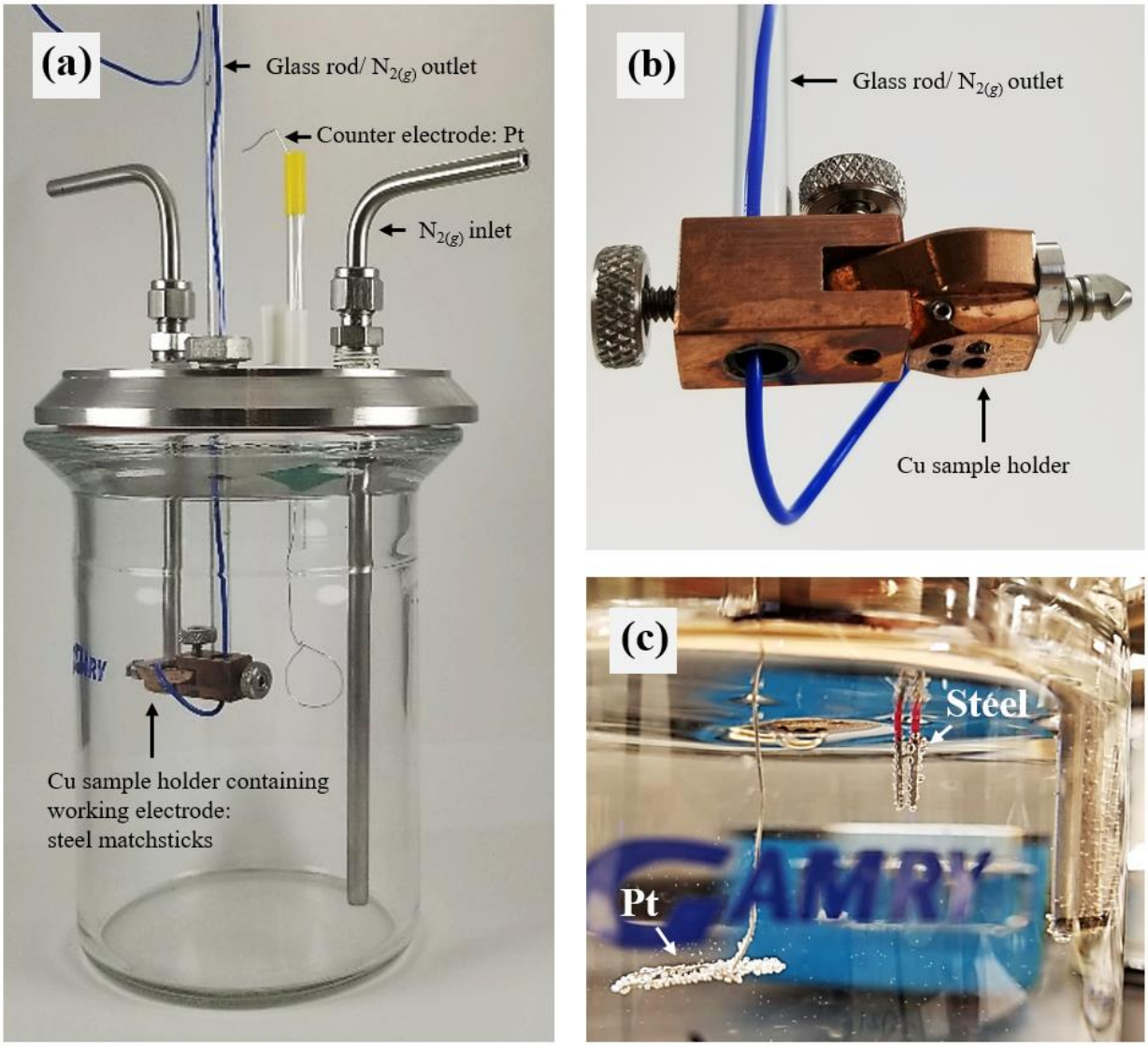

Figure 3-7 (a) Assembled H-charging device, (b) copper APT sample holder (without matchsticks) and $N_{2(g)}$ outlet, and (c) electrodes immersed in 0.1 M NaOH solution during charging.

A Hydrosteel® 6000 hydrogen probe (ION Science) was used for all TDS measurements. This solid-state sensor featured a proton-conducting ceramic plated on each side with palladium. It worked by absorbing hydrogen on one side, which was then oxidized at the palladium-ceramic interface by a voltage. Protons were absorbed into the ceramic, expelled out the other end and reduced to form hydrogen gas. The electrical current flow associated with the hydrogen redox process was measured by the probe. The thermal desorption apparatus also featured a quartz tube inside a tube furnace open at both ends. One end was connected to a nitrogen gas supply (Air Liquide, purity: 99.9999 %), which flowed through a mass flow controller (MKS, Type 247) to balance nitrogen flow through the apparatus. The draw rate of this pump is built into the hydrogen probe, connected to the other end of the quartz tube.

The nitrogen gas also flowed through an oxygen scavenger (SGE Analytical Science™) through stainless steel SWAGELOK™ fittings into the quartz tube. This decreased the oxygen content to 15 ppb. The tube had an outer diameter of 12 mm and necked down to 6.3 mm near its center such that hydrogen gas coming out of the sample was swept by the carrier gas into a narrower tube. This was done to minimize mixing with other gases so that TDS peaks are more clearly defined. A sheathed K-type thermocouple was inserted into the quartz tube, positioned next to the samples. The thermocouple was connected to the thermocouple data logger (Omega Engineering, OM-EL-USB,TC). A DuPont™ Tedlar® bag (gas-impermeable gas chromatography bag) was filled with 105 ppm (mole/mole) hydrogen in nitrogen, and was used to calibrate the hydrogen probe before each test.

To obtain hydrogen profiles, the electrolytically charged matchsticks were heated from room temperature to 950 °C at a rate of 20 °C/min with the nitrogen carrier gas flowing over the sample. After TDS, the probe was detached, and the pressure gauge was connected. This sealed the quartz tube and kept it pressurized as the furnace cooled, limiting oxidation of the specimens so that they can be weighed accurately. The TDS setup is summarized in Figure 3-8.

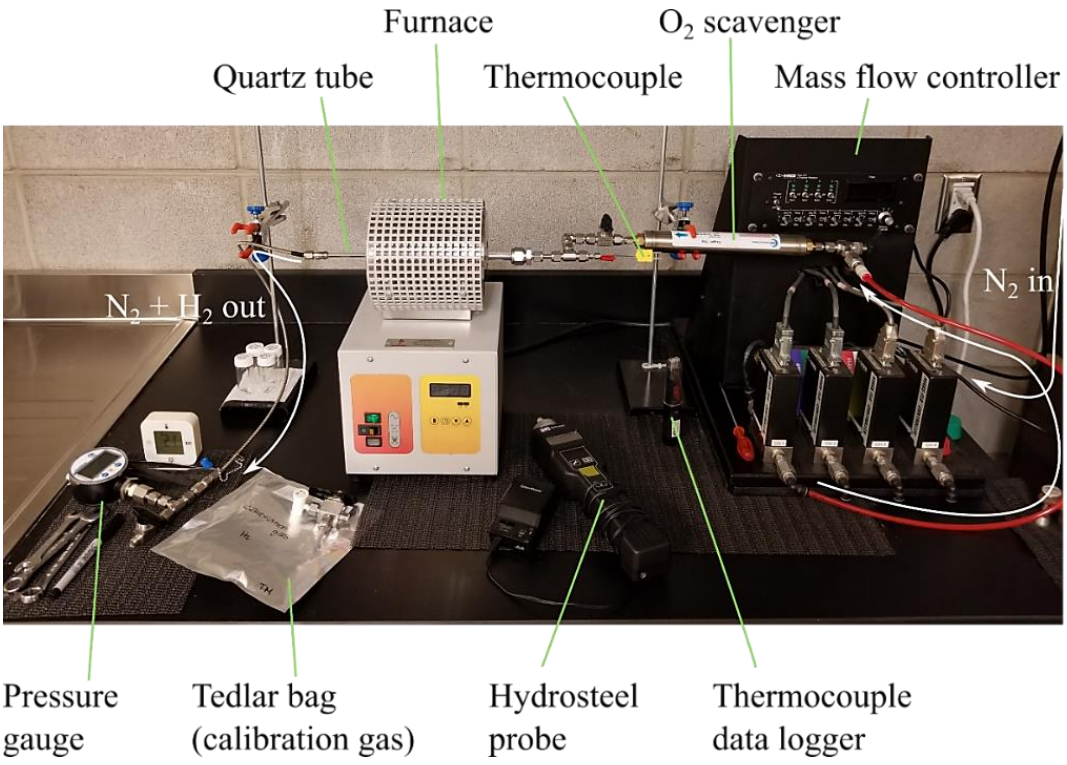

Figure 3-8: TDS apparatus at CanmetMATERIALS.

3.2. CORROSION EVALUATION OF NbC AND NbN INCLUSIONS WITHIN PURE IRON

3.2.1. MATERIALS

The materials used for this project include NbC and NbN model inclusion samples provided by Matsurf Technologies Inc. The specimens are hollow iron tubes with an NbC or NbN inclusion embedded. They were formed by vacuum hot pressing, and feature purities of 99.9% for Fe, NbC and NbN, as reported by the manufacturer. A schematic of the model inclusion samples is displayed in Figure 3-9. To compare the results acquired from the model inclusions to a commercial steel, a X70 grade steel was supplied by EVRAZ North America. The commercial steel chemistry is summarized in Table 3-4, as reported by the manufacturer.

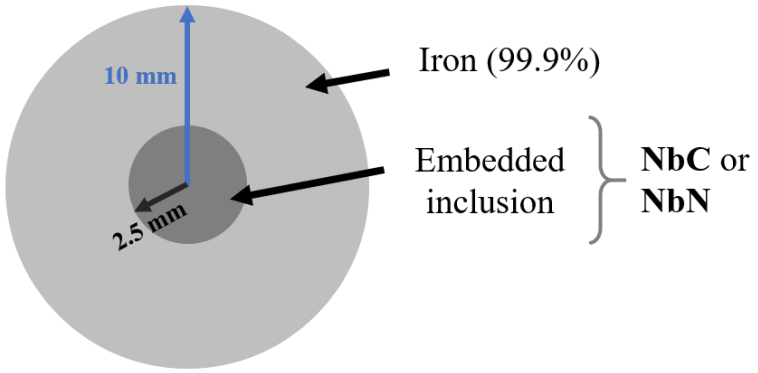

Figure 3-9: Schematic representation of radial surface of model precipitate.

Table 3-4: X70 Steel Chemistry (wt. %)

Element	C	Si	Mn	Al	Nb	Ti	S	N	Fe
wt. %	0.039	0.28	1.29	0.031	0.089	0.015	0.0027	0.0061	balance

3.2.2. MODEL INCLUSIONS

In preparation for microstructural characterization, an NbC and NbN model inclusion samples were each cold mounted in MetLab Corporation epoxy resin and hardener, with the radial surface serving as the working surface. The samples were ground and polished up to 1 μm using water-based lubricants. A continuity check was conducted using a digital multimeter to ensure electrical contact throughout the sample. Next, the samples were imaged using a JEOL JSM-6610LV scanning electron microscope coupled with X-ray energy dispersive spectroscopy. Using SEM, secondary electron and backscatter electron images were taken of three different regions of interest: the entire sample, iron-inclusion interface, and the inclusion. With EDS, elemental maps were captured along the iron-inclusion interface and inclusion using Oxford Instrument's AZtec software (version 3.3). An accelerating voltage of 15 kV was employed, and the working distance varied from 50 – 10 mm, depending on the region of interest. The magnification used to capture the images ranged from 11 – 500X.

After, the model iron-inclusion couples were repolished to 1 μm using water-based lubricants. To document the initial state of the specimens, each was imaged using a KEYENCE™ VHX Digital Multiscan Microscopy (VH-ZST). The specimens were then immersed in naturally aerated passivating and active solutions (125 mL) at room temperature. The chemical compositions of the electrolytes are summarized in Table 3-5. This passivating solution chemistry was selected as it is an alkaline saline solution known to spontaneously passivate steel [167], while the activating solution was chosen to simulate

a wet soil environment believed to cause near-neutral pH stress corrosion cracking of pipeline grade steel [168]. Images were taken using an iPhone 8 Plus 12MP Telephoto camera (Apple Inc.) over a 48-hour exposure to the passivating solution or active solutions, taken at the following times after immersion: 0, 3, 6, 9, 12, 24, 36, and 48 hours. LOM was used again to capture the state of the samples post-48-hour immersion. The working surface was descaled by submerging the model inclusions in an aqueous solution of 63 mL concentrated HCl (Fisher Chemical™, 36.5-38 % w/w, specific gravity: 1.19), 63 mL deionized water and 0.4375 g of hexamethylene tetramine (Sigma-Aldrich®, F.W.: 140.19 g/mol) for 10 minutes at room temperature, as suggested by ASTM G1-C.3.5 [169]. LOM images of the surface were taken to compare to previous sample conditions.

Table 3-5: Electrolyte compositions

Passivating solution				
Chemical compound	NaCl	Na_2CO_3	$NaHCO_3$	
Concentration (M)	0.010	0.005	0.010	
Active (NS_4) solution				
Chemical compound	KCl	$CaCl_2 .2\ H_2O$	$MgSO_4 .7\ H_2O$	$NaHCO_3$
Concentration (g/L)	0.122	0.093	0.131	0.483

In addition, optical surface profilometry (OSP) area scans were conducted before and after the 48-hour immersion in the active solution with the objective of characterizing the change in surface height. A Uniscan Model M370 Scanning Electrochemical Workstation equipped with a OSP Class II Laser Sensor Head (KEYENCE™ Corporation, λ = 650 nm, maximum output = 0.95 mW) was used for all OSP measurements. After calibration, the laser beam was used to raster through a sample area of 12,600 μm x 12,600 μm and provided the height change relative to a user-defined reference point. The scan

width and height step size were both set to 50 µm to yield 253 data points for each width and height line scan. For the movement and acquisition parameters, the scan velocity was set to 500 µm/s, over-scan was set to 100 µm, and sweep scan mode was selected. The OSP maps acquired were corrected as required using the tilt-correction function in the M370 software (version V4.61).

To determine the extent of galvanic corrosion between NbC and NbN and the iron matrix, a series of potentiodynamic polarizations (PDPs) were conducted on the scaled-up model particle-matrix samples. A second set of model inclusion specimens were prepared for electrochemical methods. A copper wire was attached to the back of each inclusion using conductive aluminum tape, and the sample was subsequently cold mounted in epoxy resin and hardener. Next, the sample surface was manually ground and polished up to 1200 grit SiC using water-based lubricants. For polarization measurements, the setup included a GAMRY Instruments Reference 600+™ potentiostat/galvanostat/ZRA system, Princeton Applied Research K47 corrosion cell, two graphite rods as the counter electrode, model inclusion sample as the working electrode, saturated calomel electrode as the reference electrode, gas bubbler, and nitrogen gas cylinder (Air Liquide, purity: 99.999 %). The apparatus is displayed in Figure 3-10. Clear lacquer was used to selectively expose the material of interest for each polarization measurement, and the sample area was measured using digital calipers and recorded. The electrolyte was deaerated using nitrogen gas for 1 hour prior to measurement. Next, a 1-hour open circuit potential measurement and PDP was completed in triplicate in the passivating and active electrolytes for pure iron, NbN, and NbC. Deaeration continued throughout the subsequent OCP and PDP measurements.

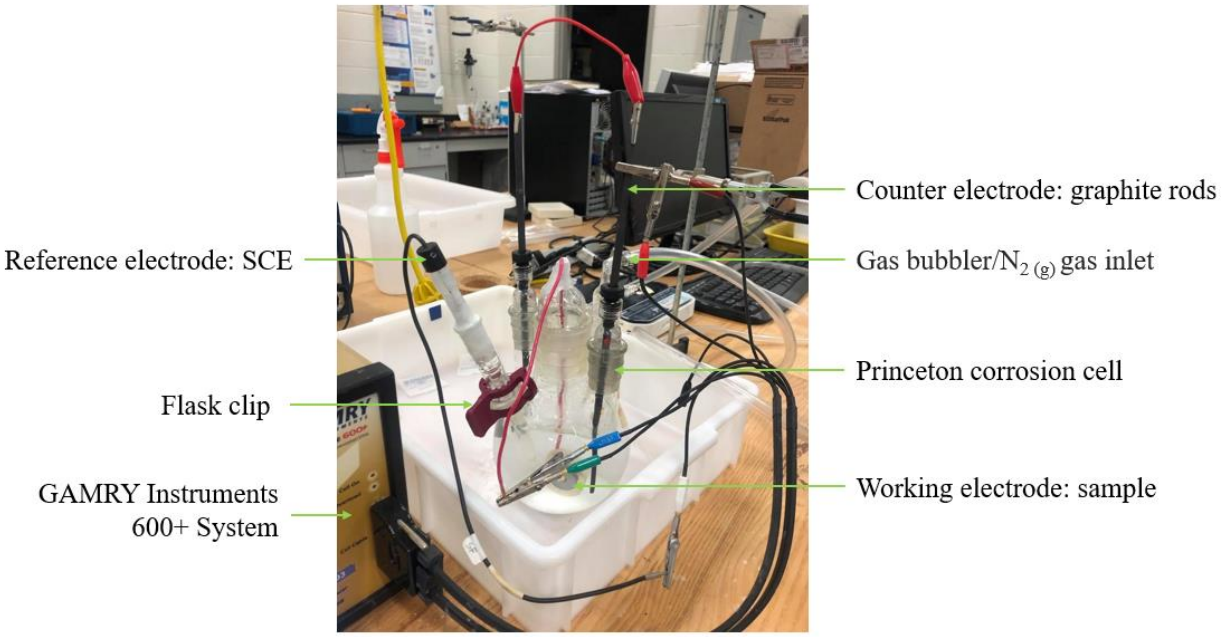

Figure 3-10: Polarization cell apparatus.

3.2.3. X70 STEEL

X70 steel was sectioned using a Struers Secotom-50 precision cutter. Copper wire was attached to the back of each X70 sample (dimensions 1.5 cm x 1.5 cm x 1.3 cm) using conductive aluminum tape. The specimen was then cold mounted in epoxy resin and hardener, and ground and polished up to 1200 grit SiC using water-based lubricants. The sample area was measured using digital calipers and recorded. Potentiodynamic polarizations were conducted on the X70 using the same setup and parameters as described in Section 3.2.2., and shown in Figure 3-10.

To determine the passive film chemistry associated with PDP curves acquired from the iron of the model inclusion samples and X70 steel, potentiostatic polarizations (PSPs) were conducted in triplicate at two different voltages: – 270 mV and – 480 mV. Each voltage

was held for three hours. The same experimental apparatus described in Section 3.2.2 was used. After the third PSP, the copper wire was manually ground off, LOM images of the surface were acquired, and the X70 samples were stored in a desiccator in preparation for surface characterization via X-ray photoelectron spectroscopy (XPS).

The XPS analyses were carried out with a Kratos Analytical Ltd AXIS Supra X-ray photoelectron spectrometer using a monochromatic Al K(alpha) source (15 mA, 15 kV). The instrument can detect all elements except hydrogen and helium, probes the surface of the sample to a depth of 7 - 10 nm, and has detection limits ranging from 0.1 - 0.5 at. %, depending on the element. The instrument work function was calibrated to give a binding energy (BE) of 83.96 eV for the Au 4f7/2 line for metallic gold and the spectrometer dispersion was adjusted to give a BE of 932.62 eV for the Cu 2p3/2 line of metallic copper. The Kratos Analytical charge neutralizer system was used on all specimens. Survey scan analyses were carried out with an analysis area of 300 μm x 700 μm and a pass energy of 160 eV. High resolution analyses were carried out with an analysis area of 300 μm x 700 μm and a pass energy of 20 eV. Spectra were charge-corrected to the main line of the carbon 1s spectrum (adventitious carbon) set to 284.8 eV, and the spectra were analyzed using CasaXPS software (version 2.3.14). Procedures from M. C. Biesinger *et al.* [170] and A. P. Grosvenor *et al.* [171] were followed for the Fe 2p spectra curve-fitting.

4. RESULTS AND DISCUSSION

4.1. HYDROGEN-TRAPPING CAPACITY OF FINE-SCALE Nb(C,N) PRECIPITATES

4.1.1. MICROSTRUCTURE CHARACTERIZATION

Light optical microscopy images (at 1000X) of the as-received and heat treated steel microstructures in the RD-ND and RD-TD planes are presented in Figure 4-1(a-d). Ferrite, bainite, and martensite were observed. The average grain size measured with 95 % confidence interval error were 5.1 ± 0.7 μm, 3.9 ± 0.9 μm, 7.0 ± 0.8 μm, and 6.7 ± 1.7 μm in (a), (b), (c), and (d), respectively. The measurements indicate that the heat treatment resulted in an increase in the average grain size, which was expected.

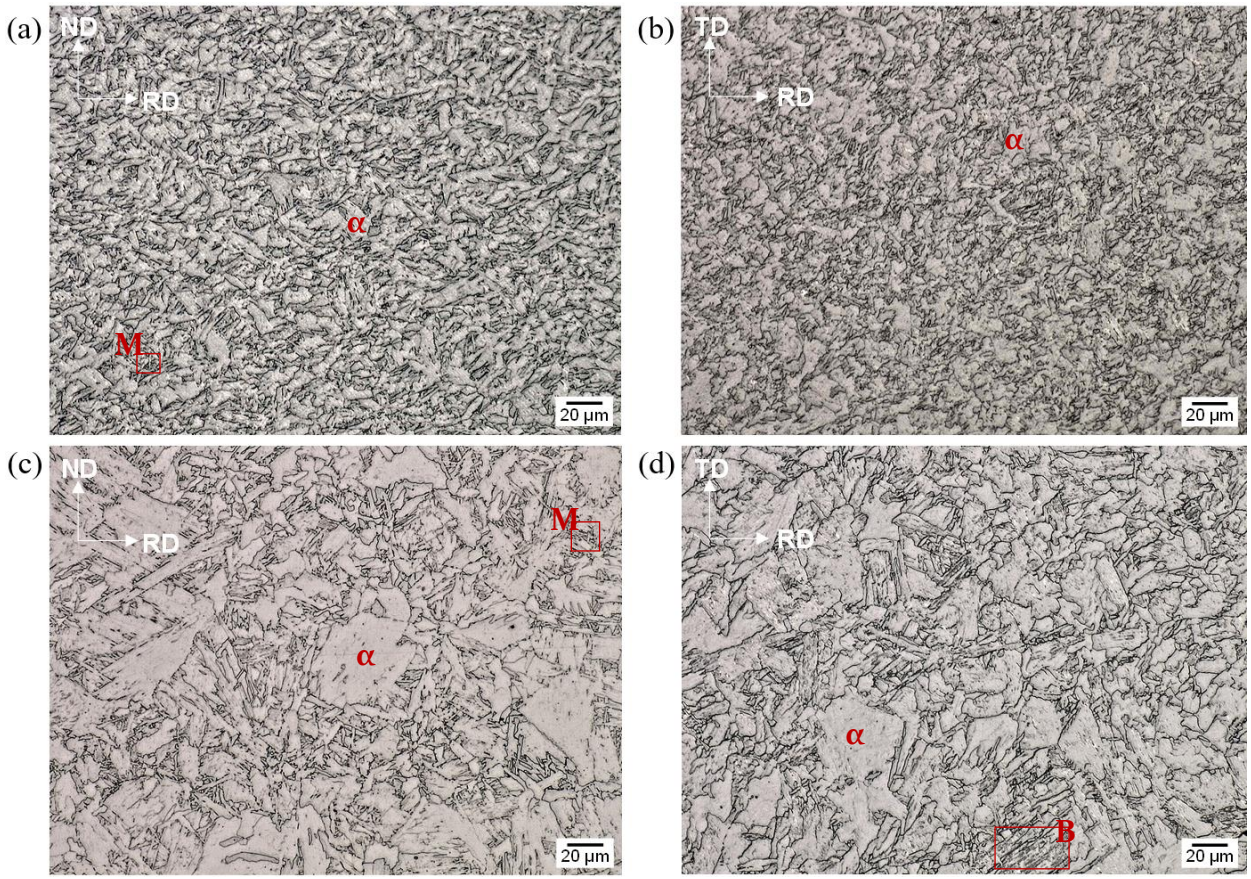

Figure 4-1: (a) As-received steel microstructure RD-ND plane, (b) RD-TD plane, (c) heat treated steel microstructure RD-ND plane, and (d) RD-TD plane. Ferrite, bainite and martensite are labelled.

4.1.2. TEM OF CARBON EXTRACTION REPLICAS

4.1.2.1. *Precipitate Morphologies and Size Distribution*

Preparation of carbon extraction replica samples allows for observation of various precipitates via TEM without the information being convoluted by the steel matrix. Recall four trials of the heat treatment (described in Chapter 3) were conducted on the as-received steel. One carbon extraction replica sample was prepared from the as-received steel, whereas four samples were prepared from the heat treated steel bars obtained from the four trials. Micrographs from one trial of the heat treated steels are shown as a typical example of the precipitate morphologies present.

Coarse precipitates (> 15 nm precipitate width) were observed in all samples prepared from the as-received and heat treated steels, as shown by the collection of TEM images in Figures 4-2 and 4-3. Elongated coarse precipitates distributed at grain boundaries were evident in the as-received steel, shown in Figure 4-2. Also, coarse precipitates with relatively low width were also found distributed at grain boundaries in the heat treated steel, as presented in Figure 4-3. Fine precipitates (< 15 nm precipitate width) were also identified in all carbon extraction replica samples. Typical TEM images of the fine precipitates in the as-received and heat treated are displayed in Figures 4-4 and 4-5, respectively. Precipitation of fine particles along grain boundaries was evident. The morphology of the fine precipitates observed in all samples were mostly square, quasi-square, rectangular, or round shape. Very few elongated rod-shape particles were detected.

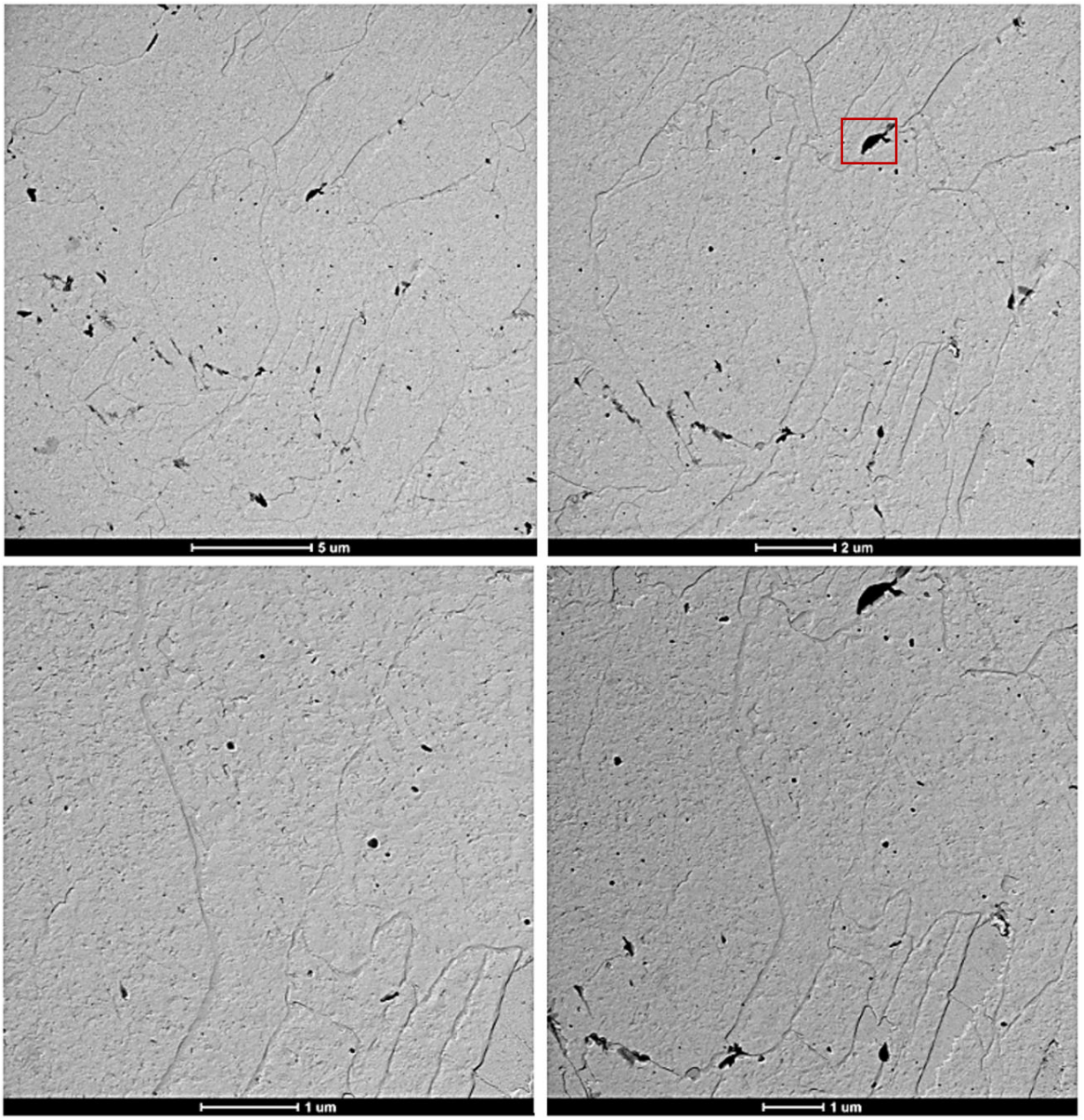

Figure 4-2: Bright field TEM images of coarse particles at different magnifications in as-received steel. An example of a course precipitate is highlighted by the red box.

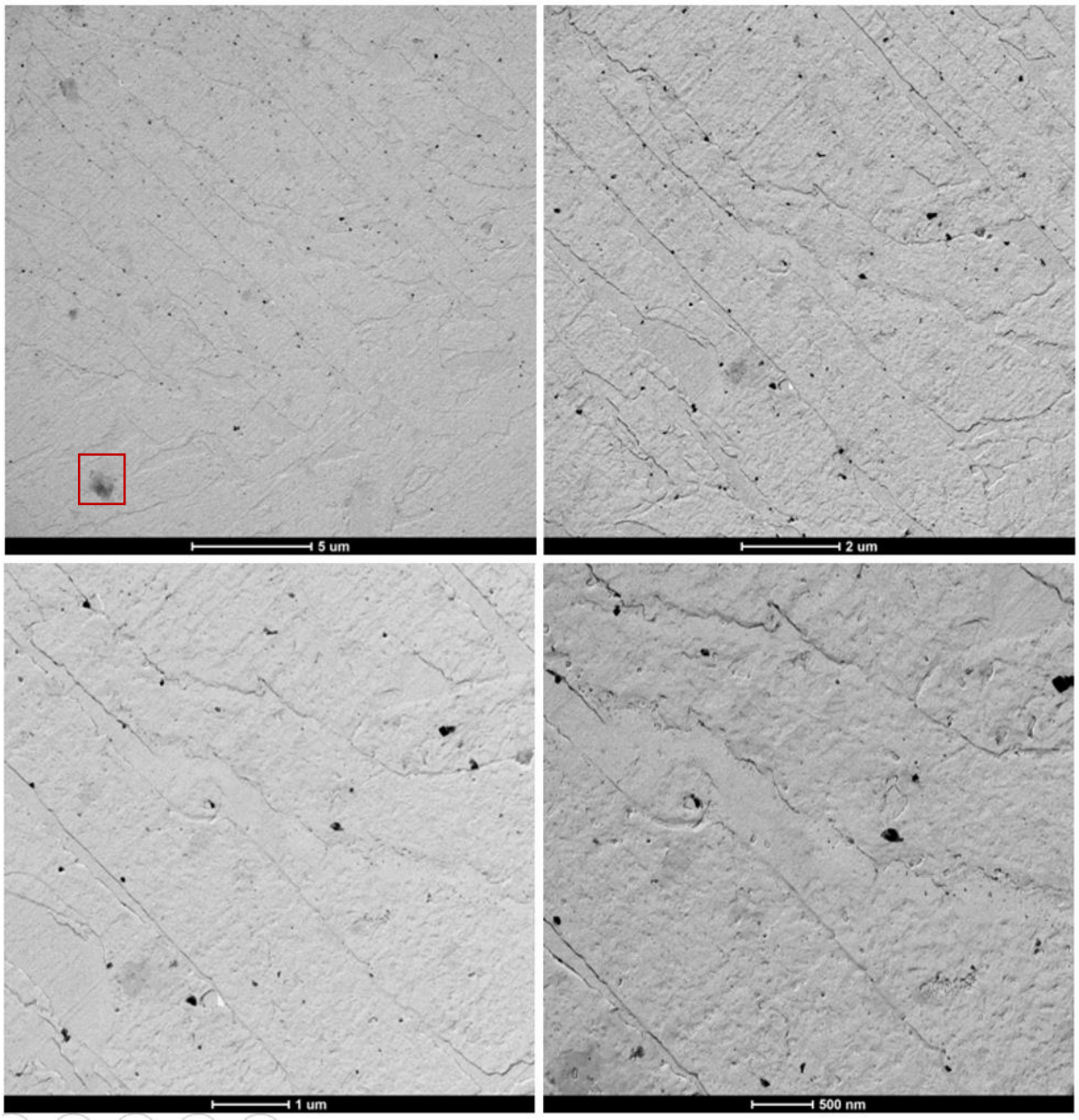

Figure 4-3: Bright field TEM images of coarse particles in heat treated steel.
An example of a course precipitate is highlighted by the red box.

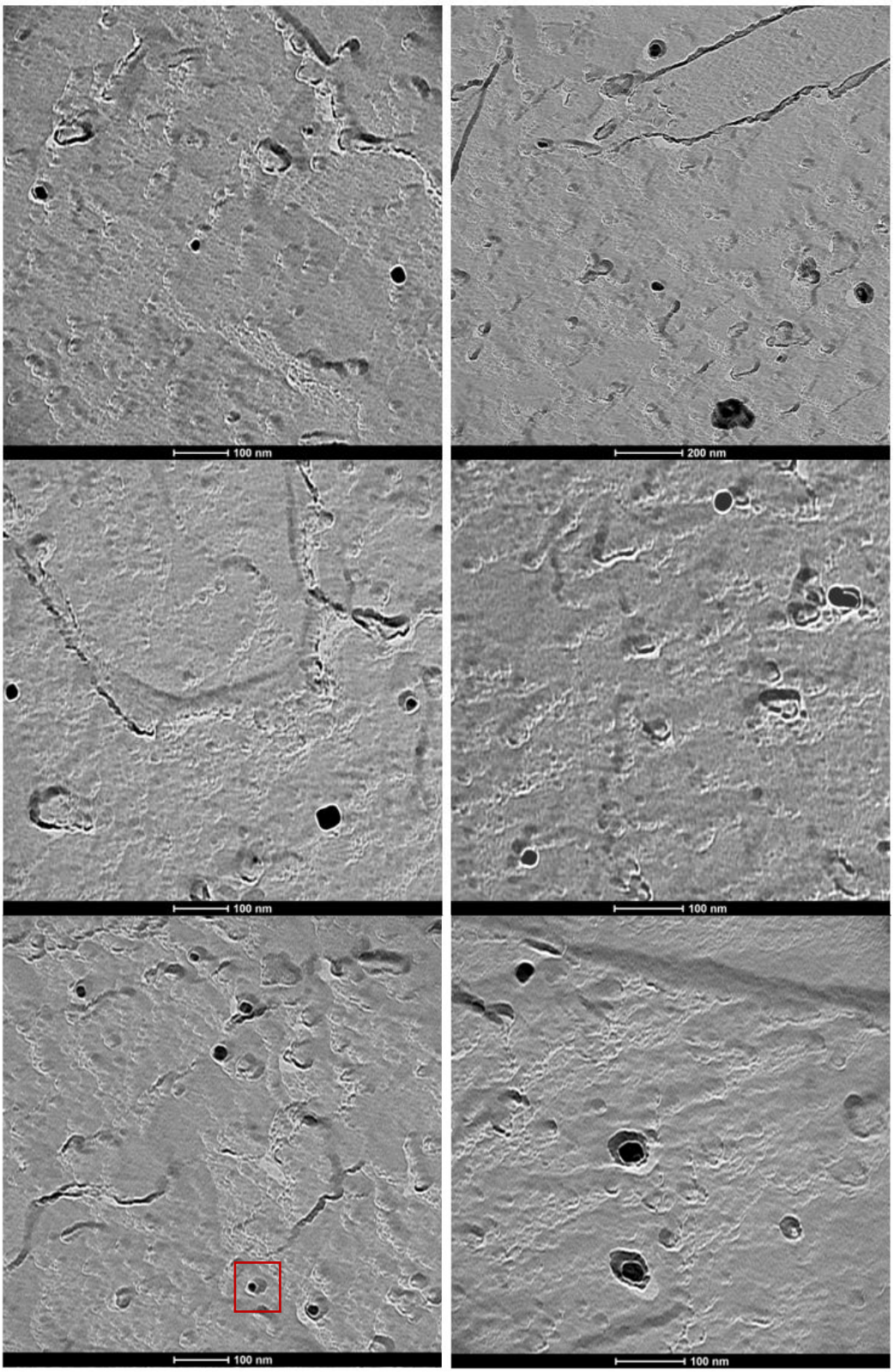

Figure 4-4: Bright field TEM images of fine particles in as-received steel. An example of a fine precipitate is highlighted by the red box.

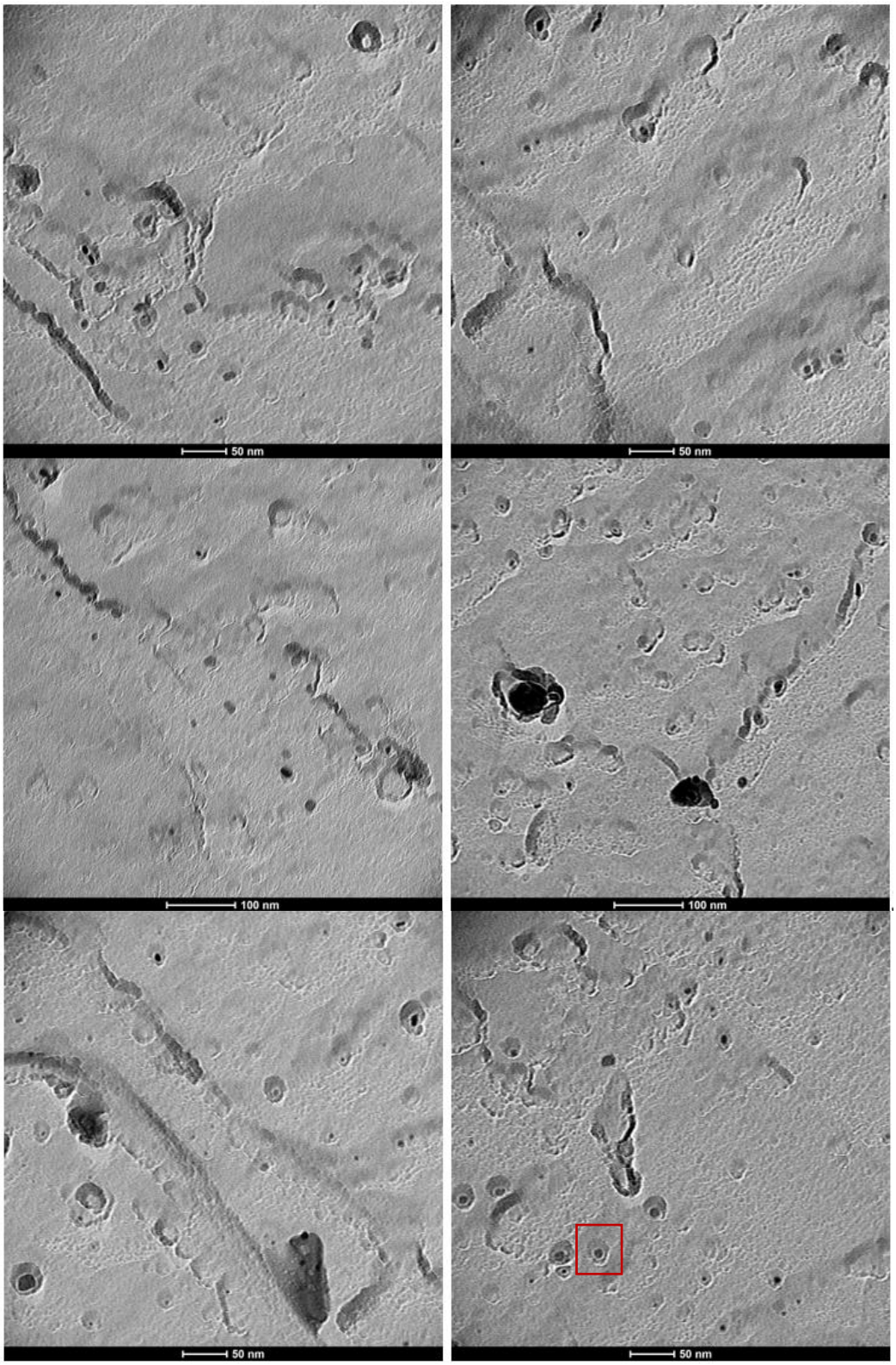

Figure 4-5: Bright field TEM images of fine particles in heat treated steel. An example of a fine precipitate is highlighted by the red box.

Quantitative TEM analysis was conducted for each sample to obtain measurements of precipitate width and compare the as-received precipitate size distribution to that of the four heat treated trials. Table 4-1 summarizes the precipitate size measurements obtained from the TEM images. The reported width depended on precipitate morphology. To clarify, precipitate width was reported as either the length of the square, small side of rectangular particles, or diameter of round-shaped particle. The average fine and coarse precipitate widths with corresponding 95% confidence interval error values are presented after measurements from 418 precipitates in the as-received carbon extraction replica sample, and 2573 precipitates from the combination of all four heat treated samples.

Table 4-1: Precipitate size distributions in as-received and heat treated steels

Sample	***Fine***		***Coarse***	
	Sample size	*Average precipitate width (nm)*	*Sample size*	*Average precipitate width (nm)*
As-received	102	10.8 ± 0.6	316	38.6 ± 2.9
Heat treated	2004	5.5 ± 0.2	569	27.3 ± 1.3

Based on these measurements, it is clear that the heat treatment procedure altered the precipitate size distribution present in the Nb model steel. Specifically, the as-received steel contains a relatively high number of coarse precipitates, whereas the heat treated steels contain a relatively high number of fine precipitates. There was no significant statistical difference between the four heat treated samples. Frequency distributions of the precipitate width in the as-received and heat treated steels are presented as Figures 4-6 and 4-7, respectively. Majority of the precipitates (63%) in the heat treated steel samples were $\leq$ 10 nm in width, and 24% were $>$ 10 nm but $\leq$ 20 nm in width.

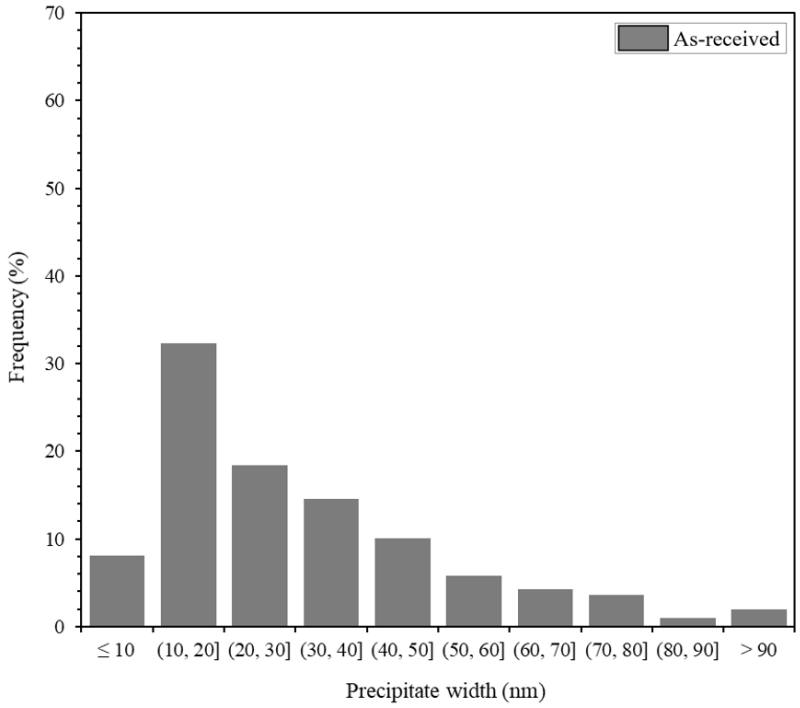

Figure 4-6: Precipitate size distribution in as-received Nb model steel.

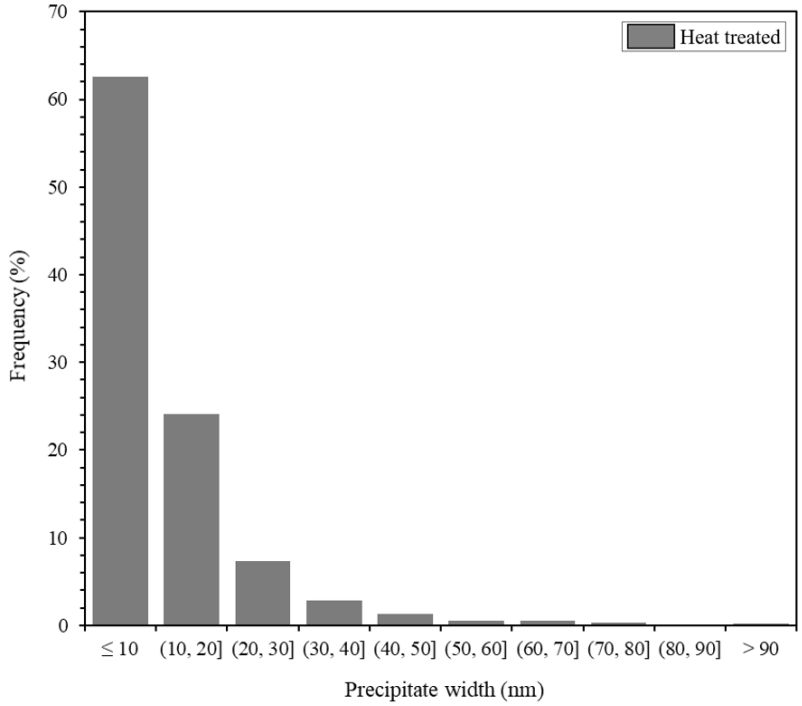

Figure 4-7: Precipitate size distribution in heat treated Nb model steel.

4.1.2.2. *Electron Energy Loss Spectroscopy*

Three different sites in the heat treated steel were analyzed using EELS to spot-check the precipitate chemistries present. The results from this technique are presented in Figures 4-8 – 4.10. Figure 4.8 presents an electron image and corresponding Nb and C EELS maps, suggesting the presence of several NbC precipitates in this region of interest. In Figure 4.9, another analyzed region is presented. A pair of NbC precipitates is present, as suggested by the Nb and C EELS maps corresponding to the electron image. There was no Ti or N detected in the regions of interest presented in Figure 4-8 and 4-9. Figure 4.10 presents an electron image of a relatively complex precipitate accompanied by Nb, C, Ti, and N EELS maps, suggesting the existence of NbC nucleating on a TiN precipitate. Precipitation of various phases in microalloyed steels is a sequential process, attributed to solubility differences, establishing guidelines for phase identification. Because TiN is the least soluble of precipitates in austenite, TiN is expected to precipitate at relatively high temperatures at earlier processing stages. Nb is known to feature higher solubility, and is thus expected to precipitate at lower temperatures during later processing stages [172]. Figure 4-11 provides a comparison of the equilibrium solubility products for microalloyed carbides and nitrides in austenite and ferrite [173]. For example, for NbC, $K_s = [Nb]_{eq}[C]_{eq} = 10^{[(A-B)/T]}$, where K_s is the solubility product, T is the temperature in Kelvin, and A and B are constant for a given system.

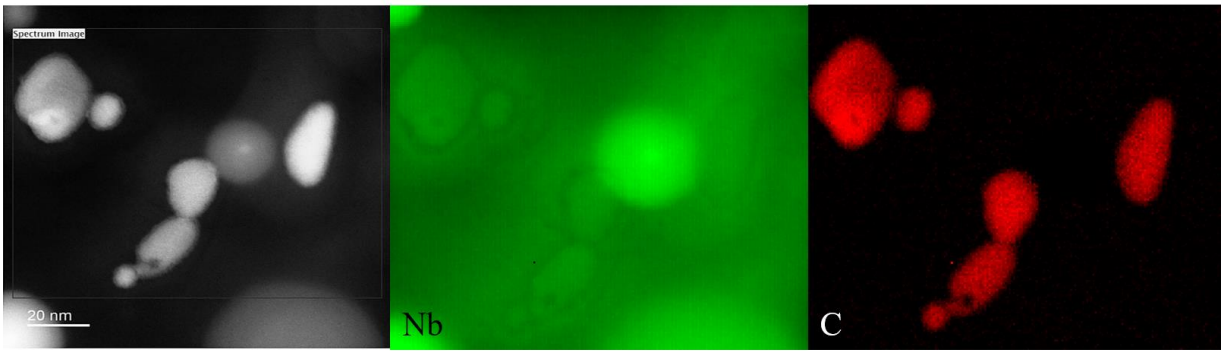

Figure 4-8: TEM image of precipitate accompanied by Nb and C EELS maps.

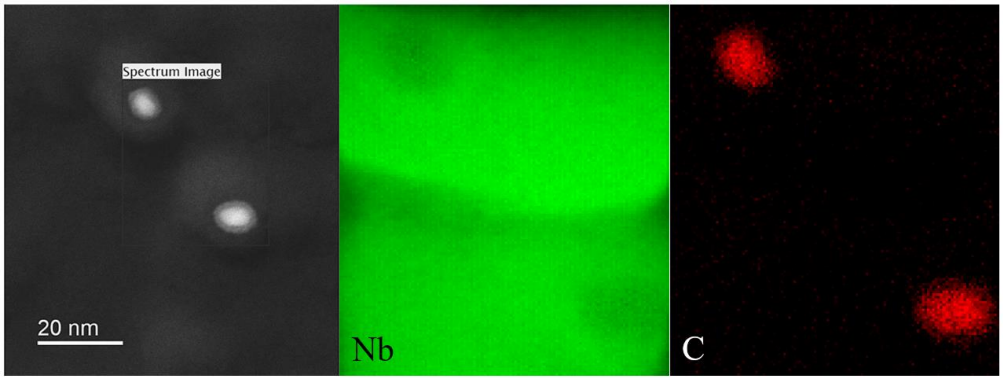

Figure 4-9: TEM image of precipitate accompanied by Nb and C EELS maps.

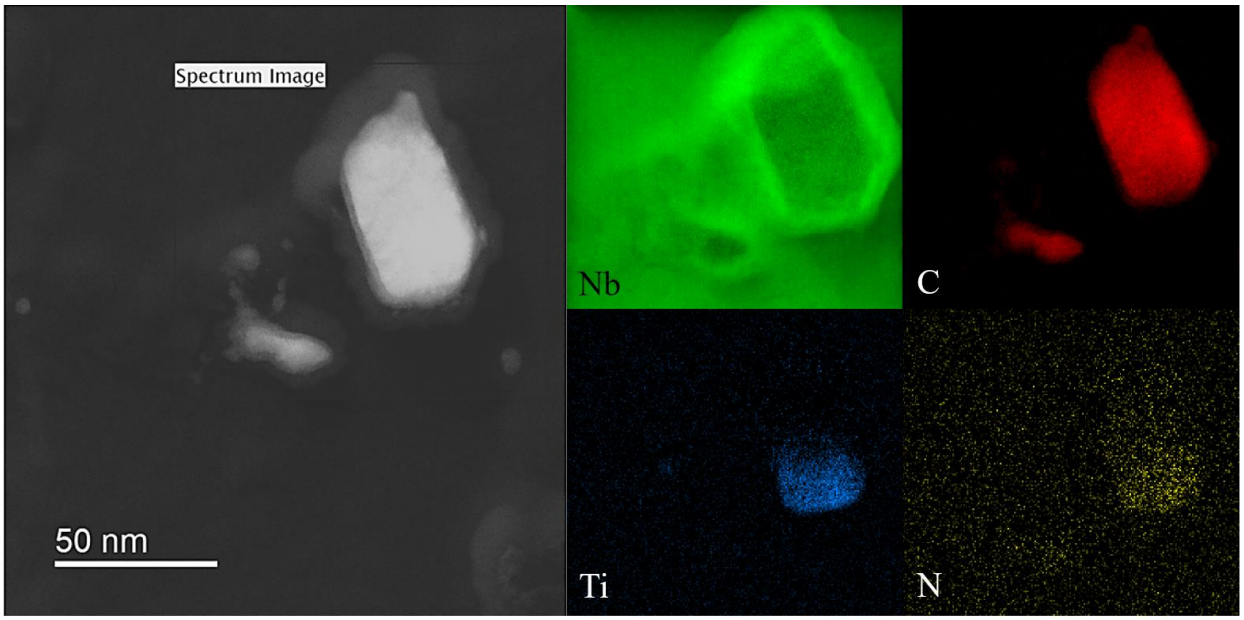

Figure 4-10: TEM image of precipitate accompanied by Nb, C, Ti, and N EELS maps.

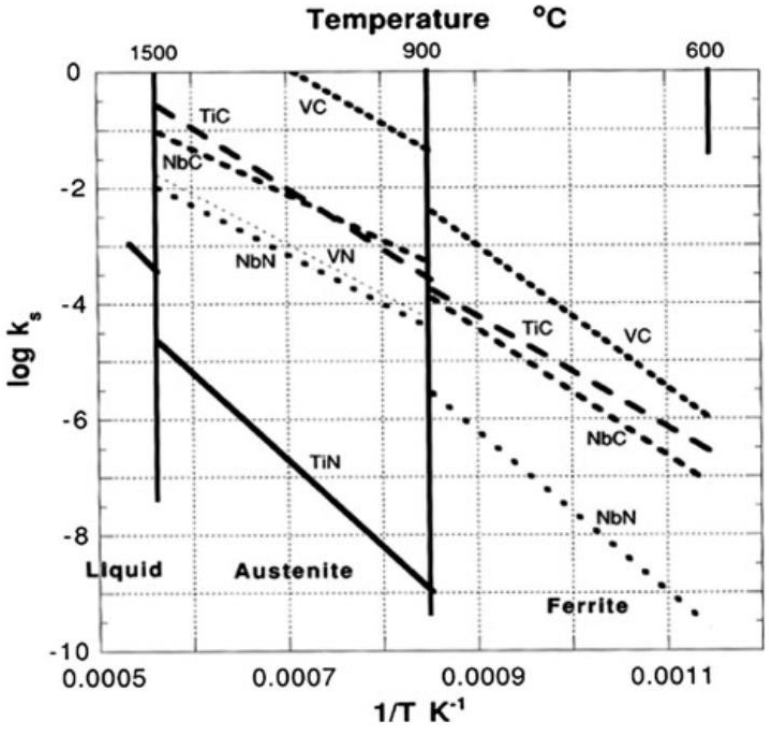

Figure 4-11: Equilibrium solubility products for microalloyed carbides and nitrides in austenite and ferrite [173].

4.1.2.3. *Fast Fourier Transforms of TEM Images*

D-spacing calculations from 34 precipitates in the heat treated steel are summarized and compared to literature values in Table 4.2. Percentage difference was reported for each of the calculated d-spacing values. 50% of the analyzed precipitates were identified as niobium carbides of various stoichiometry. Of these, 94.1% were identified as Nb_6C_5, while 5.9% were NbC. The remaining 50% of the total number of precipitates analyzed were niobium nitride precipitates of various stoichiometry. Of the niobium nitrides, 47.1% were $Nb_{0.84}N$, 23.5% $NbN_{0.801}$, 11.8% $NbN_{0.85}$, 11.8% $NbN_{0.88}$, and 5.9% NbN. These results are in agreement with EELS data presented, as NbC precipitates were also identified via EELS maps of three sites in the heat treated Nb model steel.

Table 4-2: Precipitate chemistries in heat treated steel

Calculated d-spacing (Å)	Literature comparison				
	Value (Å)	Plane	% Difference*	Precipitate Identity	Reference
2.213	2.199	(020)	− 0.64	$NbN_{0.88}$	[174]
3.870	3.873	(222)	0.08	NbC	[174]
3.349	3.405	(021)	1.64	Nb_6C_5	[175]
3.915	3.909	(-111)	− 0.15	Nb_6C_5	[175]
2.980	3.002	(111)	0.73	Nb_6C_5	[175]
4.678	4.668	(020)	− 0.21	Nb_6C_5	[175]
4.831	4.830	(002)	− 0.02	$NbN_{0.801}$	[176]
3.013	3.018	(111)	0.17	Nb_6C_5	[175]
4.021	4.021	(006)	0.00	$Nb_{0.84}N$	[177]
4.971	4.969	(001)	− 0.04	Nb_6C_5	[175]
2.992	2.988	(111)	− 0.13	Nb_6C_5	[175]
4.044	4.021	(006)	− 0.57	$Nb_{0.84}N$	[177]
3.004	3.002	(111)	− 0.07	Nb_6C_5	[175]
2.196	2.197	(200)	0.05	NbN	[178]
3.508	3.480	(021)	− 0.80	Nb_6C_5	[175]
2.056	2.130	(004)	3.47	$NbN_{0.801}$	[176]
3.355	3.405	(021)	1.47	Nb_6C_5	[175]
4.822	4.828	(002)	0.12	$NbN_{0.85}$	[179]
2.912	2.985	(009)	2.44	$Nb_{0.84}N$	[177]
4.928	4.926	(002)	− 0.04	$NbN_{0.801}$	[176]
3.037	3.026	(111)	− 0.36	Nb_6C_5	[175]
2.192	2.192	(131)	0.00	Nb_6C_5	[175]
4.834	4.837	(002)	0.06	$NbN_{0.85}$	[179]
3.485	3.480	(021)	− 0.14	Nb_6C_5	[175]
2.855	2.985	(009)	4.36	$Nb_{0.84}N$	[177]
2.075	2.130	(004)	2.58	$NbN_{0.801}$	[176]
3.336	3.293	(006)	− 1.31	$Nb_{0.84}N$	[177]
3.464	3.480	(021)	0.46	Nb_6C_5	[175]
3.229	3.237	(021)	0.25	Nb_6C_5	[175]
2.228	2.199	(020)	− 1.32	$NbN_{0.88}$	[174]
2.903	2.985	(009)	2.75	$Nb_{0.84}N$	[177]
2.875	2.985	(009)	3.68	$Nb_{0.84}N$	[177]
3.287	3.293	(006)	0.18	$Nb_{0.84}N$	[177]
3.573	3.480	(021)	− 2.68	Nb_6C_5	[175]

*Calculated via $\frac{V_{true} - V_{observed}}{V_{true}} \times 100\%$, where V_{true} and $V_{observed}$ represent the literature and measured d-spacing values, respectively.

4.1.3. ATOM PROBE TOMOGRAPHY

The heat treatment applied to the as-received Nb model steel led to Nb-based precipitates of suitable dimensions for APT analyses. More specifically, a greater percentage of precipitates less than 10 nm in width were found in the heat treated model steel when compared to the as-received. Due to the significant difference in ion yield between electropolishing and electropolishing combined with PFIB-milling, as presented in Chapter 3, electropolishing was selected for all subsequent APT sample preparation of the Nb model steel. When materials are inherently brittle, attributed to their high dislocation density or number of defects, PFIB-milling can be ineffective. However, this ion yield difference may be indicating that fracture during APT data acquisition is a random process. The matchstick may feature a locally embrittled region that limits the ion yield obtained via field evaporation, and this is only realized upon completion of the experiment.

A 2D representation of an APT reconstruction of the heat treated steel prepared by two-stage electropolishing is displayed in Figure 4-12. The Fe matrix, Nb and C are represented by orange, blue, and pink, respectively. The dimensions of the field evaporated volume are 100 nm x 100 nm x 70 nm. Regions of interest are labelled I-IV, as these were sites suspected to be NbC precipitates. These sites feature disc-like morphologies, which range in width from 7 – 16 nm. The entire specimen chemistry is presented in Table 4-3, as generated using the decomposition bulk composition function in IVAS® version 3.8.0. Sites I-IV labelled on Figure 4-12 were further studied using localized mass spectrum analyses with Nb isovalue (%) set to 1.40. The results from these analyses are displayed in Table 4-

4, with the ratio of Nb to C tabulated for each region of interest. A nearly 1 : 1 NbC ratio was found in all sites. The APT data is in agreement with NbC precipitate size and chemistry findings via TEM, FFT, and EELS, previously discussed.

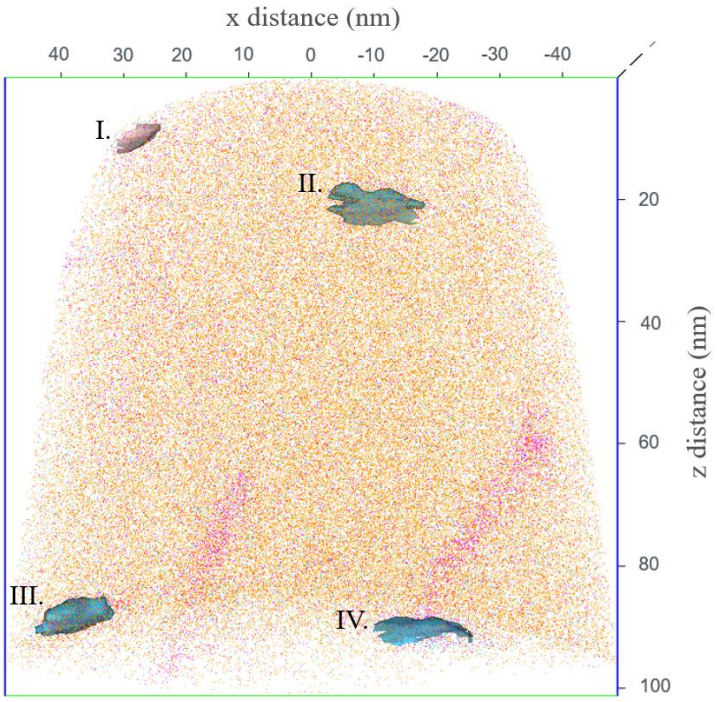

Figure 4-12: 2D view of APT reconstruction of heat treated steel matchstick. Fe, Nb, and C are represented by orange, blue, and pink, respectively.

Table 4-3: Heat treated specimen chemistry

Ion	Count	Atomic %
Fe	14,953,617	98.293
Mn	181,829	1.195
Cr	31,875	0.210
C	25,497	0.168
Si	10,363	0.068
Al	3,565	0.023
Ti	2,966	0.019
Cu	1,531	0.010
Nb	1,133	0.007
P	954	0.006

Table 4-4: Precipitate chemistries in heat treated matchstick

	Site I	Site II	Site III	Site IV
Ion Type	**Count**			
C	26	149	222	171
Fe	790	2478	5117	2860
Cr	0	1	7	5
Al	0	1	2	2
Si	1	12	33	9
P	1	0	1	4
Mn	23	34	36	32
Nb	27	121	236	148
Cu	1	1	0	0
Ti	0	1	0	2
Nb : C	**1 : 0.96**	**1 : 1.23**	**1 : 0.94**	**1 : 1.15**

4.1.4. THERMAL DESORPTION SPECTROSCOPY: CHARGING DEVICE VALIDATION

The hydrogen content in the electrolytically charged matchsticks was quantified via TDS measurements. After running a TDS test without loading any charged samples into the TDS analysis tube, it was realized that the quartz tube contributed to the hydrogen signal, as presented in Figure 4-13. The hydrogen probe outputs in units of picolitres of hydrogen (at SATP) per cm^2 of the collection plate per second. The plot indicates that above 600 °C, the quartz tube released hydrogen. A background subtraction was required to more accurately quantify the hydrogen introduced into the steel electrolytically. Figure 4-14 presents the background-subtracted hydrogen detected over time in the steel matchsticks charged with the custom cell. Temperature as a function of time is also plotted on a separate axis.

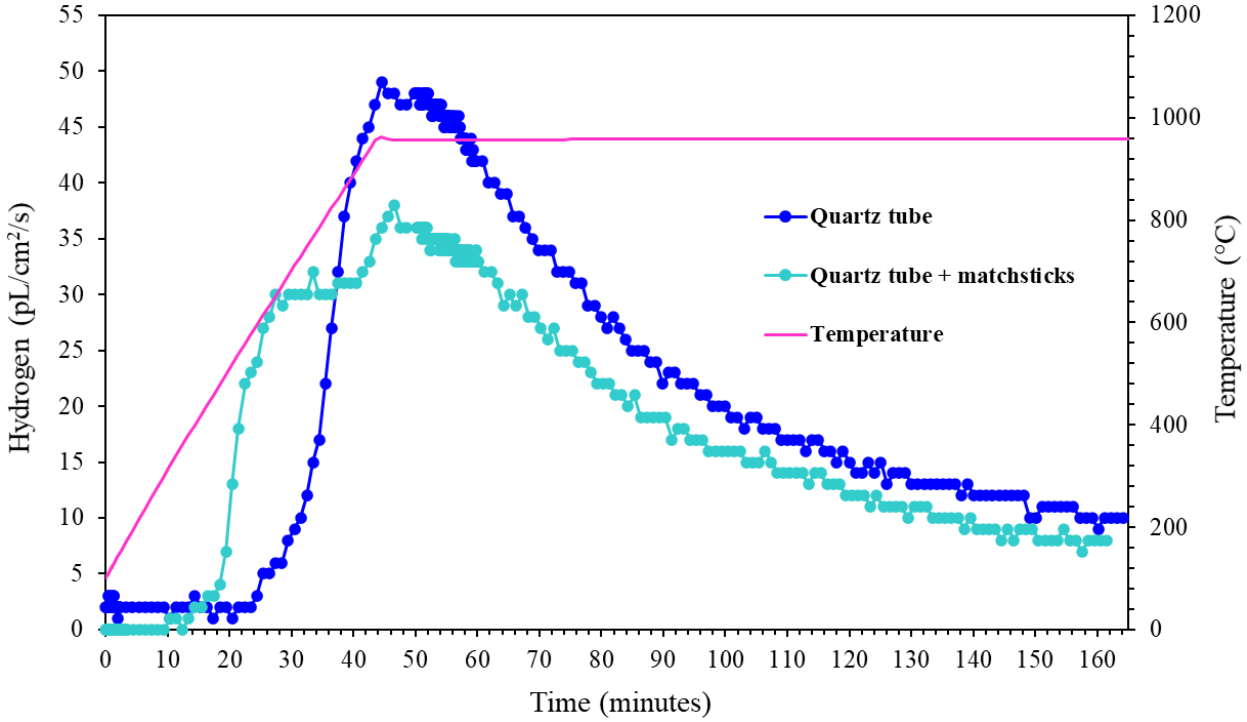

Figure 4-13: Hydrogen signal from the quartz tube compared to hydrogen signal from the quartz tube and matchsticks.

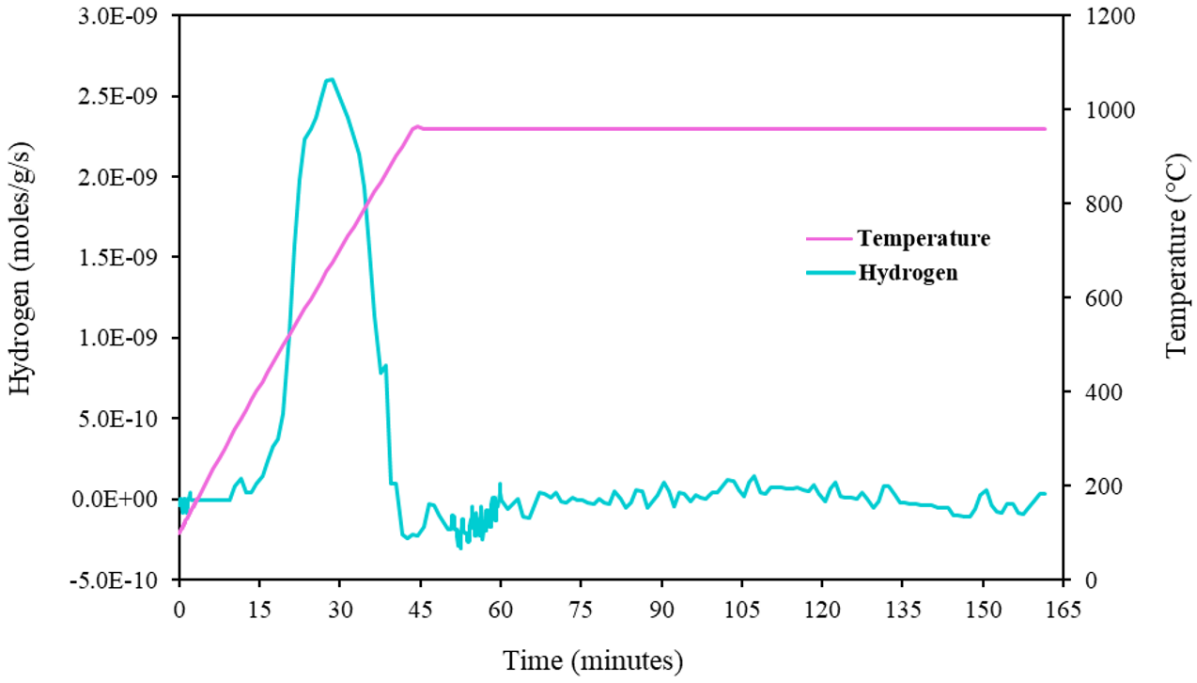

Figure 4-14: Hydrogen from charged matchsticks.

Hydrogen released at 450 °C is associated with reversibly-trapped hydrogen, so the hydrogen in the peak corresponds to approximately 2.2 ppm (mass of hydrogen/mass of steel) in reversible traps. The signal is likely contributed to by microvoids, dislocations, and/or grain boundaries, which have associated activation energies of 27.6 kJ/mol [124], 19.2-29.9 kJ/mol [124, 126], and 18-59 kJ/mol [123-125], respectively. There is an absence of hydrogen peaks above 850 °C in Figure 4-14, which suggests there is no contribution to the hydrogen signal by irreversible traps such as NbC or NbN precipitates, which have associated activation energies of 63-68 kJ/mol [129] and 100-143 kJ/mol [129], respectively. However, given the volume of the steel matchsticks and the Nb precipitate size distribution in the heat treated steel, it is likely NbC and/or NbN precipitates were present in the TDS-analyzed specimens. Presence of Nb-based precipitates in the TDS-analyzed steel matchsticks could be revealed via a destructive APT characterization following the TDS.

It was shown that the heat treatment applied to the as-received Nb model steel led to a more fine-scale size distribution of Nb-based precipitates, of suitable dimensions for APT analyses. Additionally, TDS characterization of the electrolytically charged heat treated steel validated the hydrogen-charging ability of the custom cell. With this device validated, future APT experiments incorporating deuterium pre-charging treatment of the heat treated steel can be conducted.

Specifically, a null charge experiment will be conducted, using 0.1 M NaOH in H_2O as the electrolyte for charging the matchsticks prior to APT characterization. Next, a deuterium-charge experiment shall be conducted, repeating the previously described experiment, but with electrochemical charging occurring in 0.1 M NaOD in D_2O. Recall

using deuterium allows for the differentiation between deliberately introduced hydrogen and residual hydrogen in the APT chamber. Incorporation of recently developed cryogenic and vacuum sample preparation transfer technologies [121] into the APT methodology would be advantageous, as such technologies have led to higher hydrogen yields. Collectively, these experiments should facilitate the direct observation of hydrogen-trapping sites relative to the Nb-based precipitates in the heat treated model steel.

This methodology can be repeated on matchsticks prepared from different heat treatments of the as-received model steel. Specifically, varying the holding time at 900 °C will vary the size distribution of the Nb-based precipitates. In this way, a series of heat treatments can be conducted to yield different precipitate size distributions. Electrolytic-charging pretreatment coupled to APT can be used to study the hydrogen-trapping locations relative to the Nb-based precipitates of various sizes. The data provided will facilitate an improved understanding of the influence of precipitate size on hydrogen-trapping capacity and location.

Further, the Nb wt.% can be varied in the Nb model steel, and the same series of different heat treatments applied to understand the influence of Nb-content on the hydrogen trapping capacity. Using these multi-length scale studies, the NbC, NbN, and Nb(C,N) precipitate size distribution, morphologies, hydrogen-trapping capacity, and precipitate volume fraction can be reported as a function of heat treatment. This research will aid steel manufacturers in optimizing the Nb content in HSLA steels such as X70, specifically from a HIC-mitigation perspective.

4.2. CORROSION EVALUATION OF NIOBIUM CARBIDE AND NIOBIUM NITRIDE INCLUSIONS WITHIN PURE IRON

4.2.1. SCANNING ELECTRON MICROSCOPY EXAMINATION

After polishing, the Fe-NbC and Fe-NbN model inclusion samples were Au-coated and subsequently characterized by SEM-EDS. Figure 4-15 presents a secondary electron image (SEI) at magnification 11X, providing an aerial view of the Fe-NbC inclusion. At this relatively low magnification, there is evidence of decohesion at the Fe-NbC interface.

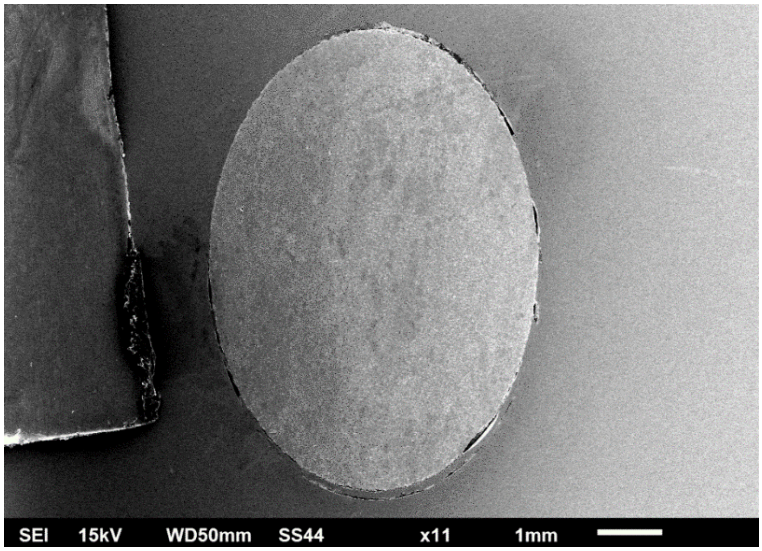

Figure 4-15: Electron image of NbC inclusion in Fe matrix.

To observe the decohesion in greater detail, images at 100X magnification were taken at the interface. A backscattered electron image of an interfacial area, and the corresponding EDS maps are shown in Figure 4-16. In the electron image, the decohesion is apparent, likely attributed to the difference in the coefficient of thermal expansion value for the two materials that were vacuum hot-pressed to form the sample. The EDS maps verify the presence of a Nb and C-containing core, and surrounding Fe-matrix, as reported

by the manufacturer. Without changing the imaging parameters, additional electron imaging and EDS analyses were conducted at the inclusion core, motivated by the low carbon signal obtained via EDS at the interface. Figure 4-17 displays a SEI and EDS maps acquired from this region. Both Nb and C are present, with the C signal clearer than the signal shown in Figure 4-16.

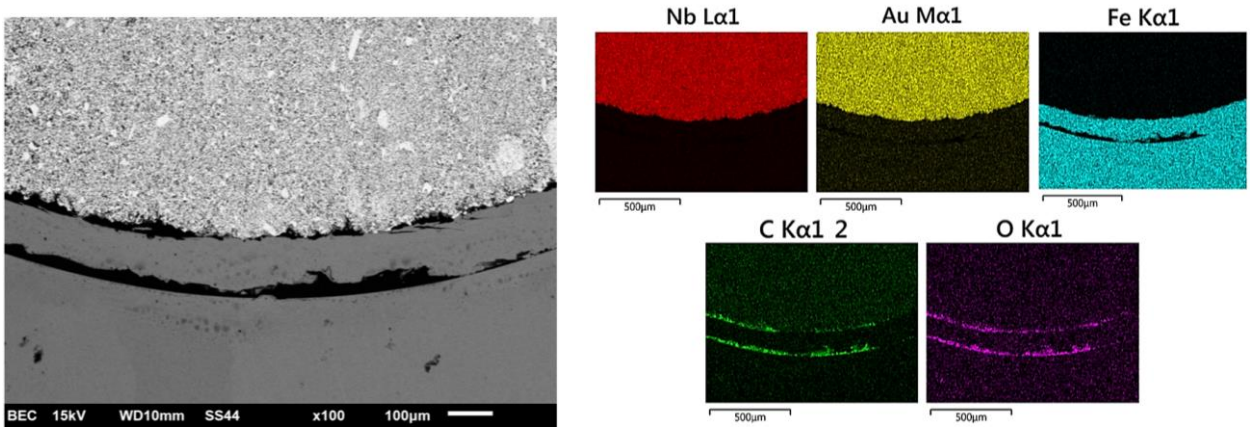

Figure 4-16: Electron image of Fe-NbC interface and corresponding EDS maps.

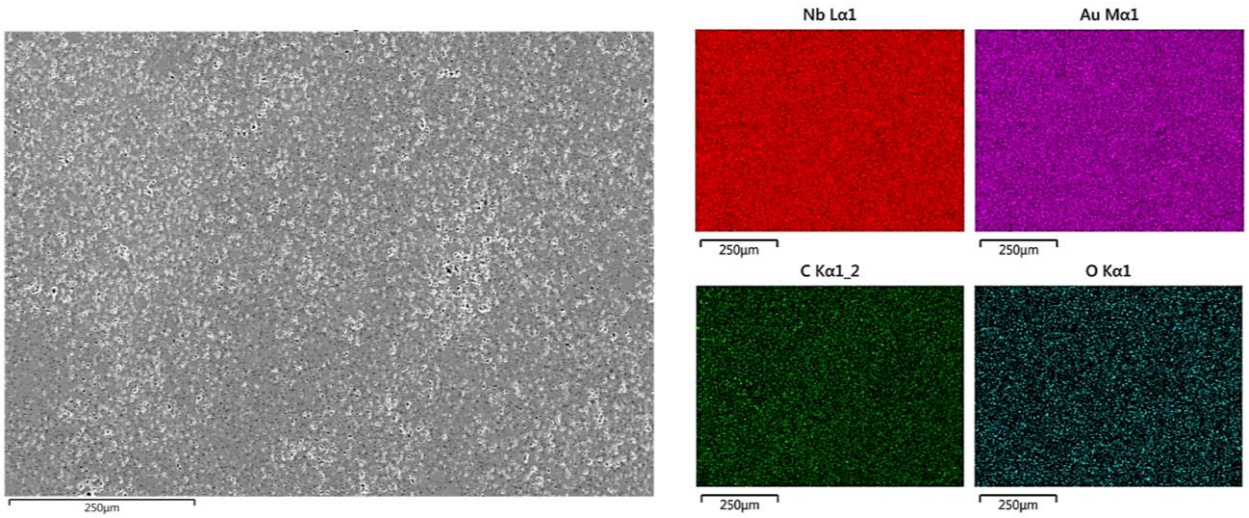

Figure 4-17: Electron image of NbC inclusion center and corresponding EDS maps.

The SEI at 11X magnification shown in Figure 4-18 displays an overview of the Fe-NbN specimen. Similarly, there is evidence of decohesion at the Fe-NbN interface. An interfacial area was captured at 100X magnification to further observe the decohesion, and to perform EDS analyses. These results are presented in Figure 4-19. EDS maps verify the presence of Nb and N-containing core, and Fe surrounding matrix as reported by the manufacturer.

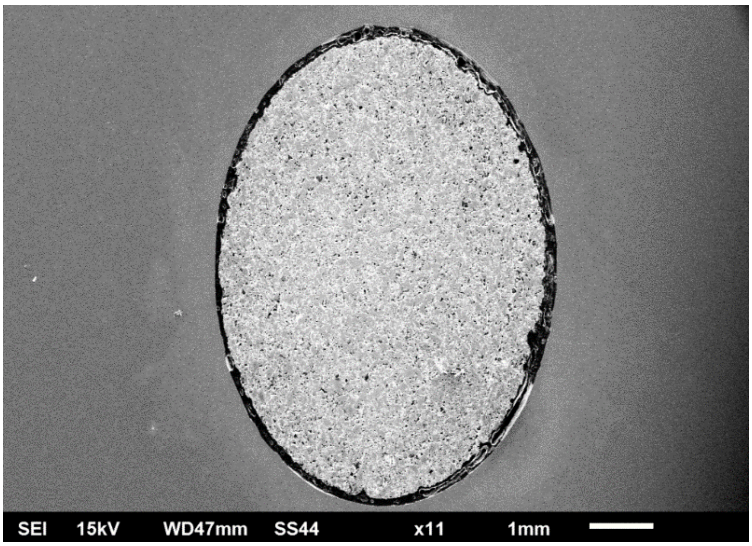

Figure 4-18: Electron image of NbN inclusion in Fe matrix.

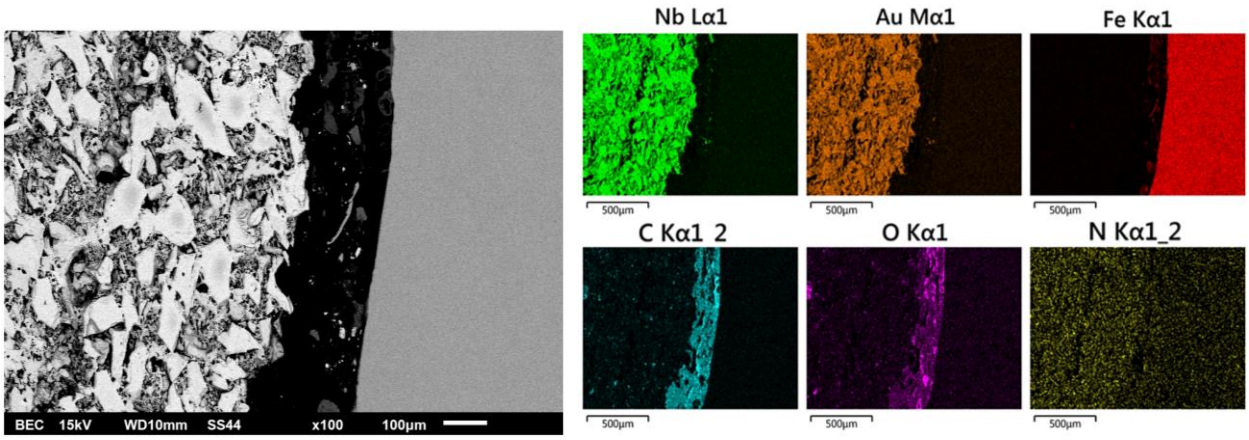

Figure 4-19: Electron image of Fe-NbN interface and corresponding EDS maps.

4.2.2. IMMERSION IMAGES IN PASSIVATING AND ACTIVE ELECTROLYTES

After repolishing each inclusion type to 1200 μm, they were each immersed in a passivating solution, which was selected as it is an alkaline saline solution known to spontaneously passivate steel [167]. The immersion images captured for the Fe-NbC specimen over 12 hour intervals for a total time of 48 hours are summarized in Figure 4-20. There were no changes observed on the Fe-NbC model inclusion working surface over the 48 hours of immersion in the passivating solution. Select immersion images of the Fe-NbN model inclusion specimen in the passivating solution are similarly summarized in Figure 4-21. At a time of 24 hours from the start of immersion, a white corrosion product was observed at the inclusion-iron interface. More corrosion product appeared to accumulate at this location until the immersion was stopped at 48 hours. The LOM images captured before immersion, after 48 hours of immersion, and after descaling treatment are summarized for the Fe-NbC and Fe-NbN inclusions in Figures 4-22 and 4-23, respectively.

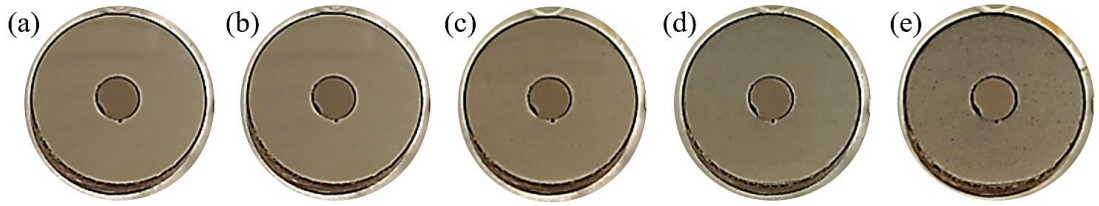

Figure 4-20: Immersion images of Fe-NbC model inclusion specimen in the passivating solution at (a) 0 hours, (b) 12 hours, (c) 24 hours, (d) 36 hours, (e) 48 hours.

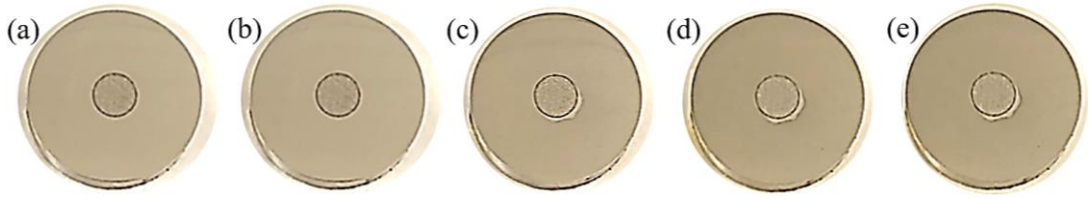

Figure 4-21: Immersion images of Fe-NbN model inclusion specimen in the passivating solution at (a) 0 hours, (b) 12 hours, (c) 24 hours, (d) 36 hours, (e) 48 hours.

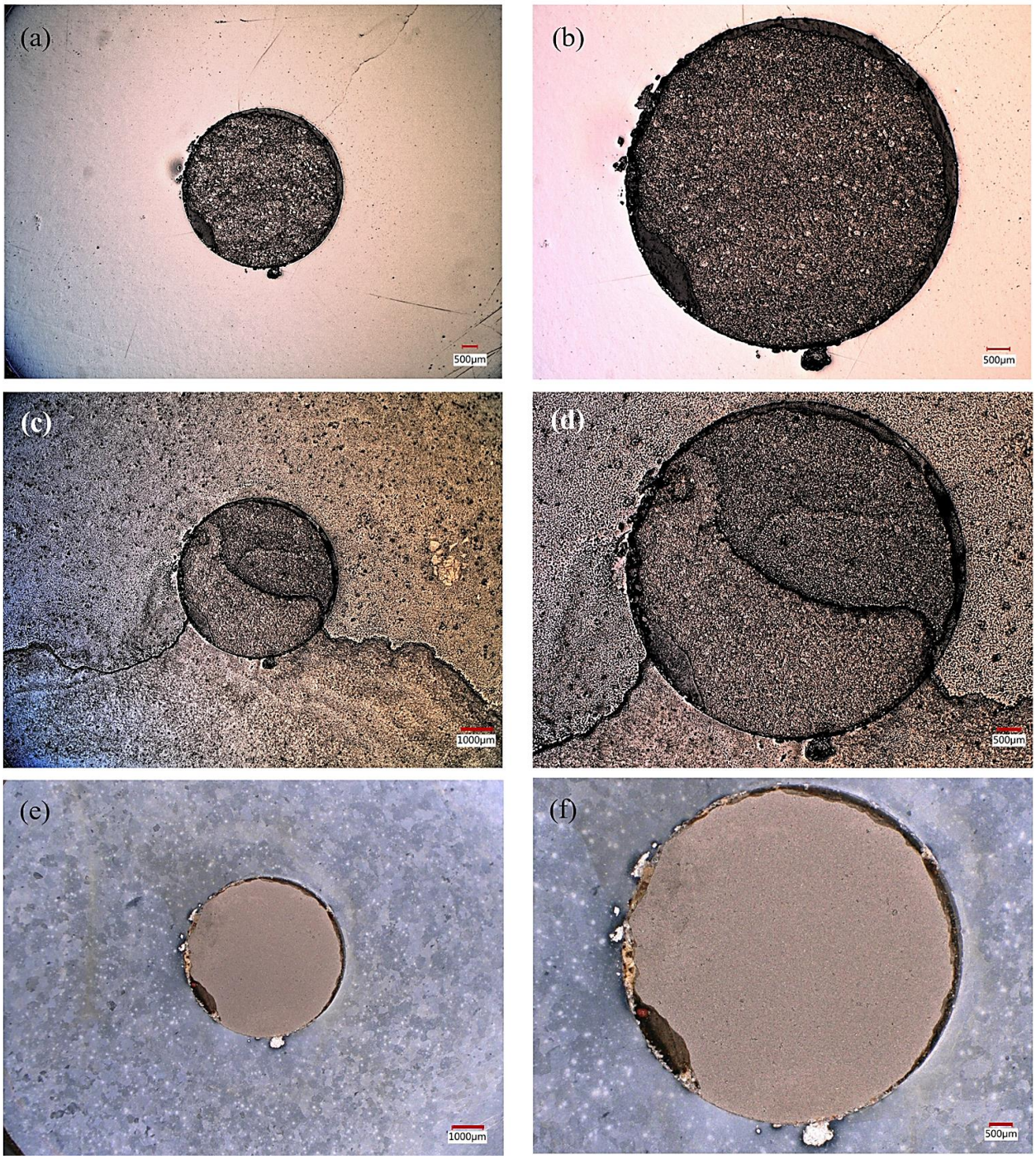

Figure 4-22: LOM images of Fe-NbC model inclusion specimen (a) at 20X before passivating solution exposure, (b) at 40X before passivating solution exposure, (c) at 20X after 48 hours of passivating solution exposure, (d) at 40X after 48 hours of passivating solution exposure, (e) at 20X after descaling treatment, and (f) at 40X after descaling treatment.

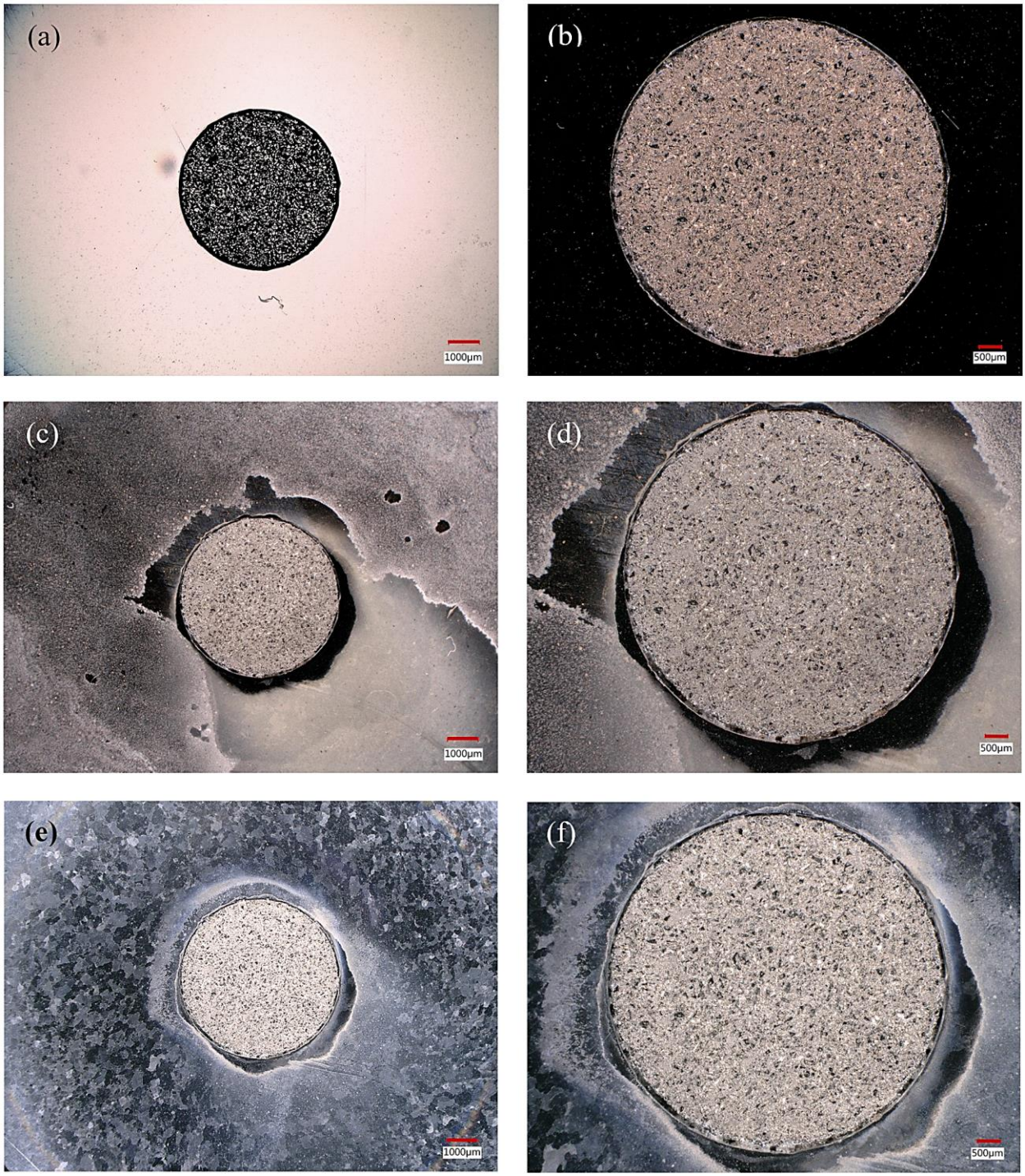

Figure 4-23: LOM images of Fe-NbN model inclusion specimen (a) at 20X before passivating solution exposure, (b) at 40X before passivating solution exposure, (c) at 20X after 48 hours of passivating solution exposure, (d) at 40X after 48 hours of passivating solution exposure, (e) at 20X after descaling treatment, and (f) at 40X after descaling treatment.

The LOM images captured for Fe-NbC again show there is no significant change between the working surface before immersion in the passivating solution and after the descaling treatment was applied. However, the LOM images of the Fe-NbN working surface show corrosion occurring at the Fe-NbN interface after the 48-hour immersion in the passivating solution and subsequent descaling treatment. The corroded area has a maximum width of approximately 0.5 mm.

The working surfaces were again repolished to 1200 µm using water-based lubricants, and subsequently immersed for 48 hours in the active state corrosion solution: NS4. Recall the active solution was chosen to simulate a wet soil environment believed to cause near-neutral pH stress corrosion cracking of pipeline grade steel [168]. The immersion images captured for each of the inclusion types are summarized in Figures 4-24 and 4-25.

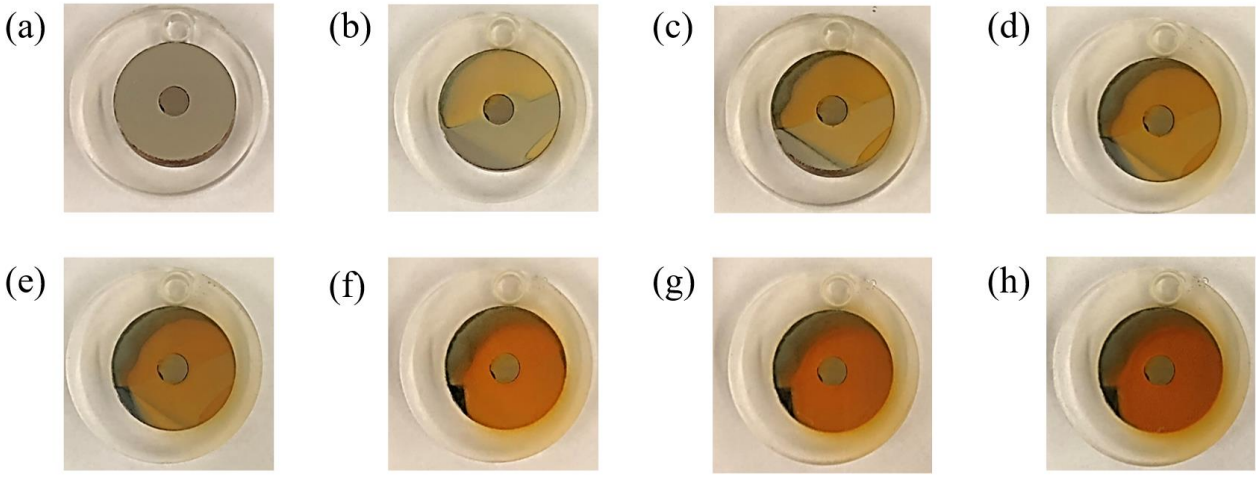

Figure 4-24: Immersion images of Fe-NbC model inclusion specimen in the active solution at (a) 0 hours, (b) 3 hours, (c) 6 hours, (d) 9 hours (e) 12 hours, (f) 24 hours, (g) 36 hours, (h) 48 hours.

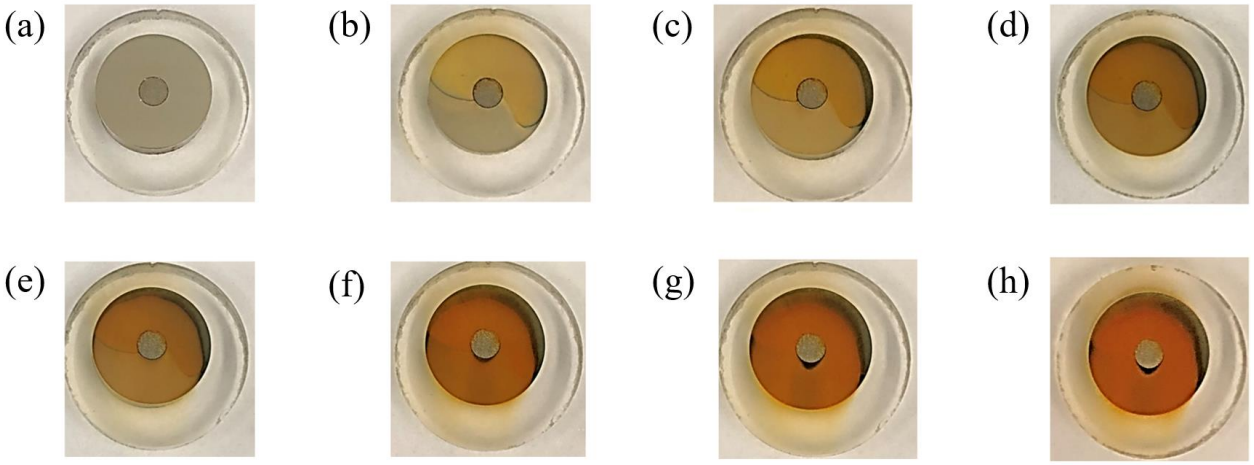

Figure 4-25: Immersion images of Fe-NbN model inclusion specimen in the active solution at (a) 0 hours, (b) 3 hours, (c) 6 hours, (d) 9 hours (e) 12 hours, (f) 24 hours, (g) 36 hours, (h) 48 hours.

For both the Fe-NbC and Fe-NbN model inclusion specimens, corrosion product is first evident at the 3 hour mark and accumulated until the end of the immersion at 48 hours. In both cases, the orange-coloured corrosion product gathered on the Fe matrix rather than the inclusion core. However, in Figure 4-25 there appeared to be a halo-like corroded region at the Fe-NbN interface, not observed in the immersion images of Fe-NbC in Figure 4-24. LOM images of the working surfaces before NS4-immersion, immediately after 48 hours of immersion, and after descaling treatment are presented at various magnifications are presented for the Fe-NbC and Fe-NbN specimens in Figures 4-26 and 4-27, respectively. Again, a halo-like corroded region appears around the interface of the Fe-NbN sample, but this phenomenon is absent in the images taken of the Fe-NbC sample. For both the Fe-NbC and Fe-NbN inclusion types, the LOM images after 48-hour NS4 exposure and descaling treatment support uniform corrosion of the Fe matrix, while the NbC or NbN core appeared unchanged.

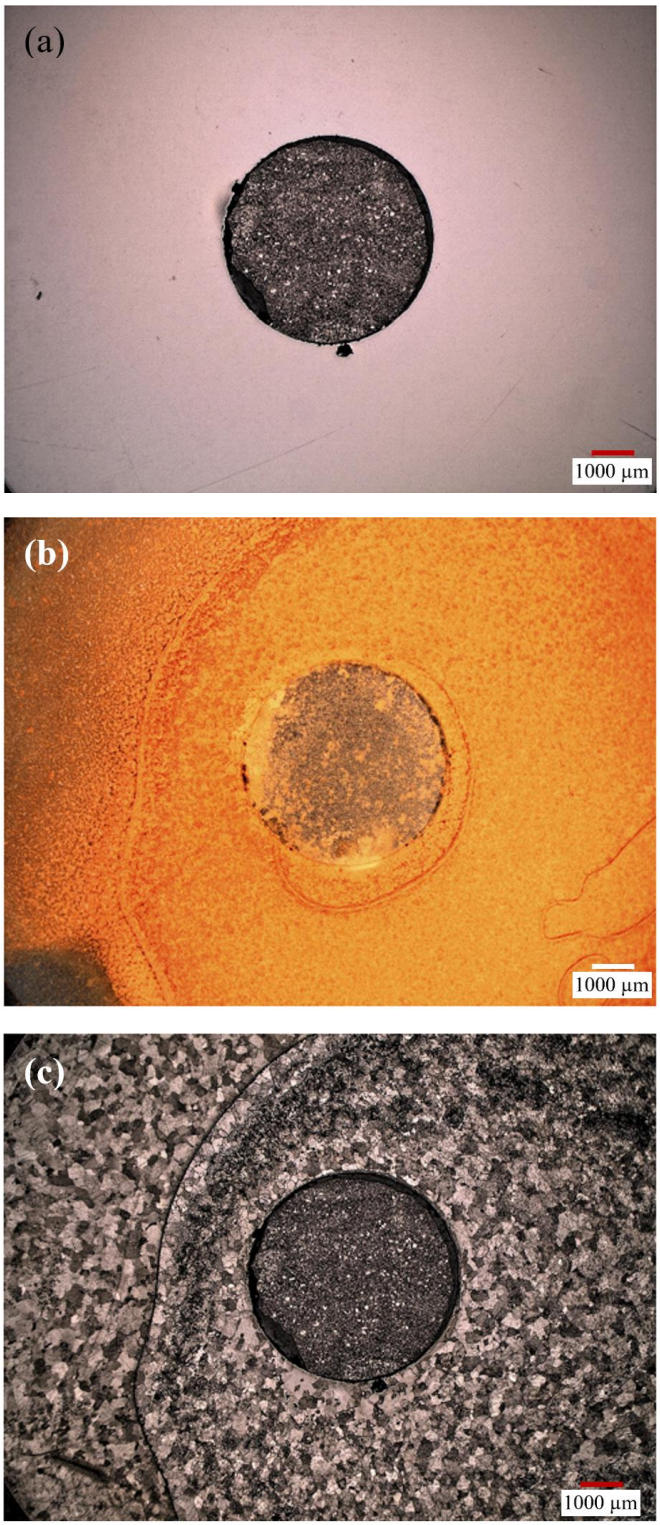

Figure 4-26: LOM images at 20X of Fe-NbC model inclusion (a) before NS4 exposure, (b) after 48 hours of NS4 exposure, and (c) after descaling treatment.

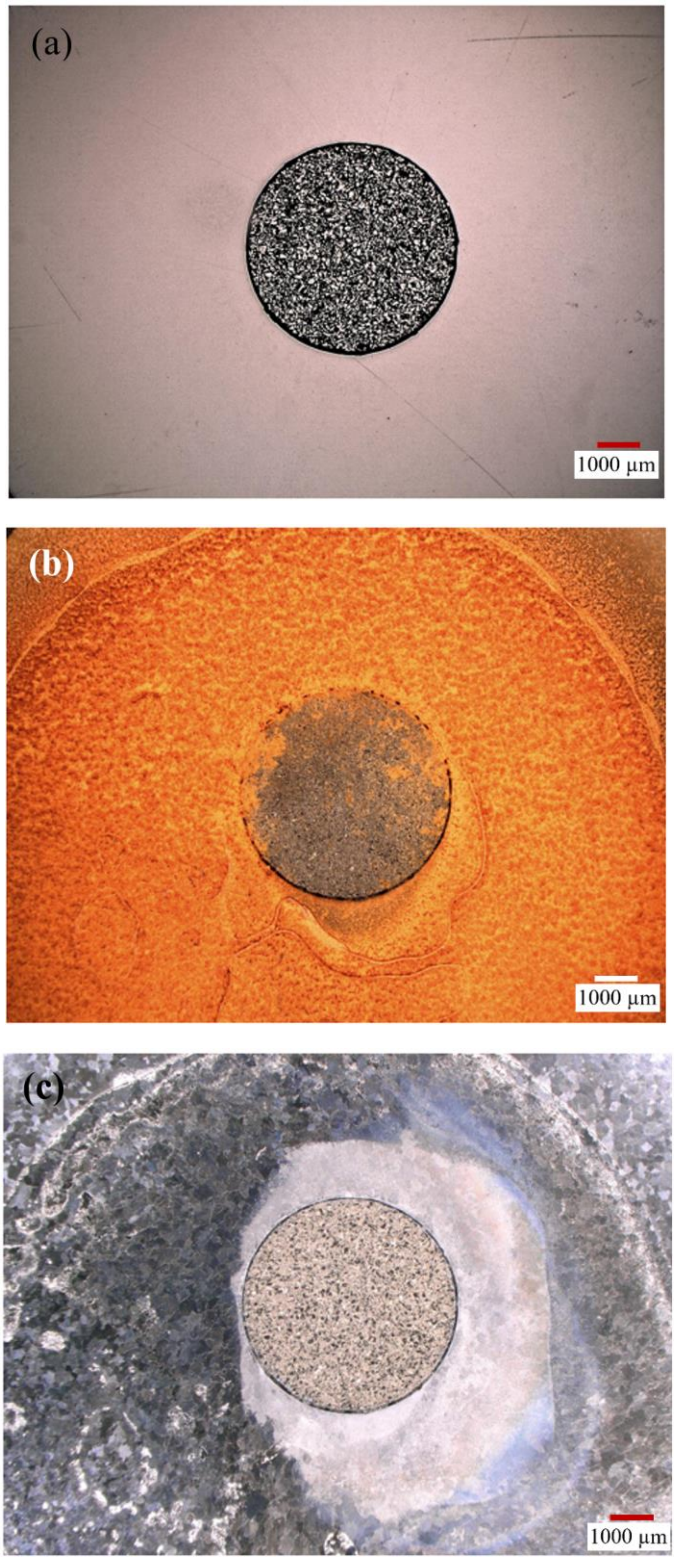

Figure 4-27: LOM images at 20X of Fe-NbN model inclusion (a) before NS4 exposure, (b) after 48 hours of NS4 exposure, and (c) after descaling treatment.

4.2.3. OPTICAL SURFACE PROFILOMETRY AREA SCANS

Optical surface profilometry (OSP) area scans were conducted before and after the 48-hour immersion in the active solution with the objective of characterizing the change in surface height across the specimen surfaces. Three trials were conducted for each inclusion type. Figures 4-28 and 4-29 present a representative trial from the triplicate OSP area scans of the NS4-exposed Fe-NbC and Fe-NbN surfaces, respectively. Because the profilometer acquires change in height measurements, it requires a consistent user-defined reference point. The height (z) value would be zeroed at (x=0, y=0) for all OSP tests. A matrix subtraction was conducted, and the resulting change in height values were mapped in Surfer® Version 12. The Δh distance in each OSP map is the result of the initial condition (before NS4 exposure) change in height values subtracted from the final condition (after 48 hour NS4 exposure) values.

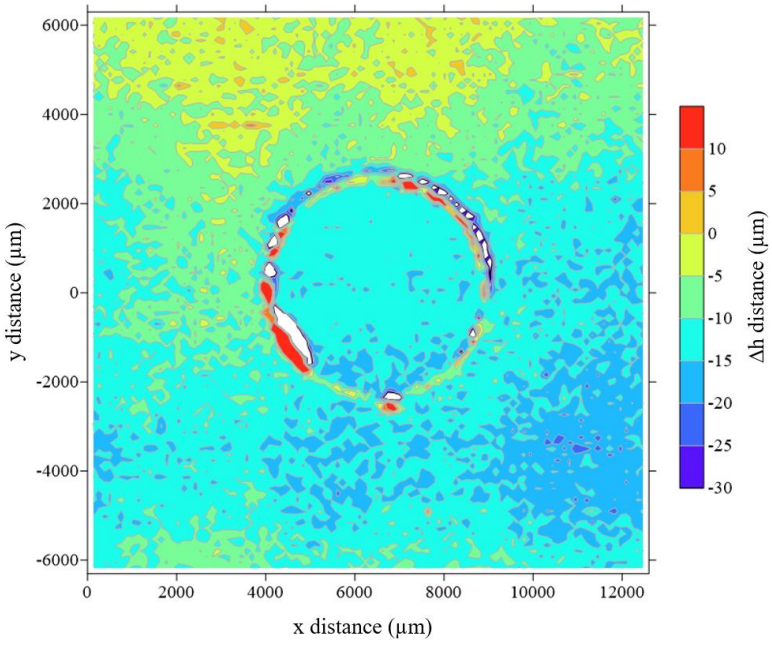

Figure 4-28: OSP area scan of Fe-NbC model inclusion specimen.

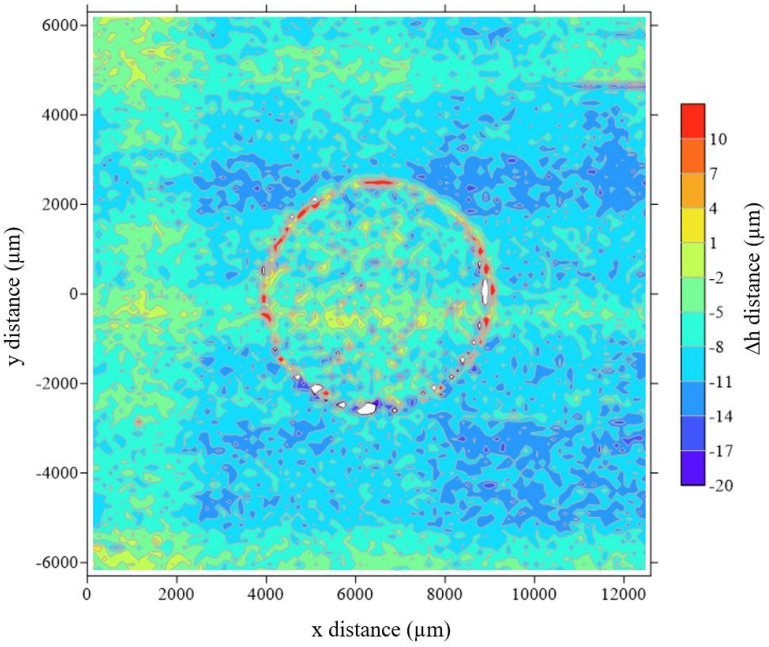

Figure 4-29: OSP area scan of Fe-NbN model inclusion specimen.

The OSP results summarized in Figure 4-28 for the Fe-NbC inclusion suggest uniform corrosion across the entire mapped sample surface. Most of the NbC inclusion had an associated change in height distance ranging from – 10 to – 15 µm, with small fractions of the inclusion area ranging from – 15 to – 20 µm. The largest proportion of the Fe matrix also featured change in height distances ranging from – 10 to – 15 µm. The remaining fractions of the matrix area featured change in height values of 0 to –25 µm. The OSP results presented in Figure 4-29 for the Fe-NbN inclusion suggested uniform corrosion of the Fe matrix. The Fe matrix featured a larger fraction of change in height distances – 8 to – 20 µm when compared to the NbN inclusion. Both the LOM and OSP acquired from the Fe-NbN specimen support a uniform corrosion of the Fe matrix.

4.2.4. POTENTIODYNAMIC POLARIZATION OF MODEL INCLUSIONS

To further evaluate the corrosion mechanism of NbC and NbN inclusions in pure Fe, potentiodynamic polarizations were conducted in triplicate for each material in the passivating and active solutions. A representative trial of each NbC, NbN, and Fe in the passivating and active solutions are presented in Figures 4-30 and 4-31, respectively. The average corrosion potential corresponding to each material in the passivating and active solutions are presented in Tables 4-5 and 4-6, respectively. Standard deviation is reported with the corrosion potentials.

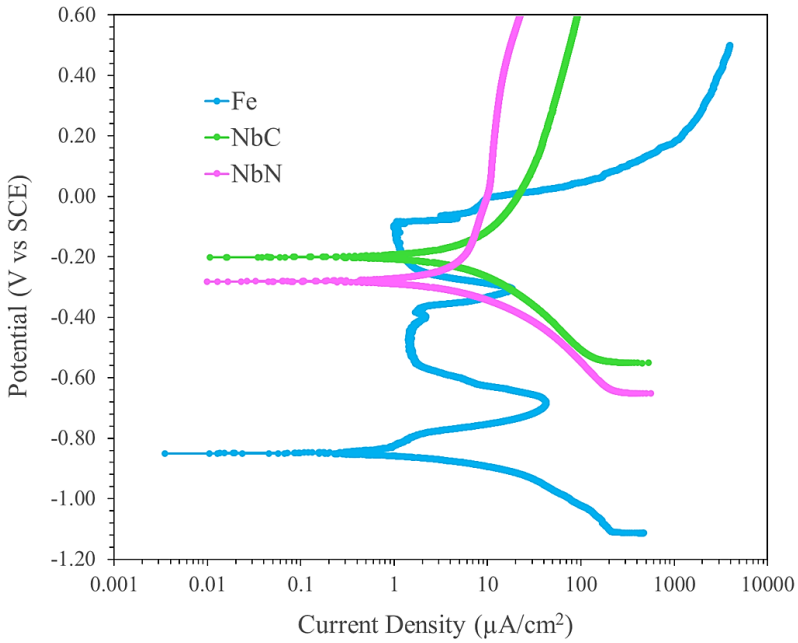

Figure 4-30: Potentiodynamic polarization curves in passivating solution for Fe, NbC, and NbN.

Table 4-5: Corrosion potentials in passivating solution

Sample	Corrosion potential (mV)
Fe	-857 ± 6
NbC	-206 ± 17
NbN	-271 ± 23

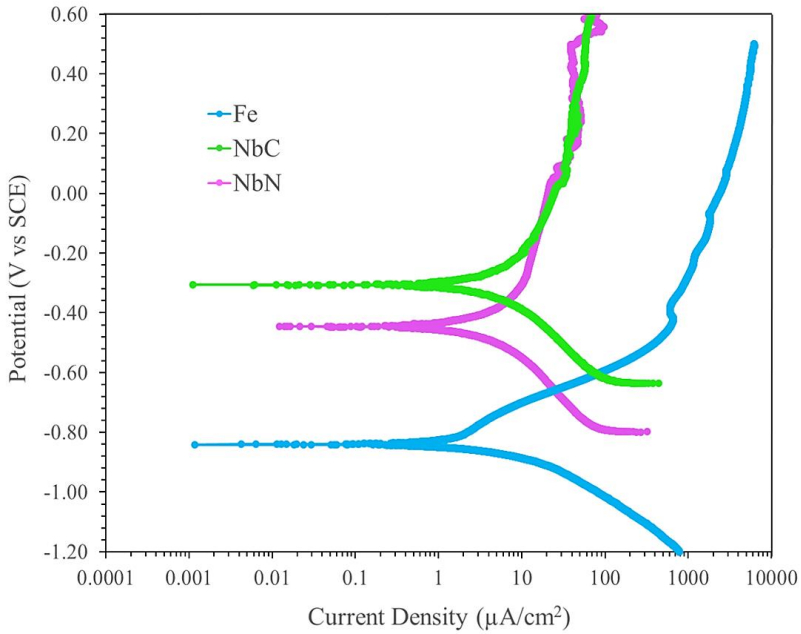

Figure 4-31: Potentiodynamic polarization curves in active solution for Fe, NbC, and NbN.

Table 4-6: Corrosion potentials in active solution

Sample	Corrosion potential (mV)
Fe	-841 ± 21
NbC	-299 ± 24
NbN	-485 ± 90

Both the passivating and active solution potentiodynamic polarization results indicate Fe is less noble than both the NbC and NbN inclusions, with NbC demonstrating the highest nobility. Because NbC and NbN particles are more noble than the steel matrix, they have driving force for galvanic corrosion with the particles serving as cathodes. The Fe-NbC or Fe-NbN galvanic couple likely leads to increased local H_2 generation, which can ultimately diffuse into the steel matrix and contribute to HIC.

Fe featuring a lower corrosion potential than NbC is consistent with Oruela *et al.*'s studies [155], which showed that the corrosion potentials of all NbC-coated AISI 1045 steels were higher than that of the uncoated steel. This result is also consistent with the research of Fernandes *et al.* [156], which also demonstrated through potentiodynamic polarization measurements that NbC features higher nobility than an uncoated AISI 52100 steel. Fe featuring lower corrosion potential than NbN is supported by the potentiodynamic polarization results from Wang *et al.* [157] and Fonseca *et al.* [158].

Recent studies by Clark *et al.* [180] investigated the role of NbC inclusions in initiating localized corrosion of a Cr-Ni-Nb stainless steel using a wide range of techniques, including AFM, SKPFM, SVET, SEM-EDS, FIB-SEM, time lapse microscopy (TLM), and electrochemical atomic force microscopy (EC-AFM), to evaluate the corrosion over multiple length scales. Volta potential mapping indicated NbC inclusions were up to 30 mV more noble compared to the stainless steel matrix. Additionally, anodic dissolution of the stainless steel matrix was observed around NbC precipitates. The visualized NbC precipitates had diameters of several microns. They observed more pitting around areas with a higher density of Nb-rich precipitates. Thus, it was proposed that the precipitate clusters formed galvanic couples with the steel matrix, creating initiation points for intergranular corrosion.

In addition, recent research carried out by Xue *et al.* [152] evaluated the effects of nanoscale Ti and Nb carbonitrides on the corrosion initiation and propagation in a Sb-containing weathering steel using EC-AFM while soaking the material in 0.01 M $NaHSO_3$.

The matrix around the precipitated (Ti, Nb)N phases dissolved. Further, their SKPFM results demonstrated precipitated (Ti, Nb)N phases had a higher Volta potential compared to the steel matrix. These results similarly support the galvanic corrosion mechanism is acting between Fe and NbN phases, with the precipitated phase serving as a cathode and the matrix acting as the anode, accelerating corrosion.

Employing longer exposure times for the immersion tests and subsequent characterization via LOM, SEM-EDS, and OSP would aid in better understanding the corrosion mechanism at play. Future work can also incorporate in-situ synchrotron x-ray tomography [181, 182] and in-situ high speed AFM [183-185], which could work as complimentary techniques to further understand the corrosion mechanisms of NbC and NbN in X70 grade steel samples at smaller length scales. The X-ray tomography can provide a 3D view of the corroding material, although voxel sizes are on the order of 0.1 – 1 μm [181]. So, in-situ synchrotron X-ray tomography is likely limited to providing information regarding corrosion propagation around NbC and NbN inclusions greater than 1 μm in width. Because of its higher temporal and spatial resolution, high-speed AFM would be capable of providing details on the early stages of corrosion initiation around NbC and NbN inclusions and grain boundaries [180].

4.2.5. POTENTIODYNAMIC POLARIZATION OF X70

Also observed in Figure 4-30 are two passivation noses on the polarization curve for Fe, from − 550 to − 400 mV vs SCE and again from approximately −250 to −100 mV vs SCE. To understand this phenomenon, the potentiodynamic polarizations measurements were

repeated for the X70 grade steel in the passivating solution. Figure 4-32 displays the results of the polarization measurements conducted in triplicate for X70. Again, two passivation noses can be observed on the polarization curves, although the second passivation nose appears over a smaller potential (V vs SCE) range compared to what was seen in Figure 4-30. The plot is followed by Table 4-7, which tabulates the measured corrosion potentials of X70 in the passivating solution, as well as the average of -808 ± 14 mV, where the error is the calculated standard deviation. Additionally, the potentiodynamic polarization tests were repeated in triplicate for X70 in the active solution, as summarized in Figure 4-33. Similarly, the polarization curves are followed by Table 4-8, which presents the measured corrosion potentials of X70 in the active solution, and an average corrosion potential of -773 ± 28 mV, where the error reported is the standard deviation.

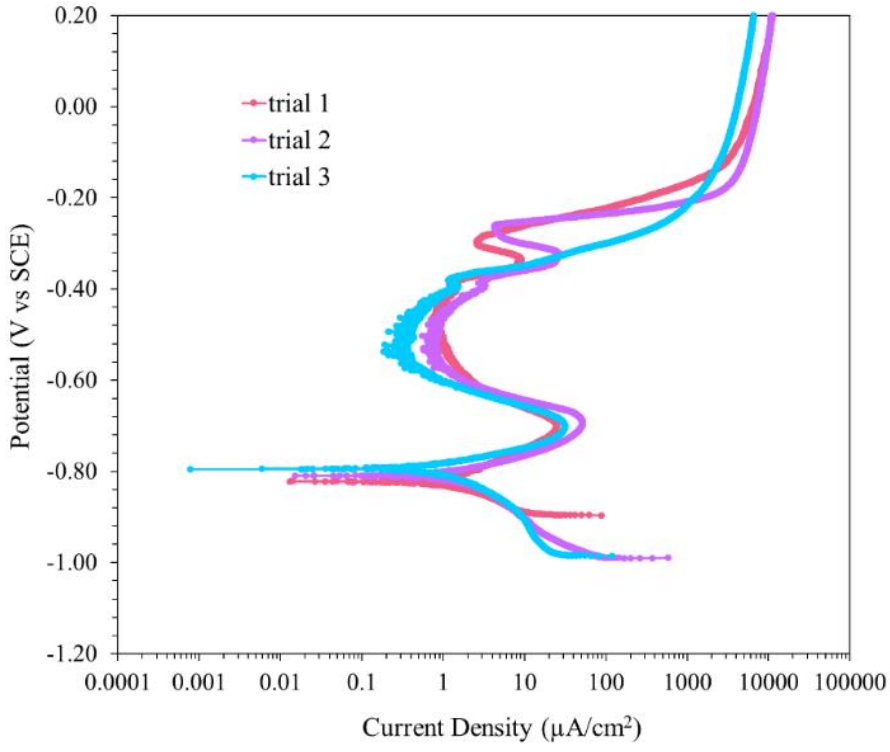

Figure 4-32: Potentiodynamic polarization curves in passivating solution for X70.

Table 4-7: Corrosion potential of X70 in passivating solution

Trial	Corrosion potential (mV)	Average (mV)
1	− 823	− 808 ± 14
2	− 808	
3	− 794	

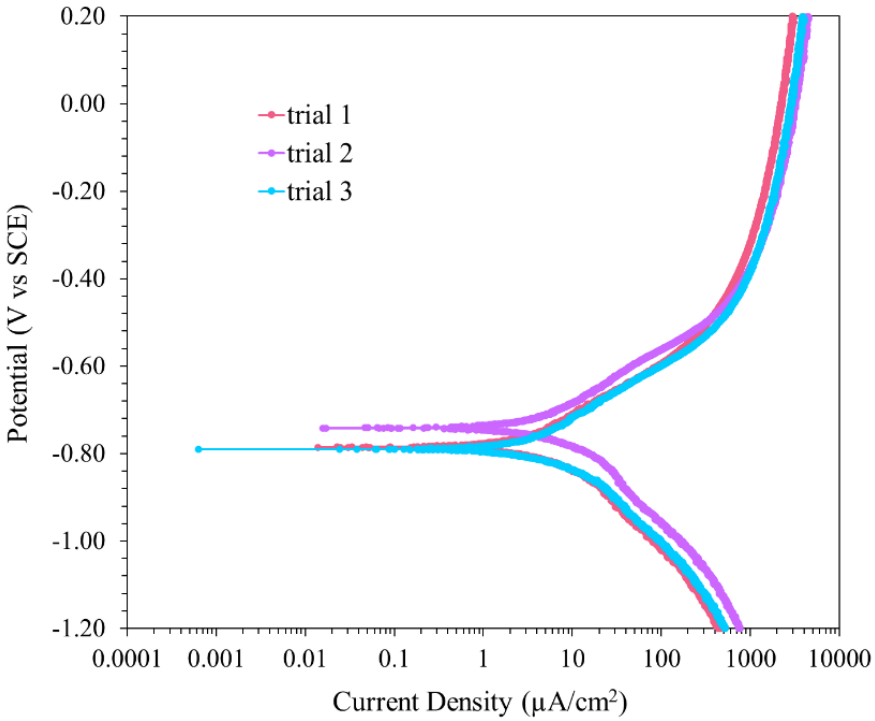

Figure 4-33: Potentiodynamic polarization curves in active solution for X70.

Table 4-8: Corrosion potential of X70 in active solution

Trial	Corrosion potential (mV)	Average (mV)
1	− 786	− 773 ± 28
2	− 742	
3	− 793	

The two passivation noses present in Figures 4-30 and 4-32 have been observed by other researchers when pipeline steel was immersed in similar electrolytes. Li *et al.* [186]

obtained polarization curves of X80 pipeline steel in 1 M $NaHCO_3$/0.5 M Na_2CO_3 buffer solution and observed a stable passive state in a potential range of 0 – 0.8 V (vs SCE), with a current density of 7.97E-5 A/cm^2. Additionally, there was a current peak appearing at approximately – 0.5 V on the polarization curve, reasoned to be related to electrochemical reactions in the solid state involving Fe transitioning to higher oxidation state.

It was expected that these different passivation windows may influence the passive film chemistry. To determine possible differences in the passivation film chemistries associated with the two passivation zones observed in Figures 4-30 and 4-32, potentiostatic polarizations were conducted, holding one X70 sample at – 480 mV and another at – 270 mV. These potentials were selected as they were the approximate midpoint potentials of each passivation nose in Figure 4-32. Each potential was held for 3 hours. The surfaces were then characterized via XPS.

4.2.6. SURFACE CHARACTERIZATION OF X70

The optical microscope image obtained from the sample held at – 480 mV is shown in Figure 4-34. The sample surface shows extensive pitting and deposition of corrosion product on the surface. XPS analyses focused on intact regions on the surface to reveal the passive film chemistry. The area analyzed is highlighted by the red oval. The corresponding survey, Fe 2p, O1s and C1s spectrum are shown in Figures 4-(35-38). The optical microscope image taken of the sample held at – 270 mV is shown in Figure 39. Similarly, the XPS analysis region is highlighted by the red oval. The associated survey, Fe 2p, O1s and C1s spectra are shown in Figures 4-(40-43).

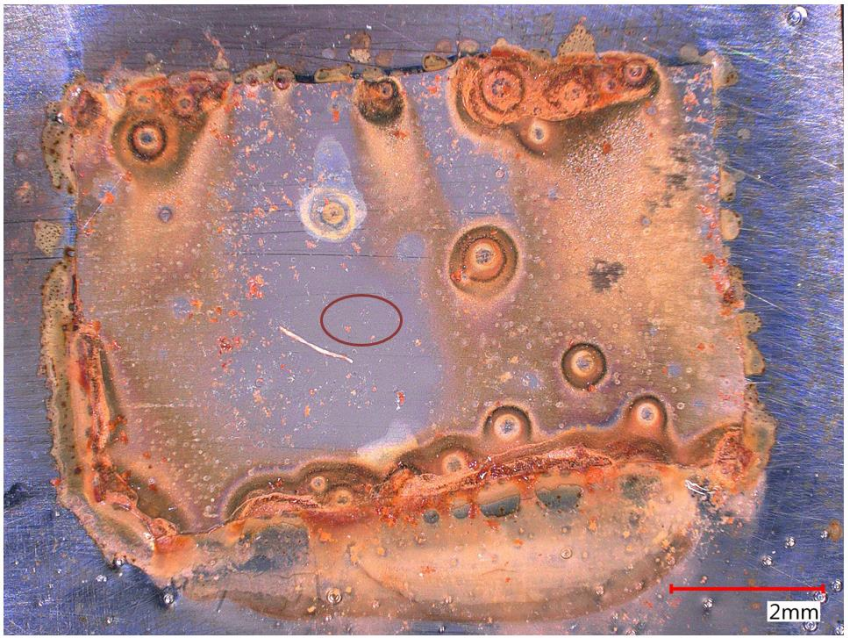

Figure 4-34: Optical micrograph of X70 working surface polarized with potential of – 480 mV, and highlighted region of interest.

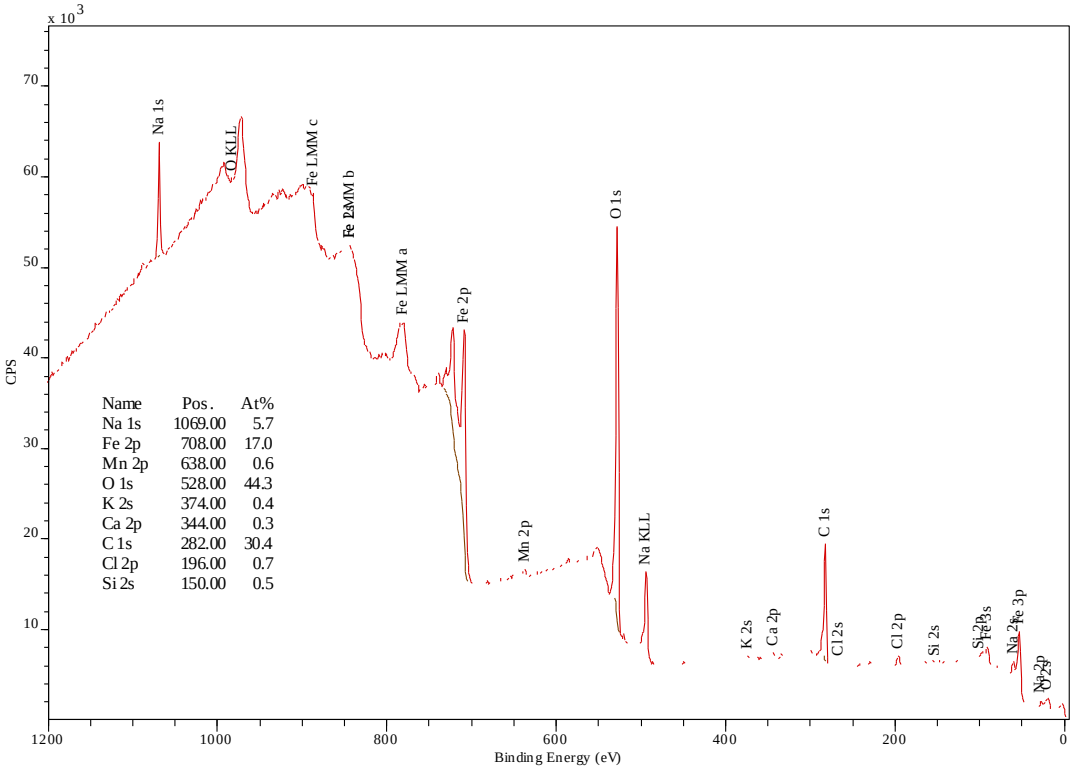

Figure 4-35: XPS survey spectrum of X70 working surface polarized with potential of – 480 mV.

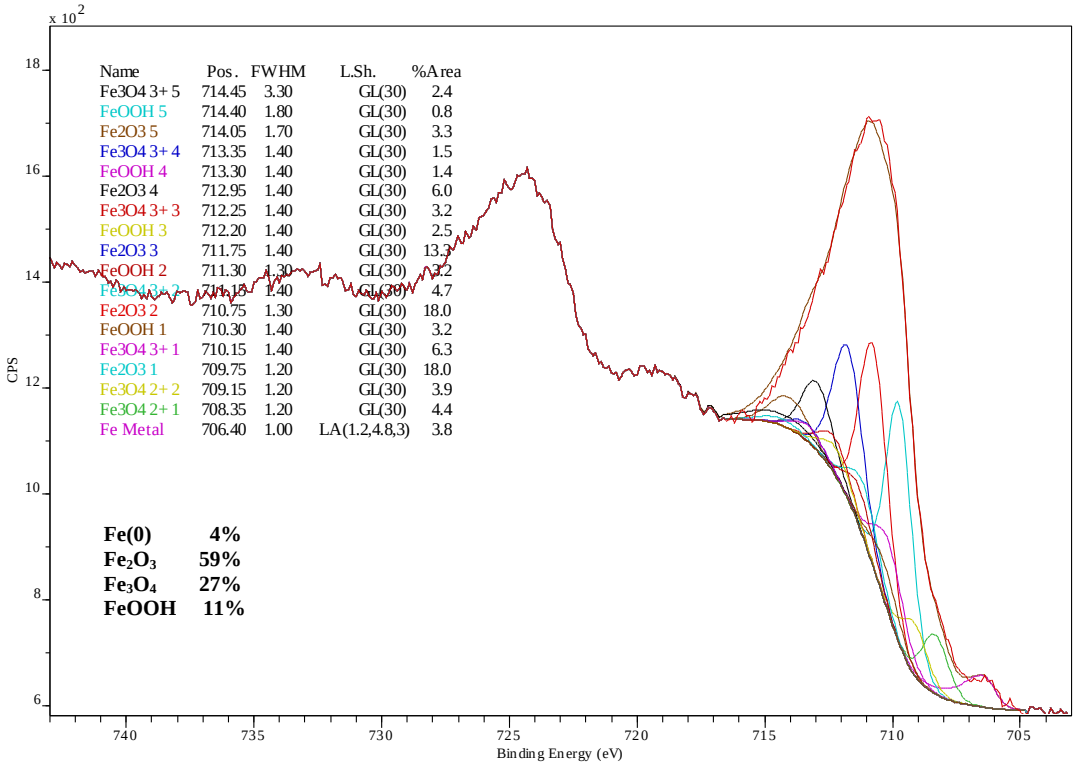

Figure 4-36: XPS Fe 2p spectrum of X70 working surface polarized with potential of – 480 mV.

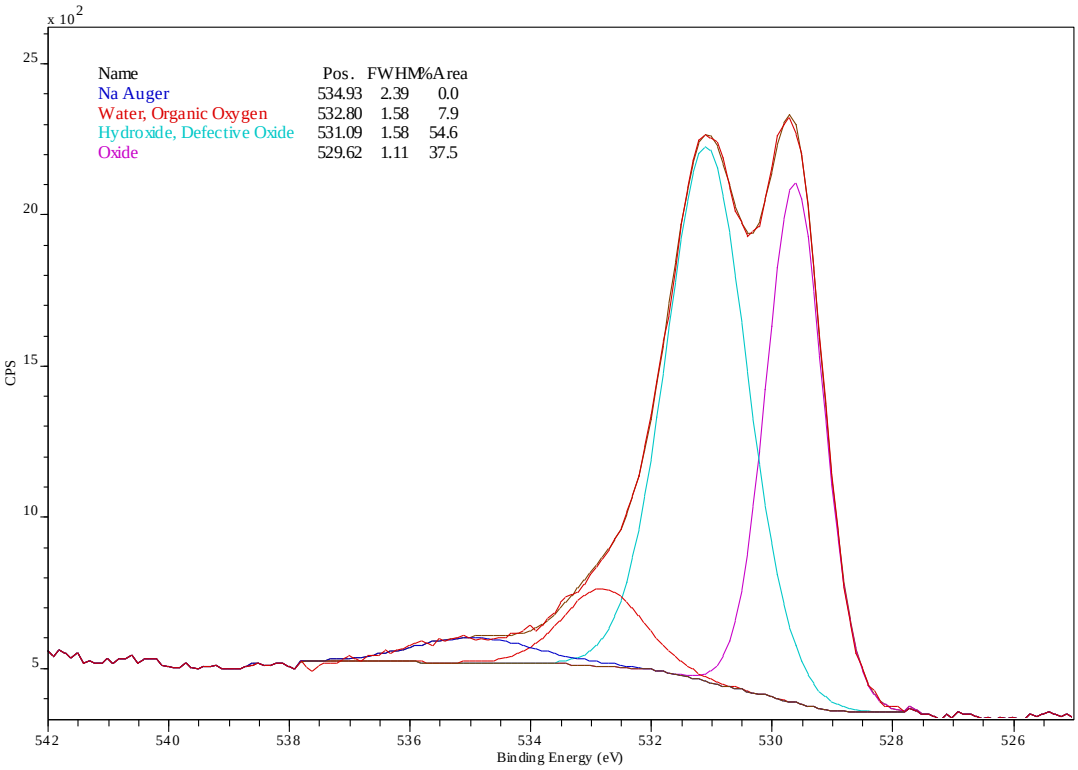

Figure 4-37: XPS O 1s spectrum of X70 working surface polarized with potential of – 480 mV.

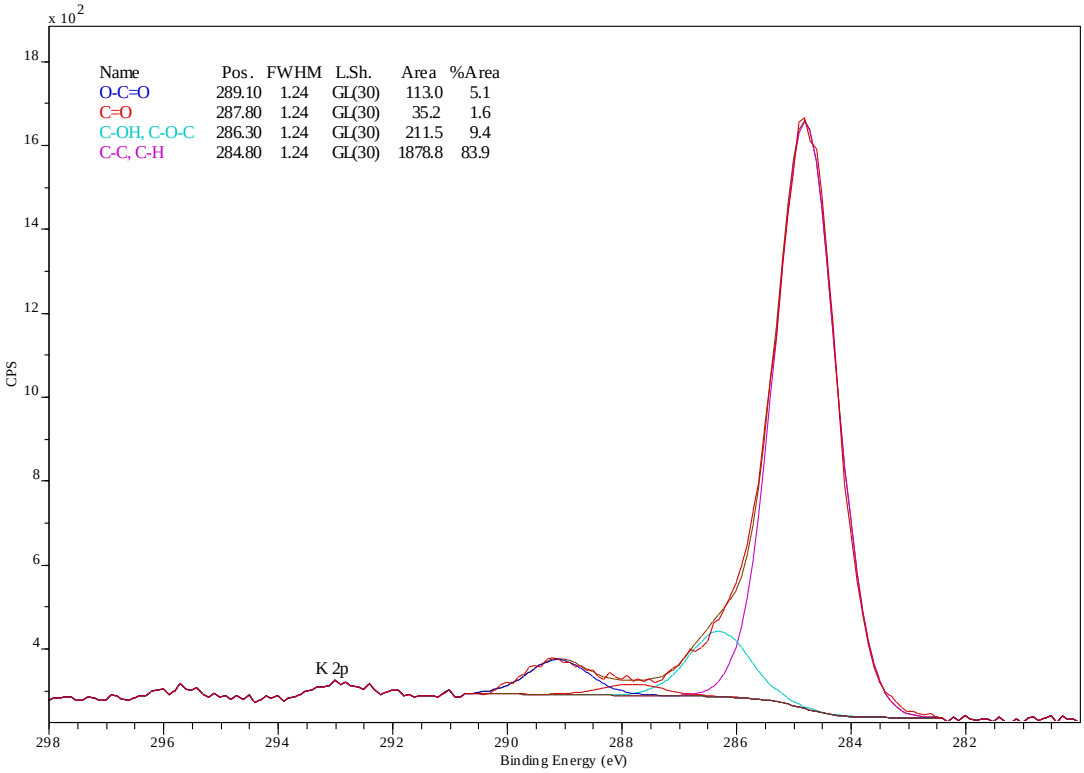

Figure 4-38: XPS C 1s spectrum of X70 working surface polarized with potential of – 480 mV.

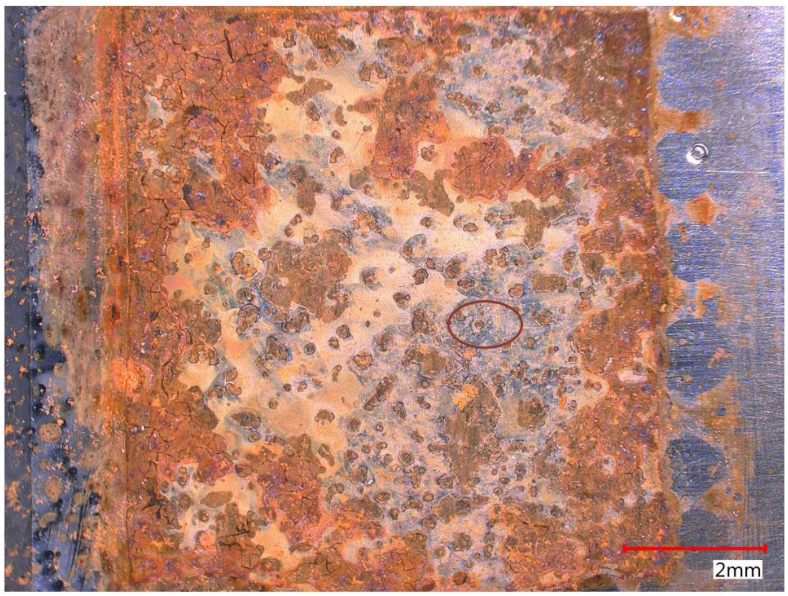

Figure 4-39: Optical micrograph of X70 working surface potentiostatically polarized with potential of – 270 mV, and highlighted region of interest.

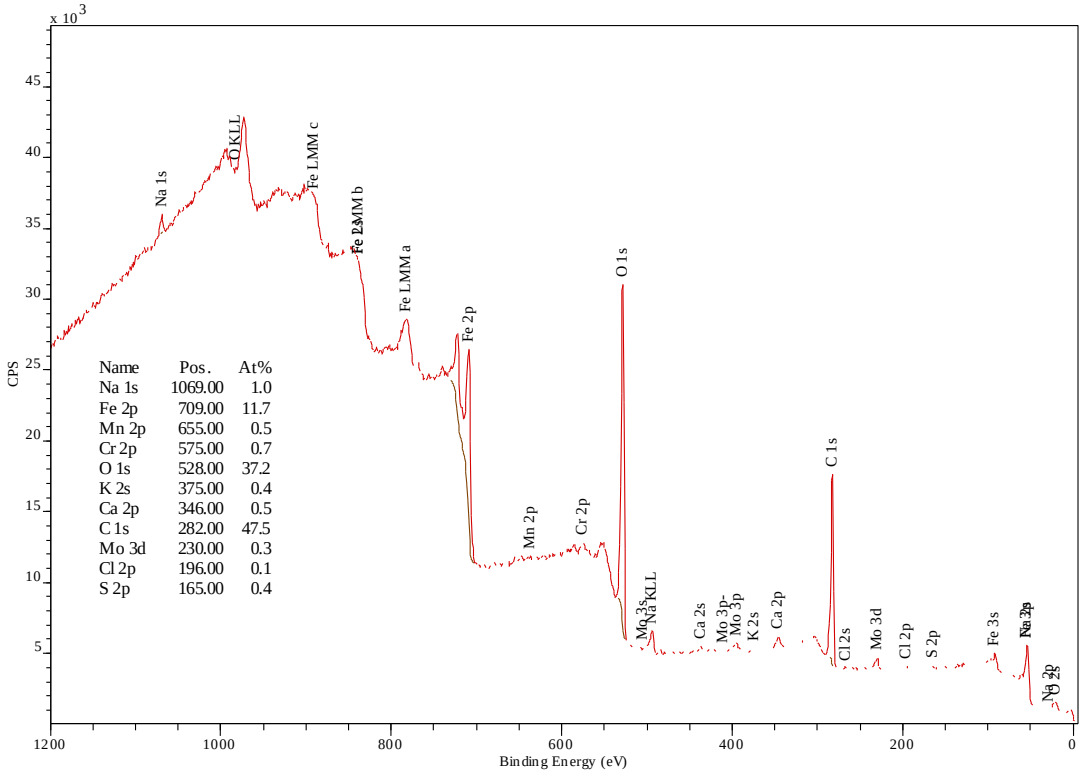

Figure 4-40: XPS survey spectrum of X70 working surface polarized with potential of – 270 mV.

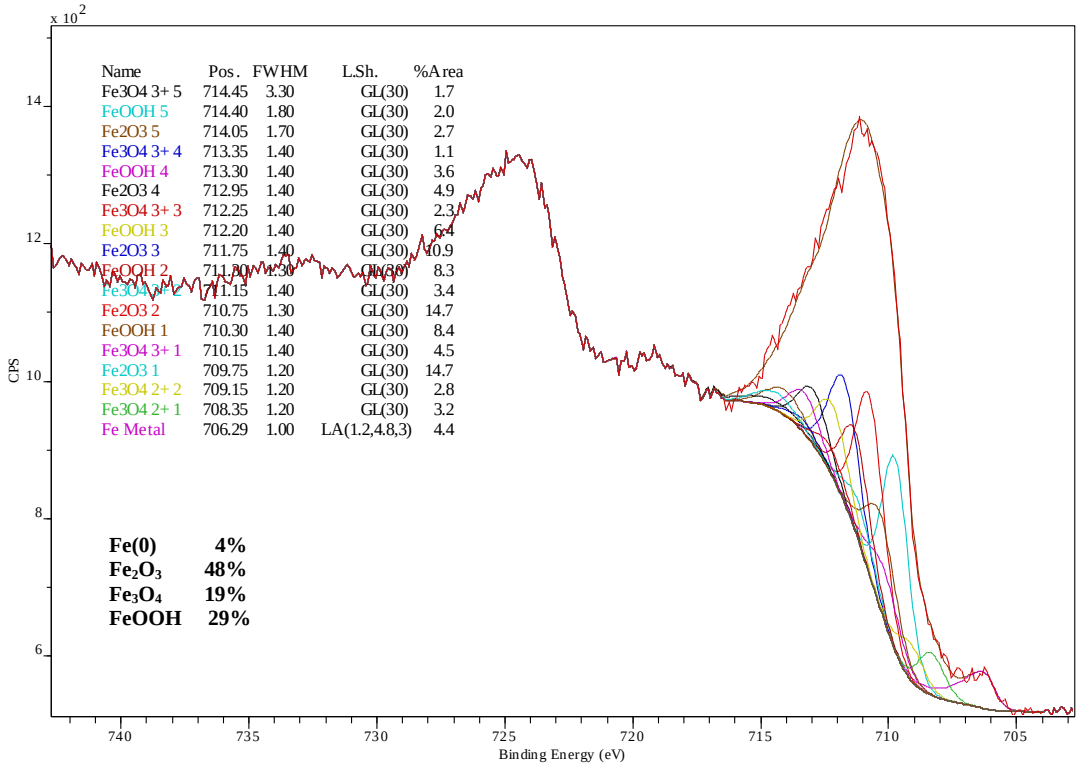

Figure 4-41: XPS Fe 2p spectrum of X70 working surface polarized with potential of – 270 mV.

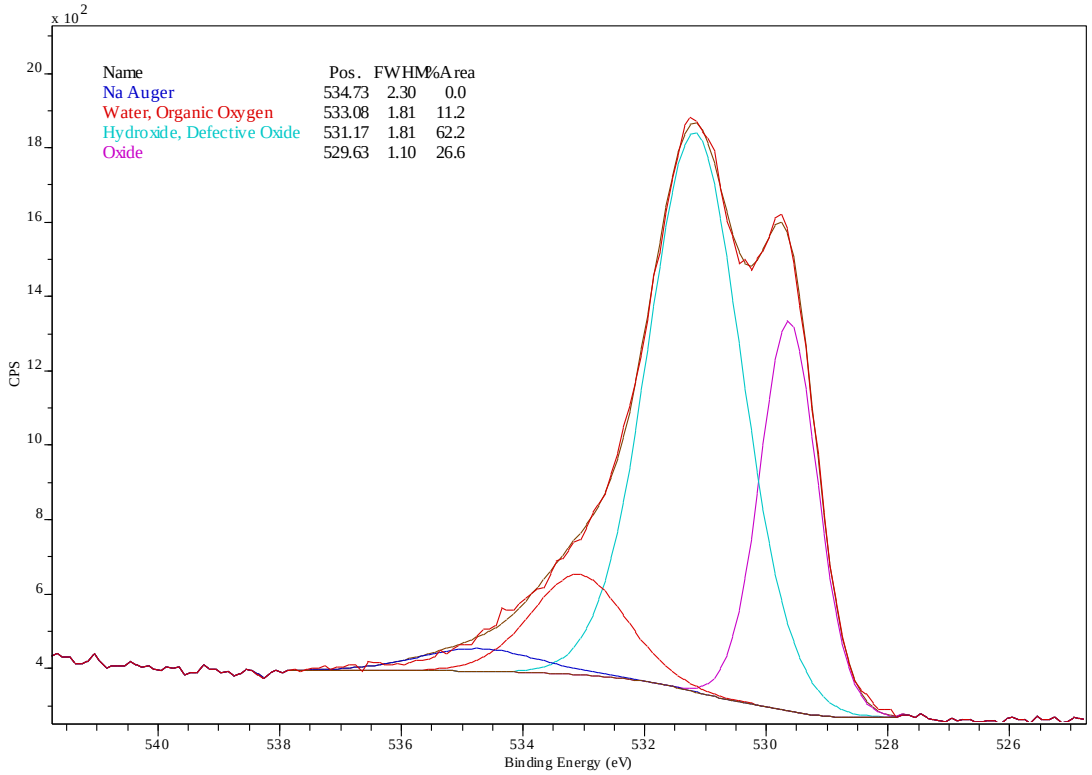

Figure 4-42: XPS O 1s spectrum of X70 working surface polarized with potential of – 270 mV.

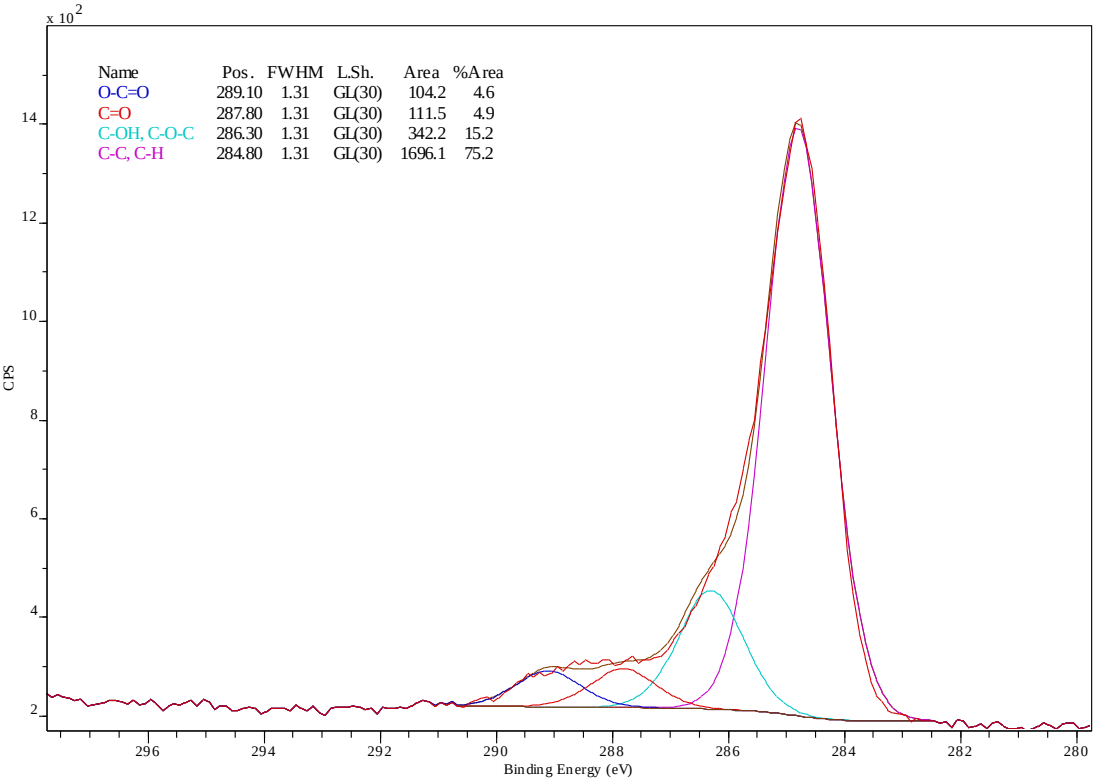

Figure 4-43: XPS C 1s spectrum of X70 working surface polarized with potential of – 270 mV.

Table 4-9 summarizes the percentage differences in the atomic % values associated with different elements. There was an absence of Si in the film on the sample held at − 270 mV, and an absence of Cr, Mo, and S in the film of the sample held at − 480 mV. The survey spectra also indicate a greater percentage of C in the region analyzed on the sample held at − 270 mV. The atomic percentage difference for C is 17.1 %. This sample also featured a lower O atomic percentage when compared to the sample held at − 480 mV. Comparing the Fe 2p spectra, it can be noticed that the X70 sample held at − 270 mV features a higher percentage area of FeOOH (18 % more), but a lower percentage area of Fe_2O_3 (11 % less) and Fe_3O_4 (8 % less). There were no significant differences in the passive film chemistries of the two X70 steel samples held at the different potentials. The secondary passivation observed in the potentiodynamic polarizations of X70 may be related to electrochemical reactions in the solid state involving Fe transitioning to higher oxidation state [186].

Table 4-9: XPS survey spectra summary for X70 held at different potentials

Sample	**− 480 mV**	**− 270 mV**	**difference**
	at. %	**at. %**	**(%)**
Na 1s	5.7	1.0	4.7
Cr 2p	0	0.7	0.7
Fe 2p	17.0	11.7	5.3
Mn 2p	0.6	0.5	0.1
O 1s	44.3	37.2	7.1
K 2s	0.4	0.4	0
Ca 2p	0.3	0.5	0.2
C 1s	30.4	47.5	17.1
Cl 2p	0.7	0.1	0.6
Si 2s	0.5	0	0.5
Mo 3d	0	0.3	0.3
S	0	0.4	0.4

5. CONCLUSIONS

From Project 1, the following conclusions were drawn:

- The experimental heat treatment of the Nb model steel increased the number of fine precipitates that are ideal for APT characterization. Majority of the precipitates (63 %) in the heat treated samples were ≤ 10 nm in width, and 24% were > 10 nm but ≤ 20 nm in width.

- APT characterization of the heat treated Nb model steel identified four NbC precipitates. All sites featured a nearly 1 : 1 NbC ratio, determined via localized mass spectrum analyses. The APT data were in agreement with NbC precipitate size and chemistry findings via TEM, FFT, and EELS.

- The custom electrolytic charging cell's ability to introduce hydrogen into the heat treated model steel matchsticks was validated using TDS. The hydrogen in the peak of the desorption spectrum corresponded to approximately 2.2 ppm (mass of hydrogen/mass of steel) in reversible traps, likely due to a combination of microvoids, dislocations, and grain boundaries. With this device validated, future APT experiments incorporating D-charging treatment of the heat treated steel can be conducted. Such experiments can reveal the hydrogen-trapping locations associated with NbC and NbNs.

From Project 2, the following conclusions were drawn:

- Both the passivating and active solution potentiodynamic polarization results indicated Fe is less noble than both the NbC and NbN inclusions, with NbC demonstrating the highest nobility. Because NbC and NbN particles are more noble than the steel matrix, they have driving force for galvanic corrosion with the particles serving as cathodes. The active corrosion case is more problematic as the Fe-NbC or Fe-NbN galvanic couple likely leads to increased local H_2 generation, which can ultimately diffuse into the steel matrix and contribute to HIC.

- Two passivation zones were detected via potentiodynamic polarization of both pure Fe and X70 grade steel. The passive film chemistries of X70 steel specimens held at two different potentials ($-$ 480 mV and $-$ 270 mV) via potentiostatic polarizations were revealed using XPS survey, Fe 2p, O1s and C1s spectra. There were no significant differences in the passive film chemistries of the two X70 steel samples held at the different potentials. The secondary passivation observed in the potentiodynamic polarizations of X70 may be related to electrochemical reactions in the solid state involving Fe transitioning to higher oxidation state.

6. REFERENCES

[1] Takahashi, J., Kawakami, K., & Kobayashi, Y. (2018). Origin of hydrogen trapping site in vanadium carbide precipitation strengthening steel. *Acta Materialia*, *153*, 193-204.

[2] Haley, D., Merzlikin, S. V., Choi, P., & Raabe, D. (2014). Atom probe tomography observation of hydrogen in high-Mn steel and silver charged via an electrolytic route. *international journal of hydrogen energy*, *39*(23), 12221-12229.

[3] Breen, A. J., *et al*. (2020). Solute hydrogen and deuterium observed at the near atomic scale in high-strength steel. *Acta Materialia*, *188*, 108-120.

[4] Ohaeri, E., Eduok, U., & Szpunar, J. (2018). Hydrogen related degradation in pipeline steel: A review. *International Journal of Hydrogen Energy*, *43*(31), 14584-14617.

[5] Li, L., Song, B., Cheng, J., Yang, Z., & Cai, Z. (2018). Effects of vanadium precipitates on hydrogen trapping efficiency and hydrogen induced cracking resistance in X80 pipeline steel. *International Journal of Hydrogen Energy*, *43*(36), 17353-17363.

[6] Mohtadi-Bonab, M. A., Szpunar, J. A., & Razavi-Tousi, S. S. (2013). A comparative study of hydrogen induced cracking behavior in API 5L X60 and X70 pipeline steels. *Engineering Failure Analysis*, *33*, 163-175.

[7] Zhang, S., Wan, J., Zhao, Q., Liu, J., Huang, F., Huang, Y., & Li, X. (2020). Dual role of nanosized NbC precipitates in hydrogen embrittlement susceptibility of lath martensitic steel. *Corrosion Science*, *164*, 108345.

[8] Garet, M., Brass, A. M., Haut, C., & Guttierez-Solana, F. (1998). Hydrogen trapping on non metallic inclusions in Cr-Mo low alloy steels. *Corrosion Science*, *40*(7), 1073-1086.

[9] Michler, T., Lee, Y., Gangloff, R. P., & Naumann, J. (2009). Influence of macro segregation on hydrogen environment embrittlement of SUS 316L stainless steel. *International Journal of Hydrogen Energy*, *34*(7), 3201-3209.

[10] Kwon, Y. J., Seo, H. J., Kim, J. N., & Lee, C. S. (2018). Effect of grain boundary engineering on hydrogen embrittlement in Fe-Mn-C TWIP steel at various strain rates. *Corrosion Science*, *142*, 213-221.

[11] Szost, B. A., Vegter, R. H., & Rivera-Díaz-del-Castillo, P. E. J. (2013). Developing bearing steels combining hydrogen resistance and improved hardness. *Materials & Design*, *43*, 499-506.

[12] Michler, T., & Balogh, M. P. (2010). Hydrogen environment embrittlement of an ODS RAF steel–Role of irreversible hydrogen trap sites. *International Journal of Hydrogen Energy*, *35*(18), 9746-9754.

[13] Lin, L., Li, B. S., Zhu, G. M., Kang, Y. L., & Liu, R. D. (2018). Effect of niobium precipitation behavior on microstructure and hydrogen induced cracking of press hardening steel 22MnB5. *Materials Science and Engineering: A*, *721*, 38-46.

[14] Mohtadi-Bonab, M. A., Karimdadashi, R., Eskandari, M., & Szpunar, J. A. (2016). Hydrogen-induced cracking assessment in pipeline steels through permeation and crystallographic texture measurements. *Journal of Materials Engineering and Performance*, *25*(5), 1781-1793.

[15] Pressouyre, G. M. (1979). A classification of hydrogen traps in steel. *Metallurgical Transactions A*, *10*(10), 1571-1573.

[16] Zhong, N., Wang, X. D., Wang, L., & Rong, Y. H. (2009). Enhancement of the mechanical properties of a Nb-microalloyed advanced high-strength steel treated by quenching–partitioning–tempering process. *Materials Science and Engineering: A*, *506*(1-2), 111-116.

[17] Cheng, X., Cheng, X., Jiang, C., Zhang, X., & Wen, Q. (2018). Hydrogen diffusion and trapping in V-microalloyed mooring chain steels. *Materials Letters*, *213*, 118-121.

[18] Shi, X. B., Yan, W., Wang, W., Zhao, L. Y., Shan, Y. Y., & Yang, K. (2015). HIC and SSC behavior of high-strength pipeline steels. *Acta Metallurgica Sinica (English Letters)*, *28*(7), 799-808.

[19] Depover, T., & Verbeken, K. (2016). Evaluation of the effect of V_4C_3 precipitates on the hydrogen induced mechanical degradation in Fe-CV alloys. *Materials Science and Engineering: A*, *675*, 299-313.

[20] Kim, H. J., Jeon, S. H., Yang, W. S., Yoo, B. G., Chung, Y. D., Ha, H. Y., & Chung, H. Y. (2018). Effects of titanium content on hydrogen embrittlement susceptibility of hot-stamped boron steels. *Journal of Alloys and Compounds*, *735*, 2067-2080.

[21] Depover, T., & Verbeken, K. (2016). The effect of TiC on the hydrogen induced ductility loss and trapping behavior of Fe-C-Ti alloys. *Corrosion Science*, *112*, 308-326.

[22] Cho, L., Seo, E. J., Sulistiyo, D. H., Jo, K. R., Kim, S. W., Oh, J. K., ... & De Cooman, B. C. (2018). Influence of vanadium on the hydrogen embrittlement of aluminized ultra-high strength press hardening steel. *Materials Science and Engineering: A*, *735*, 448-455.

[23] Wei, F. G., & Tsuzaki, K. (2006). Quantitative analysis on hydrogen trapping of TiC particles in steel. *Metallurgical and Materials Transactions A*, *37*(2), 331-353.

[24] Turk, A., San Martín, D., Rivera-Díaz-del-Castillo, P. E., & Galindo-Nava, E. I. (2018). Correlation between vanadium carbide size and hydrogen trapping in ferritic steel. *Scripta Materialia*, *152*, 112-116.

[25] Koch, G. H. *et al*. (2002). *Materials Performance*.

[26] "Report 2013-B: Pipeline Performance in Alberta, 1990-2012" (2013). *Alberta Energy Regulator*, Calgary, AB.

[27] Hertelé, S. (2012). *Coupled experimental-numerical framework for the assessment of strain capacity of flawed girth welds in pipelines* (Doctoral dissertation, Ghent University).

[28] Mouriño, N. S. (2010). Crystallographically controlled mechanical anisotropy of pipeline steel. *Ghent University*.

[29] Stalheim, D. G., & Muralidharan, G. (2006, January). The role of continuous cooling transformation diagrams in material design for high strength oil and gas transmission pipeline steels. In *International Pipeline Conference* (Vol. 42630, pp. 231-238).

[30] Vervynckt, S. (2010). *Control of the Non-Recrystallization Temperature in High Strength Low Alloy (HSLA) Steels* (Doctoral dissertation, Ghent University).

[31] Mendoza, R., Huante, J., Alanis, M., Gonzalez-Rivera, C., & Juarez-Islas, J. A. (2000). Processing of ultra low carbon steels with mechanical properties adequate for automotive applications in the as-annealed condition. *Materials Science and Engineering: A*, *276*(1-2), 203-209.

[32] Rosado, D. B., De Waele, W., Vanderschueren, D., & Hertelé, S. (2013). Latest developments in mechanical properties and metallurgical features of high strength line pipe steels. *International Journal of Sustainable Mechanical Engineering and Design*, *4*(1).

[33] Spinelli, C. M., *et al*. (2011). Full scale investigation on strain capacity of high grade large diameter pipes. *3R international, Special*, *1*.

[34] Koo, J. Y., *et al.* (2003, May). Metallurgical design of ultra-high strength steels for gas pipelines. In *The Thirteenth International Offshore and Polar Engineering Conference*. OnePetro.

[35] Jonas, J. & Sellars, C. (1992). Thermomechanical processing: Future developments of metals and ceramics. *London Institute of Materials*, 147-177.

[36] Tamehiro, H., Asahi, H., Hara, T., Terada, Y. (1999). Ultra-high strength, weldable steels with excellent ultra-low temperature toughness, EXXON Production Research Company and NIPPON Steel, *United States Patent 6264760*.

[37] Baker, T. N. (2016). Microalloyed steels. *Ironmaking & Steelmaking*, *43*(4), 264-307.

[38] Baker, T. N. (1992). Microalloyed steels: Future developments of metals and ceramics, *London Institute of Materials*, 75-119.

[39] Gladman, T. (1997). Microalloyed steels. *London Institute of Materials*.

[40] Gray, J. M., Webster, D., & Woodhead, J. H. (1965). Precipitation in mild steels containing small additions of niobium. *IRON STEEL INST J*, *203*(8), 812-818.

[41] Edmonds, D. V., & Honeycombe, R. (1979). Precipitation processes in solids. *Warrendale, PA, Metallurgical Society-AIME,* 121-160.

[42] Halley, J. W. (1946). Grain-growth inhibitors in steel. *Trans. AIME*, *167*, 224-234.

[43] Webster, D. (1962). Effect of precipitates in grain refining microalloyed steels. *Sheffield: BISRA Report No. MG/C/18/62*.

[44] Irvine, K. J., Pickering, F. B., & Gladman, T. (1967). Grain-refined C-Mn steels. *Iron Steel Inst J*, *205*(2), 161-182.

[45] American Petroleum Institute. (2013). API Specification 5L for Line Pipe.

[46] Klinkenberg, C., Hulka, K., & Bleck, W. (2004). Niobium carbide precipitation in microalloyed steel. *Steel Research International*, *75*(11), 744-752.

[47] Mendoza, R., *et al.* (2002). On the processing of Fe–C–Mn–Nb steels to produce plates for pipelines with sour gas resistance. *Materials Science and Engineering: A*, *337*(1-2), 115-120.

[48] Khulka, K., & Aleksandrov, S. (2006). Promising tube steels for gas pipelines. *Metallurgist*, *50*(3), 137-143.

[49] Morrison, W. B. (2009). Microalloy steels–the beginning. *Materials Science and Technology*, *25*(9), 1066-1073.

[50] Morrison, W. B., & Woodhead, J. H. (1963). Influence of small niobium additions on mechanical properties of commercial mild steels. *Journal of the Iron and Steel Institute*, *201*(1), 43.

[51] DeArdo, A. J. (2001). Metallurgical basis for thermomechanical processing of microalloyed steels. *Ironmaking & Steelmaking*, *28*(2), 138-144.

[52] Davenport, A. T., Brossard, L. C., & Miner, R. E. (1975). Precipitation in microalloyed high-strength low-alloy steels. *JOM*, *27*(6), 21-27.

[53] Itman, A., Cardoso, K. R., & Kestenbach, H. J. (1997). Quantitative study of carbonitride precipitation in niobium and titanium microalloyed hot strip steel. *Materials science and technology*, *13*(1), 49-55.

[54] Herman, J., Donnay, B., & Leroy, V. (1992). Precipitation kinetics of microalloying additions during hot-rolling of HSLA steels. *ISIJ international*, *32*(6), 779-785.

[55] Leroy, V. & Herman, J. Final report ECSC contract No 7210-MA/201, 2996, EUR 15748 Fr.

[56] Kruse, J., Kaspar, R., Anelli, E., & Di Nunzio, P. E. (2000). Development of high-strength strip steels with an improved processing potential. *EUR(Luxembourg)*.

[57] Maugis, P., *et al.* (2003, January). A model for niobium carbonitride precipitation in ferrite. In *Materials Science Forum* (Vol. 426, No. 432, pp. 1313-1318).

[58] McDermid, J. & Kish, J. (2019). Special Topics: Ferrous Physical Metallurgy. *McMaster University.*

[59] Han, Y. D., Jing, H. Y., Nai, S. M. L., Tan, C. M., Wei, J., Xu, L. Y., & Zhang, S. R. (2009). A modified constitutive model for creep of Sn–3.5 Ag–0.7 Cu solder joints. *Journal of Physics D: Applied Physics*, *42*(12), 12541.

[60] Lagneborg, R., Siwecki, T., Zajac, S., & Hutchinson, B. (1999). The role of vanadium in microalloyed steels. *Scandinavian Journal of Metallurgy*, *28*(5), 186-241.

[61] Lagneborg, R., Hutchinson, B., Siwecki, T., & Zajac, S. (2014). The role of vanadium in microalloyed steels. *Pittsburgh, PA, USA: Vanitec Publication*.

[62] Charleux, M., Poole, W. J., Militzer, M., & Deschamps, A. (2001). Precipitation behavior and its effect on strengthening of an HSLA-Nb/Ti steel. *Metallurgical and Materials Transactions A*, *32*(7), 1635-1647.

[63] DeArdo, A. Gray, J. M., Meyer, L. Niobium, H. Stuart. (1984). *TMS-AIME, Warrendale, PA*, 685-759.

[64] Nordberg, H. & Aronsson, B. (1968). *Jour. Iron Steel Inst*., 1263.

[65] Irvine, K. J., Pickering, F. B., & Gladman, T. J. (1967). Iron Steel. *Inst*, *205*, 161.

[66] Mendoza, R., Alanis, M., Huante, J., Gonzalez-Rivera, C., & Juarez-Islas, J. A. (2000). Evaluation of the mechanical properties and corrosion behaviour of ultra-clean steels. *Journal of Materials Processing Technology*, *101*(1-3), 238-244.

[67] Gräf, M. K., Hillenbrand, H. G., & Peters, P. A. (1986). Accelerated Cooling of Steel. *TMS, Warrendale (Pa)*, 165-179.

[68] Gräf, M., Schröder, J., Schwinn, V., & Hulka, K. (2002). Pipe Dreamer's Conf. *Proc., Yokohama (Japan)*, 323.

[69] Bhadeshia, H. K. D. H. (1992). Bainite in steels. Cambridge: The Institute of Materials.

[70] Hall, E. (1951). The deformation and ageing of mild steel. *Proc. Phys. Soc.,* 747-753.

[71] Petch, N. J. (1953). The cleavage strength of polycrystals. *Journal of the Iron and Steel Institute*, *174*, 25-28.

[72] Liessem, A., Knauf, G., & Zimmermann, S. (2007, July). Strain based design—what the contribution of a pipe manufacturer can be. In *The Seventeenth International Offshore and Polar Engineering Conference*. OnePetro.

[73] Kozasu, I., Shimizu, T., & Kubota, H. (1971). Recrystallization of Austenite of Si-Mn Steels with Minor Alloying Elements after Hot Rolling. *Transactions of the Iron and Steel Institute of Japan*, *11*(6), 367-375.

[74] Kozasu, I., Ouchi, C., Sampei, T., Okita, T. (1977). Hot rolling as high temperature thermomechanical process, *Microalloying '75' 120-134, New York, Union Carbide Corporation.*

[75] Xie, H., Du, L. X., Hu, J., & Misra, R. D. K. (2014). Microstructure and mechanical properties of a novel 1000 MPa grade TMCP low carbon microalloyed steel with combination of high strength and excellent toughness. *Materials Science and Engineering: A*, *612*, 123-130.

[76] Tamura, I., Ouchi, C., Tanaka, T., Sekine, H. (1988) Thermomechanical processing of high strength low alloy steel. *London, Butterworths*.

[77] Vervynckt, S., Verbeken, K., Lopez, B., & Jonas, J. J. (2012). Modern HSLA steels and role of non-recrystallisation temperature. *International Materials Reviews*, *57*(4), 187-207.

[78] Priestner, R., Earley, C. C., & Rendall, J. H. (1968). Observations on behavior of austenite during hot working of some low-carbon steels. *J IRON STEEL INST*, *206*(12).

[79] Tanaka, T., Tabata, N., Hatomura, T., Shiga, C. (1977). Three stages of controlled-rolling process, *Microalloying '75' New York, Union Carbide Corp.*, 107-118.

[80] Vervynckt, S. (2010). *Control of the Non-Recrystallization Temperature in High Strength Low Alloy (HSLA) Steels* (Doctoral dissertation, Ghent University).

[81] Priestner, R., & De los Rios, E. (1980). Ferrite grain refinement by controlled rolling of low-carbon and microalloyed steel. *Metals Technology*, *7*(1), 309-316.

[82] Sellars, C. M., & Whiteman, J. A. (1979). Recrystallization and grain growth in hot rolling. *Metal Science*, *13*(3-4), 187-194.

[83] Sellars, C. M. (1990) The physical metallurgy of hot rolling. *London, Institute of Materials*.

[84] Haumann, W. & Koch, F. (1985). New steels for high pressure gas pipeline. *Rd International Conference on Steel Rolling-Technology of pipe and tube and their application, Tokyo,* 581-588.

[85] Nakasugi, H., Matsuda, H., & Tamehiro, H. (1980). Development of Controlled Rolled Ultra-Low-Carbon Bainitic Steel for Large-Diameter Linepipe. *Alloys for the Eighties*, 213-224.

[86] Charles, A. (2003). Corrosion Mechanisms in Theory and Practice, Hardback-Edited by Philippe Marcus, Marcel Decker, USA, 2002. *Electrochimica Acta*, *8*(48), 1081.

[87] Tiu, B. D. B., & Advincula, R. C. (2015). Polymeric corrosion inhibitors for the oil and gas industry: Design principles and mechanism. *Reactive and Functional Polymers*, *95*, 25-45.

[88] Beck, W., Bockris, J. O. M., McBreen, J., & Nanis, L. (1966). Hydrogen permeation in metals as a function of stress, temperature and dissolved hydrogen concentration. *Proceedings of the Royal Society of London. Series A. Mathematical and Physical Sciences*, *290*(1421), 220-235.

[89] Al-Mansour, M., Alfantazi, A. M., & El-Boujdaini, M. (2009). Sulfide stress cracking resistance of API-X100 high strength low alloy steel. *Materials & Design*, *30*(10), 4088-4094.

[90] Barrera, O. *et al*. (2018). Understanding and mitigating hydrogen embrittlement of steels: a review of experimental, modelling and design progress from atomistic to continuum. *Journal of materials science*, *53*(9), 6251-6290.

[91] TM0284, N. S. (2011). Evaluation of pipeline and pressure vessel steels for resistance to hydrogen-induced cracking. *NACE International, Houston, TX*.

[92] Revie, R. W., Sastri, V. S., Elboujdaini, M., Ramsingh, R. R., & Lafrenière, Y. (1993). Hydrogen-induced cracking of line pipe steels used in sour service. *Corrosion*, *49*(7), 531-535.

[93] Huang, F. *et al*. (2010). Effect of microstructure and inclusions on hydrogen induced cracking susceptibility and hydrogen trapping efficiency of X120 pipeline steel. *Materials Science and Engineering: A*, *527*(26), 6997-7001.

[94] Haq, A. J., Muzaka, K., Dunne, D. P., Calka, A., & Pereloma, E. V. (2013). Effect of microstructure and composition on hydrogen permeation in X70 pipeline steels. *International journal of hydrogen energy*, *38*(5), 2544-2556.

[95] Mohtadi-Bonab, M. A., Szpunar, J. A., Collins, L., & Stankievech, R. (2014). Evaluation of hydrogen induced cracking behavior of API X70 pipeline steel at different heat treatments. *International journal of hydrogen energy*, *39*(11), 6076-6088.

[96] Hejazi, D., *et al*. (2012). Effect of manganese content and microstructure on the susceptibility of X70 pipeline steel to hydrogen cracking. *Materials Science and Engineering: A*, *551*, 40-49.

[97] Shi, X. B., *et al*. (2015). Effect of microstructure on hydrogen induced cracking behavior of a high deformability pipeline steel. *Journal of Iron and Steel Research International*, *22*(10), 937-942.

[98] Nanninga, N., Grochowsi, J., Heldt, L., & Rundman, K. (2010). Role of microstructure, composition and hardness in resisting hydrogen embrittlement of fastener grade steels. *Corrosion Science*, *52*(4), 1237-1246.

[99] Park, G. T., Koh, S. U., Jung, H. G., & Kim, K. Y. (2008). Effect of microstructure on the hydrogen trapping efficiency and hydrogen induced cracking of linepipe steel. *Corrosion science*, *50*(7), 1865-1871.

[100] Moon, J., Park, C., & Kim, S. J. (2012). Influence of Ti addition on the hydrogen induced cracking of API 5L X70 hot-rolled pipeline steel in acid sour media. *Metals and Materials International*, *18*(4), 613-617.

[101] Telang, A., *et al*. (2018). Effect of thermo-mechanical processing on sensitization and corrosion in alloy 600 studied by SEM-and TEM-Based diffraction and orientation imaging techniques. *Journal of Nuclear Materials*, *505*, 276-288.

[102] Saleh, A. A., Hejazi, D., Gazder, A. A., Dunne, D. P., & Pereloma, E. V. (2016). Investigation of the effect of electrolytic hydrogen charging of X70 steel: II. Microstructural and crystallographic analyses of the formation of hydrogen induced cracks and blisters. *international journal of hydrogen energy*, *41*(28), 12424-12435.

[103] Eskandari, M., *et al*. (2015). In-situ strain localization analysis in low density transformation-twinning induced plasticity steel using digital image correlation. *Optics and Lasers in Engineering*, *67*, 1-16.

[104] Mohtadi-Bonab, M. A., Eskandari, M., Karimdadashi, R., & Szpunar, J. A. (2017). Effect of different microstructural parameters on hydrogen induced cracking in an API X70 pipeline steel. *Metals and Materials International*, *23*(4), 726-735.

[105] Moore, E. M., & Warga, J. J. (1976). Factors influencing the hydrogen cracking sensitivity of pipeline steels. *Mater. Performance;(United States)*, *15*.

[106] Kyada, T., Shant, J. R., Goyal, R. K., & Kathayat, T. S. (2014). Understanding the Delamination and Its Effect on Charpy Impact Energy in Thick Wall Linepipe Steel. *J. Mater. Metall. Eng*, *4*(1), 31-39.

[107] Koyama, M. *et al*. (2017). Recent progress in microstructural hydrogen mapping in steels: quantification, kinetic analysis, and multi-scale characterisation. *Materials Science and Technology*, *33*(13), 1481-1496.

[108] Takahashi, J., Kawakami, K., Kobayashi, Y., & Tarui, T. (2010). The first direct observation of hydrogen trapping sites in TiC precipitation-hardening steel through atom probe tomography. *Scripta Materialia*, *63*(3), 261-264.

[109] Chen, Y. S., Lu, H., Liang, J., Rosenthal, A., Liu, H., Sneddon, G., ... & Cairney, J. M. (2020). Observation of hydrogen trapping at dislocations, grain boundaries, and precipitates. *Science*, *367*(6474), 171-175.

[110] Wei, F. G., & Tsuzaki, K. (2004). Hydrogen absorption of incoherent TiC particles in iron from environment at high temperatures. *Metallurgical and Materials Transactions A*, *35*(10), 3155-3163.

[111] Abayarathna, D., & Naraghi, A. R. (1998, March). Overview of Hydrogen Permeation Measurement and Monitoring Techniques. In *CORROSION 98*. OnePetro.

[112] Devanathan, M. A. V., & Stachurski, Z. (1962). The adsorption and diffusion of electrolytic hydrogen in palladium. *Proceedings of the Royal Society of London. Series A. Mathematical and Physical Sciences*, *270*(1340), 90-102.

[113] Vecchi, L., *et al. (*2018). Modelling of hydrogen permeation experiments in iron alloys: Characterization of the accessible parameters–Part II–The exit side. *Electrochimica Acta*, *262*, 153-161.

[114] Zhang, Z., Moore, K. L., McMahon, G., Morana, R., & Preuss, M. (2019). On the role of precipitates in hydrogen trapping and hydrogen embrittlement of a nickel-based superalloy. *Corrosion Science*, *146*, 58-69.

[115] Kesten, P., Pundt, A., Schmitz, G., Weisheit, M., Krebs, H. U., & Kirchheim, R. (2002). H-and D distribution in metallic multilayers studied by 3-dimensional atom probe analysis and secondary ion mass spectrometry. *Journal of alloys and compounds*, *330*, 225-228.

[116] Chen, Y. S., *et al*. (2017). Direct observation of individual hydrogen atoms at trapping sites in a ferritic steel. *Science*, *355*(6330), 1196-1199.

[117] Sakaguchi, H., Kohzai, A., Hatakeyama, K., Fujine, S., Yoneda, K., Kanda, K., & Esaka, T. (2000). Visualization of hydrogen in hydrogen storage alloys using neutron radiography. *International journal of hydrogen energy*, *25*(12), 1205-1208.

[118] Grosse, M., Van den Berg, M., Goulet, C., Lehmann, E., & Schillinger, B. (2011). In-situ neutron radiography investigations of hydrogen diffusion and absorption in zirconium alloys. *Nuclear Instruments and Methods in Physics Research Section A: Accelerators, Spectrometers, Detectors and Associated Equipment*, *651*(1), 253-257.

[119] Beyer, K., Kannengießer, T., Griesche, A., & Schillinger, B. (2011). Study of hydrogen effusion in austenitic stainless steel by time-resolved in-situ measurements using neutron radiography. *Nuclear Instruments and Methods in Physics Research Section A: Accelerators, Spectrometers, Detectors and Associated Equipment*, *651*(1), 211-215.

[120] Gault, B., *et al*. (2010). Spatial resolution in atom probe tomography. *Microscopy and Microanalysis*, *16*(1), 99-110.

[121] McCarroll, I. E., Bagot, P. A. J., Devaraj, A., Perea, D. E., & Cairney, J. M. (2020). New frontiers in atom probe tomography: a review of research enabled by cryo and/or vacuum transfer systems. *Materials Today Advances*, *7*, 100090.

[122] Miller, M. K. (2012). Atom probe tomography: analysis at the atomic level. *Springer Science & Business Media*

[123] Asaoka, T., Lapasset, G., Aucouturier, M., & Lacombe, P. (1978). Observation of hydrogen trapping in Fe-0.15 wt% Ti alloy by high resolution autoradiography. *Corrosion*, *34*(2), 39-47.

[124] Choo, W. Y., & Lee, J. Y. (1982). Thermal analysis of trapped hydrogen in pure iron. *Metallurgical Transactions A*, *13*(1), 135-140.

[125] Kumnick, A. J., & Johnson, H. H. (1980). Deep trapping states for hydrogen in deformed iron. *Acta Metallurgica*, *28*(1), 33-39.

[126] Pressouyre, G. M., & Bernstein, I. M. (1978). A quantitative analysis of hydrogen trapping. *Metallurgical transactions A*, *9*(11), 1571-1580.

[127] Lee, J. L., & Lee, J. Y. (1983). Hydrogen trapping in AISI 4340 steel. *Metal Science*, *17*(9), 426-432.

[128] Lee, J. Y., & Lee, S. M. (1986). Hydrogen trapping phenomena in metals with BCC and FCC crystals structures by the desorption thermal analysis technique. *Surface and Coatings Technology*, *28*(3-4), 301-314.

[129] Wallaert, E., Depover, T., Arafin, M., & Verbeken, K. (2014). Thermal desorption spectroscopy evaluation of the hydrogen-trapping capacity of NbC and NbN precipitates. *Metallurgical and Materials Transactions A*, *45*(5), 2412-2420.

[130] Depover, T., Escobar, D. P., Wallaert, E., Zermout, Z., & Verbeken, K. (2014). Effect of hydrogen charging on the mechanical properties of advanced high strength steels. *International journal of hydrogen energy*, *39*(9), 4647-4656.

[131] Duprez, L., Verbeken, K., & Verhaege, M. (2009). Effect of hydrogen on the mechanical properties of multiphase high strength steels. *Effect of hydrogen on materials*, 62-69.

[132] Wei, F. G., Hara, T., & Tsuzaki, K. (2004). Precise determination of the activation energy for desorption of hydrogen in two Ti-added steels by a single thermal-desorption spectrum. *Metallurgical and Materials Transactions B*, *35*(3), 587-597.

[133] Dong, C. F., Li, X. G., Liu, Z. Y., & Zhang, Y. R. (2009). Hydrogen-induced cracking and healing behaviour of X70 steel. *Journal of alloys and compounds*, *484*(1-2), 966-972.

[134] Beidokhti, B., Dolati, A., & Koukabi, A. H. (2009). Effects of alloying elements and microstructure on the susceptibility of the welded HSLA steel to hydrogen-induced cracking and sulfide stress cracking. *Materials Science and Engineering: A*, *507*(1-2), 167-173.

[135] Takahashi, J., Kawakami, K., & Tarui, T. (2012). Direct observation of hydrogen-trapping sites in vanadium carbide precipitation steel by atom probe tomography. *Scripta Materialia*, *67*(2), 213-216.

[136] Zhang, S., Fan, E., Wan, J., Liu, J., Huang, Y., & Li, X. (2018). Effect of Nb on the hydrogen-induced cracking of high-strength low-alloy steel. *Corrosion Science*, *139*, 83-96.

[137] Somerday, B., Sofronis, P., & Jones, R. H. (Eds.). (2009). *Effects of Hydrogen on Materials: Proceedings of the 2008 International Hydrogen Conference, September 7-10, 2008, Jackson Lake Lodge, Grand Teton National Park, Wyoming, USA*. ASM International.

[138] Ohnuma, M., Suzuki, J. I., Wei, F. G., & Tsuzaki, K. (2008). Direct observation of hydrogen trapped by NbC in steel using small-angle neutron scattering. *Scripta Materialia*, *58*(2), 142-145.

[139] Qin, W., & Szpunar, J. A. (2017). A general model for hydrogen trapping at the inclusion-matrix interface and its relation to crack initiation. *Philosophical Magazine*, *97*(34), 3296-3316.

[140] Li, D., Gangloff, R. P., & Scully, J. R. (2004). Hydrogen trap states in ultrahigh-strength AERMET 100 steel. *Metallurgical and materials transactions A*, *35*(3), 849-864.

[141] Findley, K. O., O'Brien, M. K., & Nako, H. (2015). Critical Assessment 17: Mechanisms of hydrogen induced cracking in pipeline steels. *Materials Science and Technology*, *31*(14), 1673-1680.

[142] Jin, T. Y., Liu, Z. Y., & Cheng, Y. F. (2010). Effect of non-metallic inclusions on hydrogen-induced cracking of API5L X100 steel. *International Journal of Hydrogen Energy*, *35*(15), 8014-8021.

[143] Kirchheim, R. (2019). Changing the interfacial composition of carbide precipitates in metals and its effect on hydrogen trapping. *Scripta Materialia*, *160*, 62-65.

[144] Wei, F. G., & Tsuzaki, K. (2012). Hydrogen trapping phenomena in martensitic steels. In *Gaseous Hydrogen Embrittlement of Materials in Energy Technologies* (pp. 493-525). Woodhead Publishing.

[145] Wei, F. G., Hara, T., & Tsuzaki, K. (2011). Nano-precipitates design with hydrogen trapping character in high strength steel. In *Advanced steels* (pp. 87-92). Springer, Berlin, Heidelberg.

[146] Krawiec, H., Vignal, V., & Oltra, R. (2004). Use of the electrochemical microcell technique and the SVET for monitoring pitting corrosion at MnS inclusions. *Electrochemistry Communications*, *6*(7), 655-660.

[147] Wei, J., Dong, J. H., Ke, W., & He, X. Y. (2015). Influence of inclusions on early corrosion development of ultra-low carbon bainitic steel in NaCl solution. *Corrosion*, *71*(12), 1467-1480.

[148] Qiu, J., *et al*. (2018). Effect of SO_4^{2-} on the corrosion of 316L stainless steel in molten FLiNaK salt. *Corrosion Science*, *144*, 224-229.

[149] Jin, T. Y., & Cheng, Y. F. (2011). In situ characterization by localized electrochemical impedance spectroscopy of the electrochemical activity of microscopic inclusions in an X100 steel. *Corrosion science*, *53*(2), 850-853.

[150] Park, I. J., Lee, S. M., Kang, M., Lee, S., & Lee, Y. K. (2015). Pitting corrosion behavior in advanced high strength steels. *Journal of Alloys and Compounds*, *619*, 205-210.

[151] Yang, Z., *et al*. (2017). Pitting initiation and propagation of x70 pipeline steel exposed to chloride-containing environments. *Materials*, *10*(9), 1076.

[152] Xue, W., *et al*. (2020). Initial microzonal corrosion mechanism of inclusions associated with the precipitated (Ti, Nb) N phase of Sb-containing weathering steel. *Corrosion Science*, *163*, 108232.

[153] Zheng, S. J., *et al*. (2010). Identification of MnCr2O4 nano-octahedron in catalyzing pitting corrosion of austenitic stainless steels. *Acta Materialia*, *58*(15), 5070-5085.

[154] Liu, C. *et al*. (2021). Towards a better understanding of localised corrosion induced by typical non-metallic inclusions in low-alloy steels. *Corrosion Science*, *179*, 109150.

[155] Orjuela, G. A., Rincon, R., & Olaya, J. J. (2014). Corrosion resistance of niobium carbide coatings produced on AISI 1045 steel via thermo-reactive diffusion deposition. *Surface and Coatings Technology*, *259*, 667-675.

[156] Fernandes, F. A. P., *et al*. (2015). Wear and corrosion of niobium carbide coated AISI 52100 bearing steel. *Surface and Coatings Technology*, *279*, 112-117.

[157] Wang, L., *et al*. (2012). Niobium nitride modified AISI 304 stainless steel bipolar plate for proton exchange membrane fuel cell. *Journal of Power Sources*, *199*, 195-200.

[158] Fonseca, R. M., *et al*. (2019). Corrosion behavior of magnetron sputtered NbN and Nb1-xAlxN coatings on AISI 316L stainless steel. *Surface and Coatings Technology*, *378*, 124987.

[159] Rohwerder, M., & Turcu, F. (2007). High-resolution Kelvin probe microscopy in corrosion science: scanning Kelvin probe force microscopy (SKPFM) versus classical scanning Kelvin probe (SKP). *Electrochimica Acta*, *53*(2), 290-299.

[160] Iannuzzi, M., Vasanth, K. L., & Frankel, G. S. (2017). Unusual correlation between SKPFM and corrosion of nickel aluminum bronzes. *Journal of The Electrochemical Society*, *164*(9), C488.

[161] ASTM International. (2018). *E1019-18 Standard Test Methods for Determination of Carbon, Sulfur, Nitrogen, and Oxygen in Steel, Iron, Nickel, and Cobalt Alloys by Various Combustion and Inert Gas Fusion Techniques*. Retrieved from https://doi.org/10.1520/E1019-18

[162] ASTM International. (2017). *E1097-12 Standard Guide for Determination of Various Elements by Direct Current Plasma Atomic Emission Spectrometry*. Retrieved from https://doi.org/10.1520/E1097-12R17

[163] ASTM International. (2016). *E1479-16 Standard Practice for Describing and Specifying Inductively Coupled Plasma Atomic Emission Spectrometers*. Retrieved from https://doi.org/10.1520/E1479-16

[164] Weiss, I. E. J. J. J., & Jonas, J. J. (1979). Interaction between recrystallization and precipitation during the high temperature deformation of HSLA steels. *Metallurgical Transactions A*, *10*(7), 831-840.

[165] ASTM International. (2013). *E112-13 Standard Test Methods for Determining Average Grain Size*. Retrieved from https://doi.org/10.1520/E0112-13

[166] Pourbaix, M. (1974). Atlas of electrochemical equilibria in aqueous solution. *NACE*, *307*.

[167] Tang, X., & Cheng, Y. F. (2008). Localized dissolution electrochemistry at surface irregularities of pipeline steel. *Applied Surface Science*, *254*(16), 5199-5205.

[168] Parkins, R. N., Blanchard, W. K., & Delanty, B. S. (1994). Transgranular stress corrosion cracking of high-pressure pipelines in contact with solutions of near neutral pH. *Corrosion*, *50*(05).

[169] ASTM International. (2017). *G1-03(2017)e1 Standard Practice for Preparing, Cleaning, and Evaluating Corrosion Test Specimens*. Retrieved from https://doi.org/10.1520/G0001-03R17E01

[170] Biesinger, M. C., Payne, B. P., Grosvenor, A. P., Lau, L. W., Gerson, A. R., & Smart, R. S. C. (2011). Resolving surface chemical states in XPS analysis of first row transition metals, oxides and hydroxides: Cr, Mn, Fe, Co and Ni. *Applied Surface Science*, *257*(7), 2717-2730.

[171] Grosvenor, A. P., Kobe, B. A., Biesinger, M. C., & McIntyre, N. S. (2004). Investigation of multiplet splitting of Fe 2p XPS spectra and bonding in iron compounds. *Surface and Interface Analysis: An International Journal devoted to the development and application of techniques for the analysis of surfaces, interfaces and thin films*, *36*(12), 1564-1574.

[172] Lu, J., Wiskel, J. B., Omotoso, O., Henein, H., & Ivey, D. G. (2011). Matrix dissolution techniques applied to extract and quantify precipitates from a microalloyed steel. *Metallurgical and Materials Transactions A*, *42*(7), 1767-1784.

[173] Gladman, T. (1997). The Physical Metallurgy of Microalloyed Steels, *The Institute of Materials*.

[174] Miura, A., *et al.* (2013). Bonding preference of carbon, nitrogen, and oxygen in niobium-based rock-salt structures. *Inorganic chemistry*, *52*(17), 9699-9701.

[175] Rempel, A. A., & Gusev, A. I. (1985). Order-disorder phase transition in nonstoichiometric niobium carbide. *Kristallografiya*, *30*(6), 1112-1115.

[176] Christensen, A. N., Hazell, R. G., & Lehmann, M. S. (1981). An X-Ray and Neutron Diffraction Investigation of the Crystal Structure of Gamma-NbN. *Acta Chemica Scandinavica*, (2), 111-115.

[177] Frenzel, N., Irran, E., Lerch, M., & Buchsteiner, A. (2011). Synthesis and Crystal Structure of Nbo. 84N. *Zeitschrift für Naturforschung B*, *66*(1), 1-6.

[178] Christensen, A. N. (1977). Preparation and Structure of Stoichiometric delta-NbN.

[179] Hager, G., & Baumgartner, O. (1980). Crystal structure and lattice distortion of γ-NbNsub (x) and delta-NbNsub (x). *Journal of Physics. C, Solid State Physics*, *13*(32), 5833-5841.

[180] Clark, R. N., Searle, J., Martin, T. L., Walters, W. S., & Williams, G. (2020). The role of niobium carbides in the localised corrosion initiation of 20Cr-25Ni-Nb advanced gas-cooled reactor fuel cladding. *Corrosion Science*, *165*, 108365.

[181] Maire, E., & Withers, P. J. (2014). Quantitative X-ray tomography. *International materials reviews*, *59*(1), 1-43.

[182] Ghahari, S. M., Davenport, A. J., Rayment, T., Suter, T., Tinnes, J. P., Padovani, C., ... & Mokso, R. (2011). In situ synchrotron X-ray micro-tomography study of pitting corrosion in stainless steel. *Corrosion Science*, *53*(9), 2684-2687.

[183] Picco, L. M., Bozec, L., Ulcinas, A., Engledew, D. J., Antognozzi, M., Horton, M. A., & Miles, M. J. (2006). Breaking the speed limit with atomic force microscopy. *Nanotechnology*, *18*(4), 044030.

[184] Moore, S., Burrows, R., Picco, L., Martin, T. L., Greenwell, S. J., Scott, T. B., & Payton, O. D. (2018). A study of dynamic nanoscale corrosion initiation events using HS-AFM. *Faraday discussions*, *210*, 409-428.

[185] Laferrere, A., Burrows, R., Glover, C., Clark, R. N., Payton, O., Picco, L., ... & Williams, G. (2017). In situ imaging of corrosion processes in nuclear fuel cladding. *Corrosion Engineering, Science and Technology*, *52*(8), 596-604.

[186] Li, D. G., Feng, Y. R., Bai, Z. Q., Zhu, J. W., & Zheng, M. S. (2008). Photo-electrochemical analysis of passive film formed on X80 pipeline steel in bicarbonate/carbonate buffer solution. *Applied surface science*, *254*(9), 2837-2843.